



# Measurement of Something

by

Kiyotaka Akabori

Submitted in partial fulfillment of the  
requirements for the degree of

Doctor of Philosophy

at

Carnegie Mellon University

Department of Physics

Pittsburgh, Pennsylvania

Advised by Professor John F. Nagle  
and Professor Stephanie Tristram-Nagle

June 30, 2014







# Contents

<b>1</b>	<b>Introduction</b>	<b>1</b>
<b>2</b>	<b>Materials and Methods</b>	<b>3</b>
2.1	X-ray optics . . . . .	3
2.2	Hydration Chamber . . . . .	3
2.3	Sample Preparation . . . . .	4
2.3.1	Stock Solutions . . . . .	4
2.3.2	Thin Film Samples . . . . .	4
2.4	CCD detector . . . . .	5
<b>3</b>	<b>Structural Perturbation of Lipid Bilayers Due to Tat Peptide</b>	<b>6</b>
3.1	Introduction . . . . .	6
3.2	Materials and Methods . . . . .	9
3.2.1	Volume Measurements . . . . .	9
3.2.2	Analysis of Diffuse Scattering . . . . .	11
3.2.3	Modeling the Bilayer Structure . . . . .	17
3.2.4	Molecular Dynamics Simulation . . . . .	23
3.3	Analysis of Molecular Dynamics Simulation Data . . . . .	26
3.3.1	SIMtoEXP program . . . . .	26
3.3.2	Local Thinning of Membranes . . . . .	26
3.3.3	Lateral Decay Length of Membrane Thinning . . . . .	28
3.4	Results . . . . .	30
3.4.1	Bending and Bulk Modulus . . . . .	30
3.4.2	Volume results . . . . .	32
3.4.3	Electron Density Profile Modeling . . . . .	33
3.4.4	Hard Wall Constrain Fits . . . . .	43

3.4.5	Summary of Electron Density Profile Modeling . . . . .	44
3.4.6	Molecular Dynamics Simulations . . . . .	46
3.5	Discussion . . . . .	55
3.6	Conclusion . . . . .	58
<b>4</b>	<b>Ripple Phase</b>	<b>60</b>
4.1	Introduction . . . . .	60
4.2	Materials and Methods . . . . .	62
4.2.1	Sample Preparation . . . . .	62
4.2.2	Instrumental Resolution . . . . .	63
4.2.3	Low Angle X-ray Scattering Experiment . . . . .	65
4.2.4	Near Grazing Incidence Wide Angle X-ray Scattering Experiment	67
4.2.5	Transmission Wide Angle X-ray Scattering Experiment . . . .	71
4.3	LAXS: analysis . . . . .	78
4.3.1	Lattice Structure . . . . .	78
4.3.2	Sample q-space . . . . .	79
4.3.3	Lorentz Correction . . . . .	81
4.3.4	Absorption Correction for LAXS . . . . .	86
4.3.5	Correction due to mosaic spread . . . . .	90
4.4	LAXS: model . . . . .	93
4.4.1	Contour Part of the Form Factor . . . . .	93
4.4.2	Transbilayer Part of the Form Factor . . . . .	95
4.5	LAXS: results . . . . .	96
4.5.1	Data and Electron Density Profile . . . . .	96
4.6	NGIWAXS: analysis . . . . .	97
4.6.1	Absorption Correction . . . . .	97
4.7	NGIWAXS: model . . . . .	99
4.7.1	Thin rod model . . . . .	99
4.8	NGIWAXS: results . . . . .	99
4.9	TWAXS: results . . . . .	99
4.10	Discussion . . . . .	103
4.11	Conclusion . . . . .	103
	<b>Appendices</b>	<b>104</b>

<b>A</b>	<b>Tat</b>	<b>105</b>
A.1	Analysis of Fixed Angle Data using NFIT . . . . .	105
A.1.1	Theory . . . . .	105
A.1.2	Results . . . . .	105
A.2	Mosaic Spread for NFIT analysis . . . . .	105
A.2.1	Mosaic Spread: Calculation . . . . .	105
A.2.2	Mosaic Spread: Experiment . . . . .	110
A.2.3	NFIT . . . . .	112
A.2.4	Results . . . . .	113
A.3	Some More Details of Tat Stuff if needed . . . . .	113
<b>B</b>	<b>Ripple Phase</b>	<b>114</b>
B.1	Derivation of the contour part of the form factor . . . . .	114
B.2	Rotation of a Two-Dimensional Function . . . . .	116
B.3	Derivation of the transbilayer part of the form factor in the 2G hybrid model . . . . .	117
B.4	Correction due to refractive index . . . . .	119



# List of Tables

3.1	Some Amino Acids Data . . . . .	10
3.2	Number of electrons per lipid and volume per lipid. . . . .	22
3.3	Some structural parameters for each component. $n_i^e$ is the number of electrons and $\rho_i$ is the average electron density. . . . .	22
3.4	Tat basic structural parameters. The notations are the same as in Table 3.3. $x_{\text{Tat}} = \text{Tat}/(\text{Tat}+\text{Lipid})$ . . . . .	22
3.5	Volume results at 37 °C . . . . .	33
3.6	Fitting Results for DOPC membranes for the THG (Tat in headgroup) model. $z_{\text{PC}} - z_{\text{CG}} = 3.1 \text{ \AA}$ and $z_{\text{CG}} - z_{\text{HC}} = 1.3 \text{ \AA}$ in all fits. . . . .	34
3.7	Fitting Results for DOPC:DOPE (3:1) membranes for the THG model. $z_{\text{PC}} - z_{\text{CG}} = 3.1 \text{ \AA}$ and $z_{\text{CG}} - z_{\text{HC}} = 1.3 \text{ \AA}$ in all fits. . . . .	37
3.8	(Numbers are wrong) Fitting Results for DOPC:DOPE (1:1) membranes for the THG model. $\Delta z_1 = z_{\text{PC}} - z_{\text{CG}}$ and $\Delta z_2 = z_{\text{CG}} - z_{\text{HC}}$ . . . . .	37
3.9	Fitting Results of the bound THG model for DOPC membranes. $\Delta z_1 = z_{\text{PC}} - z_{\text{CG}}$ and $\Delta z_2 = z_{\text{CG}} - z_{\text{HC}}$ . . . . .	44
3.10	Comparison of the simulated form factors to the experimental form factors. . . . .	51
3.11	Summary of simulation results. $\langle D_{\text{PP}} \rangle$ , phosphorus-phosphorus distance averaged over all lipids; $D_{\text{PP}}$ , Tat-perturbed phosphorus atoms; $x$ , thickness away from Tat; $\Delta t$ , $\langle D_{\text{PP}}^{\text{DOPC}} \rangle - D_{\text{PP}}$ ; $H_{\text{Tat}}$ , Tat height; $R_{\text{Tat}}$ , radius of Tat cylinder; $R_2$ , radius of the calculated in-plane Tat-perturbed region; $R_3$ , effective radius of the simulation box. . . . .	52
3.12	Summary of weighted average results. The caption is the same as Table 3.11. . . . .	52

4.1	Lattice constants for DMPC at $T = 18.0$ °C reported by Wack and Webb [76]. The data collected and analyzed in this thesis are colored blue. . . . .	62
4.2	Definitions of $Z_{\text{CH}_2}$ and $Z_{\text{W}}$ . . . . .	95
4.3	Observed intensity for $h = 1$ to 3 at $D = 57.8$ , $\lambda_r = 145$ , and $\gamma = 98.2^\circ$ . *Unoriented data are from Wack and Webb [76]. . . . .	97
4.4	Observed intensity for $h = 4$ to 9 at $D = 57.8$ , $\lambda_r = 145$ , and $\gamma = 98.2^\circ$ (continued from Table 4.3). . . . .	98

# List of Figures

1.1	Experimental phase diagram of DMPC from Ref. [1]. . . . .	1
3.1	LAXS of DOPC:DOPE (1:1) with $x_{\text{Tat}} = 0.034$ at 37 °C. White lobes of diffuse scattering intensity have large grey numbers, while lamellar orders and beam are shown to the left of the molybdenum beam attenuator (short, dark rectangle). $q_z$ and $q_r$ are the cylindrical coordinates of the sample $q$ -space, where $q_z$ -axis is along the bilayer normal and $q_r$ -axis is along the in-plane direction. The lamellar repeat spacing was $D = 66.2$ Å. . . . .	12
3.2	Schematic of an oriented stack of lipid bilayers. Thick green curves represent an instance of thermally fluctuating bilayers. The dashed lines show the thermally averaged positions $z = nD$ of the centers of each bilayer and $u_n(x, y)$ gives the instantaneous deviation from the average. Each bilayer extends in the $\mathbf{r} = (x, y)$ plane. . . . .	13
3.3	Expanded view of a fluctuating bilayer. Along the two black solid lines, the electron density profile is identical in an incompressible bilayer. Along the dashed line, the bilayer appears thicker by a factor $1/\cos \alpha$ . This apparent thickness variation along the $z$ direction is corrected by the undulation correction. . . . .	14
3.4	Schematic of DOPC showing each lipid component. The dash lines show where the lipid is divided into different components. The lipid headgroup is divided into two components, phosphate-choline (PC) and carbonyl-glycerol (CG). The hydrocarbon chain region is also divided into two components, methylene+methine ( $\text{CH}_2+\text{CH}$ ) and terminal methyl groups ( $\text{CH}_3$ ). . . . .	18
3.5	A model electron density profile for DOPC with Tat. . . . .	19

3.6	Our simple model to extract the local bilayer thickness from simulation trajectories. Tat is modeled as a cylinder with its height $H_{\text{Tat}}$ and radius $R_{\text{Tat}}$ . The local thickness is defined as $D'_{\text{phos-phos}}$ . The thickness of the unperturbed DOPC bilayer is $D_{\text{phos-phos}}$ . Blue highlighted lipids fall within the imaginary cylinder extended from the Tat. Unperturbed lipids are highlighted in green. . . . .	27
3.7	Simple model of the lateral decay of the membrane thickness perturbation due to Tat. . . . .	29
3.8	Bilayer bending modulus, $K_c$ , vs. Tat mole fraction $x_{\text{Tat}}$ . $D$ -spacings for DOPC/Tat mixtures varied from 64 to 68 Å, for DOPC/DOPE/Tat mixtures from 64 to 69 Å, for DOPC/DOPS/Tat (3:1) mixtures from 57 Å to 100 Å (pure DOPS was unbound), and for nuclear mimic/Tat mixtures from unbound (nuclear mimic) to 64 Å. Estimated uncertainty in all values is about $\pm 2$ . . . . .	31
3.9	Form factors of lipid mixtures (arbitrarily scaled and vertically displaced) with increasing Tat mole fractions $x_{\text{Tat}}$ indicated on figure legends. Lipid mixtures: A. DOPC B. DOPC/DOPE (3:1) C. DOPC/DOPE (1:1) D. DOPC/DOPS (3:1) E. Nuclear mimic. The entire $q_z$ range is shown in C, while others show partial ranges. Solid vertical lines indicate the $q_z$ values where the form factors equal zero between the lobes of diffuse data. . . . .	32
3.10	The best fits to DOPC form factors (left) and the corresponding electron density profiles (right) with $x_{\text{Tat}} = 0, 0.016, 0.034$ , and $0.059$ (from top to bottom). . . . .	35
3.11	The best fits to DOPC:DOPE (3:1) form factors (left) and the corresponding electron density profiles (right) with $x_{\text{Tat}} = 0, 0.016, 0.034$ , and $0.059$ (from top to bottom). . . . .	36
3.12	The best fits to DOPC:DOPE (1:1) form factors (left) and the corresponding electron density profiles (right) with $x_{\text{Tat}} = 0, 0.016, 0.034$ , and $0.059$ (from top to bottom). . . . .	38
3.13	Modeling results for absolute electron density profiles and for the Tat location as a function of distance $z$ along the bilayer normal. A. DOPC B. DOPC:DOPE (3:1), and C. DOPC:DOPE (1:1). . . . .	39

3.14	A. Bilayer thickness, $D_{PP}$ ; B. Bilayer thickness, $D_{HH}$ ; C. Area/lipid, $A_L$ ; D. Twice the Tat location, $2z_{Tat}$ : all plotted vs. Tat mole fraction $x_{Tat}$ . Error bars are standard deviations from imposing Tat Gaussian widths, $\sigma_{Tat} = 2.5, 3.0$ or $3.5$ Å. Inverted blue triangles connected with dotted line are results from MD simulations, averaging the best fits to the X-ray data for each parameter, with standard deviations shown. .	41
3.15	$\chi^2$ as a function of $z_{Tat}$ for DOPC, DOPC:DOPE (3:1), and DOPC:DOPE (1:1) (from left to right) with $x_{Tat} = 0.016, 0.034$ , and $0.059$ (from top to bottom). $\sigma_{Tat} = 3.0$ . The THG model (black squares) and the THC model (red circles). . . . .	42
3.16	$\chi^2$ as a function of $z_{Tat}$ for DOPC with $x_{Tat} = 0.016, 0.034$ , and $0.059$ (from top to bottom). $\sigma_{Tat} = 3.0$ . The bound THG model was used. .	45
3.17	DPP graph with bound fits . . . . .	46
3.18	DHH graph with bound fits . . . . .	46
3.19	AL graph with bound fits . . . . .	46
3.20	$z_{Tat}$ graph with bound fits . . . . .	46
3.21	MD simulated form factors for DOPC at $A_L = 68$ Å <sup>2</sup> (blue solid line), $70$ Å <sup>2</sup> (red solid line), and $72$ Å <sup>2</sup> (green solid line) compared to the experimental form factor (open circles) scaled vertically to best match the form factor for $70$ Å <sup>2</sup> . . . . .	47
3.22	The simulated, symmetrized electron density profile for DOPC at $A_L = 70$ Å <sup>2</sup> as a function of the distance away from the bilayer center. Each component profile is labeled with its name: PC (phosphate-choline), CG (carbonyl-glycerol), CH <sub>2</sub> +CH (methylene-methine combination), CH <sub>3</sub> (terminal methyl). The sum of all the components is labeled as total. . . . .	48
3.23	MD simulated form factors for DOPC with $x_{Tat} = 0.015$ at $A_L = 72$ Å <sup>2</sup> (top) and $74$ Å <sup>2</sup> (bottom), with $z_{Tat} = 18$ Å (red solid lines), $16$ Å (green solid lines), and $14$ Å (blue solid lines) compared to the experimental form factor (open circles) scaled vertically to best match the form factor for $z_{Tat} = 18$ Å. . . . .	49

3.24	MD simulated form factors for DOPC with $x_{\text{Tat}} = 0.030$ at $A_L = 74 \text{ \AA}^2$ (top) and $76 \text{ \AA}^2$ (bottom), with $z_{\text{Tat}} = 18 \text{ \AA}$ (red solid lines), $16 \text{ \AA}$ (green solid lines), and $14 \text{ \AA}$ (blue solid lines) compared to the experimental form factor (open circles) scaled vertically to best match the form factor for $z_{\text{Tat}} = 18 \text{ \AA}$ . . . . .	50
3.25	Electron density profiles of guanidinium groups from the four best matched simulations for DOPC with $x_{\text{Tat}} = 0.015$ (one Tat on each leaflet). Tat on the lower and upper leaflets are shown on the left and right plots, respectively. . . . .	53
3.26	MD simulated form factors (red solid lines in A and C) of Tat/(DOPC+Tat), $x_{\text{Tat}}=0.030$ , with Tat fixed at $z_{\text{Tat}}= 18 \text{ \AA}$ (panel A) and $5 \text{ \AA}$ (panel C) from the bilayer center compared to experimental form factors (open circles) scaled vertically to provide the best fit to the simulations. Corresponding snapshots are shown in Panels B and D in which the lipid chains are represented as grey sticks on a white background, Tats are yellow, phosphate groups are red and water is blue. . . . .	54
3.27	Location of Tat in DOPC bilayer. Tat is represented as a cylinder, $z$ is the distance from the bilayer center, and $R$ is the in-plane distance from the center of Tat. The average $z$ of the lipid phosphates as a function of $R$ and the arginine guanidiniums are shown in red and blue, respectively. . . . .	55
4.1	Lattice structure of the asymmetric ripple phase. Unit cells are shown in dash lines. Center of bilayers are shown by thick, solid lines. Notations in the figure are ( <b>a</b> and <b>b</b> : lattice unit vectors), ( $D$ : $D$ -spacing along $z$ ), ( $\lambda_r =  \mathbf{b} $ : ripple wavelength), ( $\gamma$ : oblique tilt angle), ( $A$ : ripple amplitude), ( $\psi$ : chain tilt angle with respect to the $z$ direction), and ( $x_M$ : projected length of the major arm). . . . .	61
4.2	A picture of an annealing chamber. Need to take a picture . . . . .	63
4.3	The horizontal profile of the beam used in the low resolution study. Each pixel was $0.07113 \text{ mm}$ , which gave a CCD angular resolution $\Delta\theta$ of $0.0057^\circ$ , corresponding to $\Delta q = 0.0011 \text{ \AA}^{-1}$ at the sample to detector distance of $359.7 \text{ mm}$ . The beam FWHM = $1.7$ pixels, giving $\Delta\theta = 0.010^\circ$ or $\Delta q = 0.0019 \text{ \AA}^{-1}$ . . . . .	66

4.4	The vertical profile of the beam used in the low resolution study. The beam height = 15 pixels = 1.1 mm. . . . .	66
4.5	1 second exposure (left) and 60 second exposure (right) of the low angle X-ray scattering from the DMPC ripple phase in gray log scales. The index $h$ is labeled in green. $(3, k)$ reflections are identified in cyan. The shadow cast by 100 $\mu\text{m}$ thick molybdenum attenuator blocking strong $(1,0)$ and $(2,0)$ orders in the right image is labeled as attenuator and extends from $q_z = 0 \text{ \AA}^{-1}$ to $0.2 \text{ \AA}^{-1}$ . $D = 57.8 \text{ \AA}$ , $\lambda_r = 145.0 \text{ \AA}$ , and $\gamma = 97.8^\circ$ . . . . .	68
4.6	CCD images of X-ray scattering taken with (left) and without (right) a nominally 25 $\mu\text{m}$ thick Mo attenuator. These data were taken at a fixed angle of incidence $\omega = 0.8^\circ$ . The sample was an oriented film of DOPC:DOPE (3:1) in the fluid phase at $37^\circ\text{C}$ . The wavelength was $1.175 \text{ \AA}$ , the same as the one used for the ripple phase experiment. The same gray scale is used in both images. 100 pixel = $0.11 \text{ \AA}^{-1}$ in $q$ . A small dot located about $(p_x, p_z) = (520, 170)$ between the first and second orders is a specular reflection from the substrate. The exposure times were 1 second. . . . .	69
4.7	Vertical $p_z$ slices of X-ray images shown in Fig. 4.6 (left). The scattering intensity measured with the attenuator (red solid circles) was multiplied by a factor of 6.9 and compared to the intensity measured without the attenuator (black solid circles, right). . . . .	70
4.8	The horizontal profile of the beam used in the high resolution experiment. The CCD angular resolution $\Delta\theta = 0.0092^\circ$ corresponding to $\Delta q = 0.0017 \text{ \AA}^{-1}$ , at the sample to detector distance of 220.6 mm. The beam FWHM = 3.7 pixels = 0.26 mm, giving $\Delta\theta = 0.034^\circ$ or $\Delta q = 0.0063 \text{ \AA}^{-1}$ . . . . .	72
4.9	The vertical profile of the beam used in the high resolution experiment. The beam height = 9 pixels = 0.64 mm. . . . .	72

4.10	In-plane geometric broadening due to the sample width $w_s$ and the beam width $\Delta x_{\text{beam}}$ . A top view of the sample (green) on the Si wafer (gray) and the incoming and diffracted X-rays (bounded by red solid lines) are shown. The total in-plane scattering angle for a lipid chain-chain correlation is labeled as $2\theta$ , and the geometric broadening as $\Delta x$ . . . . .	73
4.11	Schematics of the sample holder in the transmission mode. Side (left) and top (right) views are shown. The thickness of the Si wafer = 35 $\mu\text{m}$ . The thickness of the sample $\approx 10 \mu\text{m}$ . The distance between the axis of rotation and sample = 21.1 mm. . . . .	74
4.12	Picture of the sample holder looking from above. A lead tape was attached to the back of the sample holder to help reduce the background scattering, typically coming from the air gap between the flightpath snout and the mylar window of the chamber. . . . .	75
4.13	Circular path followed by the sample as the angle of incidence $\omega$ was changed. The sample to detector distance and $D$ -spacing of the sample were measured in the LAXS mode, where $\omega = 1^\circ$ . WAXS images were collected at the transmission mode, where $\omega = -45^\circ$ . The $z$ position of the sample was slightly higher at the LAXS mode than at the transmission mode, so the sample holder was vertically shifted for different modes. . . . .	75
4.14	Geometric broadening in TWAXS. The cross section of the incoming X-ray with the sample and the CCD detector are both shaded in red. . . . .	76
4.15	Top view of geometric broadening in TWAXS. The cross section of the incoming X-ray with the sample is shaded in red. . . . .	76
4.16	Side view of geometric broadening in TWAXS. The cross section of the outgoing X-ray with the CCD detector is shaded in red. . . . .	77
4.17	Projection of rectangular beam on the detector. . . . .	77
4.18	Experimental reflectivity geometry. . . . .	80



4.19	Ewald sphere construction for the ripple phase diffraction in the low angle regime. A ripple $k = 0$ peak is the solid, black circle on the $q_z$ -axis. A ripple $k \neq 0$ ring is the black ring centered about the $q_z$ -axis. The portion of the ring that is inside the Ewald sphere is shown as a red dashed line and the portion of the ring that is outside but behind the Ewald sphere is shown as a black dotted line. The magnitude of the total scattering angle is exaggerated. With a wavelength of 1.175 Å, the magnitude $ \mathbf{k}_{\text{in}}  = 5.35 \text{ Å}^{-1}$ . For a $h = 5$ peak, $q_{50}^z = 0.54 \text{ Å}^{-1}$ , one tenth of $k_{\text{in}}$ . . . . .	82
4.20	Side view of an arc of $k = 0$ peak shown as a thick blue line. . . . .	83
4.21	$q$ -space representations of Bragg peaks and Bragg rings for $h = 1$ and $2$ and $k = 0, 1$ , and $2$ in $q_{hk}^z$ planes. The intersection between the Ewald sphere and a Bragg peak/ring is indicated in red. The observed intensity for the $k \neq 0$ orders is proportional to the fraction of the length of red arcs in the circumference. This fraction is equal to one for $k = 0$ reflections. Because the reflections are not in the same $q_z$ plane, the range of $q_y$ integration indicated by the height of the gray rectangle is different for different $h$ orders. For $\gamma \neq 90^\circ$ , the range of $q_y$ integration is slightly different for different $k$ reflections with the same $h$ . The values shown are for $D = 58 \text{ Å}$ , $\lambda_r = 145 \text{ Å}$ , $\gamma = 90^\circ$ , and $\lambda = 1.175 \text{ Å}$ . The magnitude of curvature of arcs is exaggerated. . . . .	84
4.22	The path of X-rays within the sample. The incident angle is $\omega$ and the total scattering angle is $2\theta$ . An X-ray with a penetration depth of $z$ is shown. The total thickness of the sample is $t$ . . . . .	87
4.23	Absorption factors as a function of $q_z \approx 4\pi\theta/\lambda$ . Values at $q_z = 2\pi h/D$ corresponding to $D = 57.8 \text{ Å}$ are shown as squares. $\mu = 2600 \text{ μm}$ , $t = 10 \text{ μm}$ , and $\lambda = 1.175 \text{ Å}$ . . . . .	89
4.24	Contours of a mosaic spread distribution projected on the $xy$ -plane. The distribution function takes a form of Lorentzian centered at $\alpha = 0$ . Domains with $\alpha = 0$ are probed at $\omega = \theta_B$ and $\chi = 0$ . Integrated intensity of $(1,0)$ reflection is proportional to the green shaded area while that of $(3,0)$ reflection is proportional to the blue shaded area, which is three times larger. The rocking scan axis is centered at $\theta_B$ . . . . .	91
4.25	Mosaic factor given by Eq. (4.35) as a function of $q_z \approx 4\pi\theta/\lambda$ . . . . .	92

4.26	title goes here . . . . .	94
4.27	NGIWAXS of the DMPC ripple phase for $D = 59.2 \text{ \AA}$ (left) and $60.8 \text{ \AA}$ (right). The angle of incidence $\omega$ was $0.2^\circ$ . The black regions around the edge of each image are the $q$ -space that was not probed. The distorted, non rectangular shape of the probed $q$ -space signifies non-linear relation between the CCD space and sample $q$ -space. . . . .	100
4.28	Enlarged view of the right image in Fig. 4.27. To show smaller features around the peak, a different contrast is used. . . . .	101
4.29	$q_r$ swaths, each averaged over $0.02 \text{ \AA}^{-1}$ . The center $q_z$ value of a swath is shown in the figure legends. . . . .	102
A.1	Two dimensional view of mosaic spread (left) and notations used in this section (right). The stacking direction of an ideal domain is $\mathbf{n}$ and that of a tilted domain $\mathbf{n}'$ . The deviation of $\mathbf{n}'$ from $\mathbf{n}$ denoted as $\alpha$ quantifies the degree of misorientation of a domain. The $x$ , $y$ , and $z$ -axes are the sample coordinates. . . . .	106
A.2	Example of a two dimensional sample consisting of an ideal and tilted domains. $\mathbf{q} = (q_x, q_z)$ is the sample $q$ -space and $\mathbf{q}' = (q'_x, q'_z)$ is the domain $q$ -space. The two $q$ -spaces are related by a rotation of $\alpha$ about the $y$ -axis, which is into the page. . . . .	107
A.3	Notations used in this section. The arc originating from the $Z$ -axis is the mosaic arc due to the mosaic spread distribution. . . . .	110
A.4	Rocking scan trace in $q$ -space. . . . .	111

# Chapter 1

## Introduction

Lipids are amphiphilic molecules, consisting of hydrophilic headgroup and hydrophobic chains. There are various kinds of lipids. These can be categorized in terms of headgroup, chain length, and chain saturation.

In water lipids self-assemble into lipid bilayers to shield their hydrophobic cores. Lipid bilayers are the building blocks of cell membranes. Lipid bilayers take various thermodynamic phases as temperature and hydration are varied as shown in Fig. 1.1. At higher temperature, lipids are in fluid phase. In this phase, chains are flexible. Lipid bilayers are also flexible and fluctuating. This flexibility of lipid bilayers make many interesting biological phenomena possible.

As the temperature is reduced, lipid bilayers go into the gel phase. In this phase, chains are straightened out and bilayers are rigid.

Between the fluid and gel phases, some lipids have the ripple phase. This phase is found in saturated lipids. In this phase, the bilayer height is modulated in a periodic manner in the in-plane direction. Each bilayer is registered along its orthogonal direction.

In this thesis, we focus on the fluid and ripple phase. In the former phase, we investigated the interaction of a peptide called Tat with lipid bilayers in the fluid phase. Tat is discussed in chapter 3. Regarding the ripple phase, we measured the electron density profile of the lipid bilayers using a stack of oriented bilayers. Using wide angle x-ray scattering technique, we also investigated the chain packing within

Figure 1.1: Experimental phase diagram of DMPC from Ref. [1].

a bilayer. The ripple phase is discussed in chapter 4. The appendices show a lot of details that will allow other people to reproduce much of the results shown in this thesis as well as help readers understand scattering analysis employed in this work. It is my hope that these details will help future researchers, especially students, understand some of the techniques to investigate the structure of lipid bilayers in sub Angstrom resolution.

# Chapter 2

## Materials and Methods

This chapter describes parts of experimental techniques that are common in both Tat and ripple phase projects. These common parts are also the key experimental components that make experiments on oriented samples successful. Experimental and theoretical methods that are specific to each project are described in each respective chapter.

### 2.1 X-ray optics

Low resolution setup should be described.

### 2.2 Hydration Chamber

Probably the most important of all. The chamber is sealed very tightly. We used helium to replace air. Air scattering is strong. Mylar window, cast scattering in wide angle region. Helium. Peltier used to condense water in and out of the sample.

The sample was placed on a Peltier element that was connected to a controllable power supply and a multimeter was connected to read off the applied current. In order to achieve a desired hydration of the sample, small current was applied to the Peltier. The applied current caused the Peltier surface to either heat or cool depending on the direction of the current. The sample became less hydrated with the heated Peltier surface while it became more hydrated with the cooled Peltier surface. The temperature gradient caused by the Peltier was negligible (less than 0.1 °C). The

hydration level of the sample was quantified by the average inter-bilayer distance,  $D$ -spacing, which was measured by indexing observed peaks in X-ray scattering.

## 2.3 Sample Preparation

### 2.3.1 Stock Solutions

Synthesized lipids were purchased from Avanti Polar Lipids (Alabaster, AL) and used without further purification. Membrane mimics for Tat experiments were prepared by first dissolving lyophilized lipids in chloroform and then mixing these stock solutions to create the lipid compositions DOPC, DOPC/DOPE (3:1), DOPC/DOPE (1:1), DOPC/DOPS (3:1) and nuclear membrane mimic (POPC/POPE/POPS/SoyPI/Cholesterol, 69:15:2:4:11) (based on Ref. [37]). Peptide (Y47GRKKRRQRRR57) was purchased in two separate lots from the Peptide Synthesis Facility (University of Pittsburgh, Pittsburgh, PA); mass spectroscopy revealed greater than 95% purity. This Tat peptide corresponds to residues (47-57) of the 86 residues in the Tat protein [6]. Tat was dissolved in HPLC trifluoroethanol (TFE) and then mixed with lipid stock solutions in chloroform to form mole fractions between 0.0044 and 0.108. Weight of Tat in these mole fractions was corrected for protein content (the remainder being 8 trifluoroacetate counter-ions from the peptide synthesis). Solvents were removed by evaporation in the fume hood followed by 2 hours in a vacuum chamber at room temperature.

### 2.3.2 Thin Film Samples

For Tat experiments, four mg dried lipid/peptide mixture was re-dissolved in HPLC chloroform/TFE (2:1 v:v) for most of the lipid compositions. DOPC/DOPS (3:1) mixtures required chloroform/HFP (1:1 v:v) in order to solubilize the negatively charged DOPS. 200  $\mu$ l of 4 mg mixtures in solvents were plated onto silicon wafers (15x30x1 mm) via the rock and roll method [38] to produce stacks of  $\approx$ 1800 well-aligned bilayers; solvents were removed by evaporation in the fume hood, followed by two hours under vacuum. Samples were prehydrated through the vapor in polypropylene hydration chambers at 37 °C for two to six hours directly before hydrating in the thick-walled X-ray hydration chamber [39] for 0.5 to 1 hour.

For ripple phase experiments, four mg DMPC powder was dissolved in 140  $\mu$ l chloroform/methanol (2:1 v:v) mixture. The solution was plated onto silicon wafers similarly to Tat mixtures. The sample was annealed at 60 °C for approximately 6-10 hours just before the X-ray experiment. Then, the sample was trimmed to 1 mm for high resolution and 5 mm for low resolution study. The temperature was set to 18 °C.

## **2.4 CCD detector**

Data reduction and correction for charged coupled device (CCD) detector are described in detail in [?].

# Chapter 3

## Structural Perturbation of Lipid Bilayers Due to Tat Peptide

### 3.1 Introduction

The name cell-penetrating peptide (CPP) connotes a peptide that easily penetrates cell membranes (for Reviews see [2–4]).

This thesis focuses on the transactivator of translation, Tat, from the HIV-1 virus, which plays a role in AIDS progression. Earlier work showed that the HIV-Tat protein (86 amino acids) was efficiently taken up by cells, and concentrations as low as 1 nM were sufficient to transactivate a reporter gene expressed from the HIV-1 promoter [5, 6]. It has been reported that Tat protein uptake does not require ATP [7]. Studies using inhibitors of different types of endocytosis, including clathrin and caveolae-mediated, or receptor-independent macropinocytosis reached the same conclusion that ATP mediated endocytosis is not involved in Tat protein permeation [?, 8–10]. However, this issue is controversial, as other studies found evidence for endocytosis in Tat protein import [11–19]. Still other studies have concluded that an ATP requirement for Tat protein entry depends on the size of the cargo attached to Tat protein, or on the specific cell type [20–22]. The part of the Tat protein responsible for cellular uptake was assigned to a short region Tat (48–60), G<sub>4</sub>8RKKRRQRRRPPQ<sub>60</sub>, which is particularly rich in basic amino acids [7]. Deletion of three out of eight positive charges in this region caused loss of its ability to translocate [7]. In this chapter, short basic regions will be called Tat, while the entire



86 amino acid protein will be called Tat protein. Tat was shown to be responsible for the Tat proteins permeation into the cell nucleus and the nucleoli [7], and this was confirmed using live cell fluorescence in SVGA cells [23]. Tat (48-60) was shown to have little toxicity on HeLa cells at 100  $\mu$ M concentration [7], but the longer Tat protein (2-86) was toxic to rat brain glioma cells at 1-10  $\mu$ M [24]. Interestingly, no hemolytic activity was found when human erythrocytes were incubated with a highly neurotoxic concentration (40  $\mu$ M) of Tat (2-86) [24]. These results prompt the question, what is the mechanism of Tatts translocation through membranes? To address this question, many biophysical studies have used simple models of biological membranes composed of a small number of lipid types. These studies are valuable because there is no possibility for ATP-dependent translocation, thus ruling out endocytosis if translocation occurs. For example, Mishra et al. reported that the rate of entry into giant unilamellar vesicles (GUVs) composed of PS/PC (1:4 mole ratio) lipids of rhodamine-tagged Tat is immeasurably slow, but it crosses a GUV composed of PS/PC/PE (1:2:1) lipids within 30 seconds [25]. This study suggests that negative curvature induced by the inclusion of PE facilitates translocation. In a subsequent study using much smaller unilamellar vesicles (LUVs), Tat did not release an encapsulated fluorescent probe in LUVs composed of lipids modeling the outer plasma membrane, PC/PE/SM/Chol (1:1:1:1.5), but did release the probe in LUVs composed of BMP/PC/PE (77:19:4) [26]; BMP (bis(monoacylglycero)-phosphate) is an anionic lipid specific to late endosomes. In that study [26], the inclusion of PE did not suffice to cause leaky fusion in LUVs in the absence of a negatively charged lipid. The contrasting results in these two experiments may also be due to the use of LUVs instead of GUVs since it was reported that Tat does not translocate across LUVs of PC/PG (3:2) but does translocate across GUVs of the same lipid composition [27]. In a similar experiment, Tat did not translocate into egg PC LUVs [28]. In another experiment confirming these results, Tat did not translocate into GUVs containing only PC with 20 mol% cholesterol, but when PS or PE was included with PC, then rapid translocation of Tat was observed [29]. These experiments demonstrate that the choice of lipids and model systems influences Tat translocation.

Is a pore formed during Tat translocation? Although direct conductance measurements of Tat and lipid membranes have not been carried out, two studies measured conductance with the somewhat similar CPP oligoarginine R<sub>9</sub>C peptide. Using single-channel conductance of gramicidin A in planar lipid membranes consisting of anionic,

neutral or positively charged lipids, R<sub>9</sub>C did not increase conductance, even in anionic lipid membranes [30]. By contrast, in a similar experiment using planar lipid membranes, a current was induced by R<sub>9</sub>C in PC/PG (3:1) membranes, with increasing destabilization over time [31]. Thus questions remain about pore formation of Tat in membranes. In the GUV experiment with Tat mentioned above [29], Ciobanasu *et al.*, using size exclusion methods, suggested a pore in the nanometer range, which could only be passed by small dye tracer molecules. Thus, if a true pore forms, it is likely to be small and transitory.

The secondary structure of Tat has been characterized by many researchers. Ref. [27] carried out Circular dichroism (CD) spectroscopy on a variation of Tat where the penultimate proline on Tat (48-60) was replaced by a tryptophan [27]. Their study found a random coil secondary structure in aqueous solution as well as when Tat was mixed with PC/PG/PE (65:35:5) LUVs. Ziegler *et al.* [10] obtained the same result using CD in PC/PG (3:1) vesicles. In addition, solid state NMR has identified a random coil structure of Tat in DMPC/DMPG (8:7 mole ratio) multibilayers [32]. In the larger Tat-(1-72)-protein NMR measurements at pH 4 have determined there is no secondary structure, with a dynamical basic region [33]. Similarly, NMR was used to study the full Tat protein and found a highly flexible basic region [34]. These previous studies indicate that an alpha helix is not required for Tats translocation ability.

Regarding the mechanism of translocation of this randomly structured, short basic peptide, many models have been proposed based on the conflicting results listed above. Molecular dynamics simulations offer some insight into the molecular details of translocation. Hecce and Garcia simulated the translocation of Tat (Y<sub>47</sub>GRKKRRQRRR<sub>57</sub>) across DOPC at various lipid:peptide molar ratios [35]. Their simulations indicated that Tat binds to the phosphate headgroups, with 1 Tat binding with 14 lipids, each positive charge on Tat associated with nearly 2 phosphate groups [35]. Translocation involved a localized thinning, and snorkeling of arginine side chains through the hydrophobic layer to interact with phosphates on the other side of the membrane. This allowed some water molecules to penetrate the membrane along with Tat, forming a pore [35]. In this simulation, performed without inclusion of counterions, pore formation was only observed at high ratios of peptide:lipid (1:18) or at elevated temperature. However, a subsequent Gromacs simulation with counterions found no thinning and no pore formation when Tat was added to DOPC

membranes [36]. Instead it found a membrane invagination associated with a cluster of Tat peptides. From their findings, the authors suggested that micropinocytosis could be the model for Tat translocation across membranes [36].

In this thesis, I combine experimental low-angle X-ray scattering (LAXS) data with MD simulations to obtain the structure of fully hydrated, oriented lipid bilayers with Tat (47-57) added at several mole ratios. The lipid systems were DOPC, DOPC/DOPE (3:1 mole ratio), DOPC/DOPS (3:1), DOPC/DOPE (1:1) and a mimic of the nuclear membrane (POPC/POPE/POPS/SoyPI/Chol, 69:15:2:4:11).

## 3.2 Materials and Methods

### 3.2.1 Volume Measurements

Multilamellar vesicles (MLVs) were prepared by mixing dried lipid mixtures with MilliQ water to a final concentration of 2-5 wt% in nalgene vials and cycling three times between 20 °C and 60 °C for ten minutes at each temperature with vortexing. Pure Tat was dissolved in water at 0.4 wt%.

Volumes of lipid mixtures with and without peptides in fully hydrated multilamellar vesicles (MLV) were determined at  $37 \pm 0.01$  °C using an Anton-Paar USA DMA5000M (Ashland, VA) vibrating tube densimeter. This instrument measures the average density of a solution and compares it to the density of air using  $\rho_s - \rho_0 = k(\tau_s - \tau_0)^2$  where  $k$  is an instrumental ??? that depends on the atmospheric pressure.

The Tat peptide sequence used in X-ray experiments and MD simulations was Y<sub>47</sub>GRKKRRQRRR<sub>57</sub>. Table 3.1 lists the chemical formulas and molecular weights of these amino acids for convenience. The molecular weight of this sequence is  $181.2 + 75.1 + 146.1 + 2 \times 146.2 + 6 \times 174.2 - 10 \times 18 = 1560$ . The Tat peptides were synthesized in trifluoroacetic acid, which has the chemical formula CF<sub>3</sub>CO<sub>2</sub>H, and is made into a powder form by the freeze-dry method. Therefore, each positively charged amino acid such as an arginine and lysine was counter-balanced by a trifluoroacetate (TFA) (C<sub>2</sub>F<sub>3</sub>O<sub>2</sub>). Since Tat has six arginines and two lysines, it came with eight trifluoroacetates. This complex has a molecular weight of  $1560 + 113 \times 8 = 2464$ . We used the molecular weight of this complex in order to calculate the molarity of Tat correctly. The same molecular weight was also used in preparing oriented samples.

The Tat volume  $V_{\text{Tat}}$  was calculated from the measured average density of a Tat-

Code	Amino acid	Chemical Formula	Molecular weight (g/mol)
K	Lysine	$\text{C}_6\text{H}_{14}\text{N}_2\text{O}_2$	146.2
R	Arginine	$\text{C}_6\text{H}_{14}\text{N}_4\text{O}_2$	174.2
G	Glycine	$\text{C}_2\text{H}_5\text{NO}_2$	75.1
Y	Tyrosine	$\text{C}_9\text{H}_{11}\text{NO}_3$	181.2
Q	Glutamine	$\text{C}_5\text{H}_{10}\text{N}_2\text{O}_3$	146.1

Table 3.1: Some Amino Acids Data

water solution in the following way. Assuming that Tat molecules in water do not change the volume of water molecules, the density of Tat-water solution is equal to the mass of Tat-water solution divided by the sum of volumes of water and Tat,

$$\rho_{\text{sol}} = \frac{m_{\text{w}} + m_{\text{c}}}{V_{\text{w}} + V_{\text{c}}N_{\text{c}}}, \quad (3.1)$$

where  $m_{\text{w}}$  and  $m_{\text{c}}$  are the total masses of water and Tat-TFA complex, respectively,  $V_{\text{w}}$  is the total volume of water,  $V_{\text{c}}$  is the molecular volume of a Tat-TFA complex, and  $N_{\text{c}}$  is the total number of this complex in the solution. Denoting  $V_{\text{w}} = m_{\text{w}}/\rho_{\text{w}}$  and  $N_{\text{c}} = N_{\text{A}}m_{\text{c}}/W_{\text{c}}$ , where  $W_{\text{c}}$  is the molecular weight of the complex,  $N_{\text{A}}$  is the Avogadro's number, and  $\rho_{\text{w}}$  is the density of water, we have

$$V_{\text{c}} = \frac{W_{\text{c}}}{\rho_{\text{sol}}N_{\text{A}}} \left( 1 + \frac{m_{\text{w}}}{m_{\text{c}}} \left( 1 - \frac{\rho_{\text{sol}}}{\rho_{\text{w}}} \right) \right), \quad (3.2)$$


which allows us to calculate the molecular volume of a Tat-TFA complex from the experimentally measured quantities. Assuming that the molecular volume scales with the molecular weight gives the volume of Tat,  $V_{\text{Tat}} = 1560/2464 \times V_{\text{c}} \text{ \AA}^3$ .

### 3.2.2 Analysis of Diffuse Scattering

Figure 3.1 shows our typical Low angle X-ray scattering (LAXS) data from oriented stacks of fluctuating bilayers in the fluid phase. Analysis of diffuse scattering intensity patterns like the one shown in Fig. 3.1 results in material parameters such as the bending modulus  $K_{\text{c}}$  and bulk modulus  $B$  as well as the absolute form factor  $|F(q_z)|$ . The form factor is the Fourier transform of the bilayer electron density profile  $\rho(z)$  and gives us information about the internal structure of the bilayers interacting with Tat peptides.

The form factor  $F(q_z)$  is obtained by realizing that the diffuse scattering intensity pattern  $I(\mathbf{q})$  is a product of the structure factor  $S(\mathbf{q})$  and the form factor;  $I(\mathbf{q}) = S(\mathbf{q})|F(q_z)|^2$ . This means that once the two dimensional structure factor map  $S(\mathbf{q})$  is calculated from a model free energy for bilayer fluctuations, the form factor can simply be calculated by dividing the intensity by the structure factor. Getting the best fit of a model structure factor to the intensity results in the material parameters,  $K_{\text{c}}$  and  $B$ .

We used an analysis program called NFIT developed by Dr. Yufeng Liu [37–39]



figures/Tat/figure1.pdf

Figure 3.1: LAXS of DOPC:DOPE (1:1) with  $x_{\text{Tat}} = 0.034$  at 37 °C. White lobes of diffuse scattering intensity have large grey numbers, while lamellar orders and beam are shown to the left of the molybdenum beam attenuator (short, dark rectangle).  $q_z$  and  $q_r$  are the cylindrical coordinates of the sample  $q$ -space, where  $q_z$ -axis is along the bilayer normal and  $q_r$ -axis is along the in-plane direction. The lamellar repeat spacing was  $D = 66.2 \text{ \AA}$ .

to analyze the diffuse scattering and obtain the bending modulus, bulk modulus, and form factor. The details of the analysis are found in Dr. Yufeng Liu's thesis [39]. This section outlines the method.

X-ray scattering essentially reflects the electron density distribution of the sample system. This includes not only the average electron density but also the disorder caused by fluctuations about the average. In our samples, the electron density distribution reflects the stacking of the bilayers, whose average structure can be described as a one-dimensional array of membranes, each of which is a two-dimensional in-plane fluid. A sketch of the membrane stack is shown in Fig. 3.2.



Figure 3.2: Schematic of an oriented stack of lipid bilayers. Thick green curves represent an instance of thermally fluctuating bilayers. The dashed lines show the thermally averaged positions  $z = nD$  of the centers of each bilayer and  $u_n(x, y)$  gives the instantaneous deviation from the average. Each bilayer extends in the  $\mathbf{r} = (x, y)$  plane.

Fluctuations in the stack of the bilayers are described by the quantities  $u_n(\mathbf{r})$ , which are the spatial deviations of the center of the  $n$ -th bilayer from its average position in the  $z$  direction at the in-plane location  $\mathbf{r} = (x, y)$ . Given this description of structure of the lipid bilayer system, we write the electron density  $\rho_n$  of the  $n$ -th bilayer as

$$\rho_n(z, r) = \rho(z - nD - u_n(\mathbf{r})) \quad (3.3)$$

where  $\rho(z)$  is the electron density profile of a single, flat (no fluctuations) bilayer centered at  $z = 0$  with its normal in the  $z$  direction. Eq. (3.3) is not quite accurate for an incompressible fluid phase bilayers because it ignores the  $\cos \alpha$  factor [39] (see Fig. 3.3). To correct for the absence of this factor, the undulation correction [40] was applied to all our form factors in this thesis. For a typical sample, this correction is

about 2% [39]. We then write the electron density of a stack of  $N$  bilayers,

$$\rho(\mathbf{R}) = \sum_{n=0}^{N-1} \rho_n(z, \mathbf{r}). \quad (3.4)$$

figures/Tat/stack2.pdf

Figure 3.3: Expanded view of a fluctuating bilayer. Along the two black solid lines, the electron density profile is identical in an incompressible bilayer. Along the dashed line, the bilayer appears thicker by a factor  $1/\cos \alpha$ . This apparent thickness variation along the  $z$  direction is corrected by the undulation correction.

Basic X-ray scattering theory in the usual Born approximation gives

$$\begin{aligned} I(\mathbf{q}) &\propto \int d\mathbf{R} d\mathbf{R}' \rho(\mathbf{R}) \rho(\mathbf{R}') e^{i\mathbf{q} \cdot (\mathbf{R} - \mathbf{R}')} \\ &= \left| \int_V d^3\mathbf{R} \rho(\mathbf{R}) e^{i\mathbf{q} \cdot \mathbf{R}} \right|^2, \end{aligned} \quad (3.5)$$

where  $\rho(\mathbf{R})$  is the electron density distribution function of a stack of bilayers. Because X-ray scattering measures integrated intensity over time, Eq. (3.5) requires thermal averaging indicated by angular brackets,

$$I(\mathbf{q}) = \left\langle \left| \int_V \rho(\mathbf{R}) e^{i\mathbf{q} \cdot \mathbf{R}} d^3\mathbf{R} \right|^2 \right\rangle. \quad (3.6)$$

Using Eq. (3.3) and (3.4), it can be shown that [39]

$$I(\mathbf{q}) = |F(q_z)|^2 S(\mathbf{q}) \quad (3.7)$$

where

$$S(\mathbf{q}) = \left\langle \left| \sum_{n=0}^{N-1} \int e^{inDq_z + iu_n(\mathbf{r})q_z + i\mathbf{q}_r \cdot \mathbf{r}} d^2\mathbf{r} \right|^2 \right\rangle, \quad (3.8)$$



and

$$\begin{aligned} F(q_z) &= \int_V \rho(z) e^{iq_z z} dz \\ &= \int \rho(z) \cos(q_z z) dz. \end{aligned} \quad (3.9)$$

The second equality in Eq. (3.9) follows for centro-symmetric lipid bilayers. Assuming that  $u_n(\mathbf{r}) - u_m(\mathbf{r}')$  has a normal distribution, we write Eq. (3.8) as

$$S(\mathbf{q}) = \sum_{n,m=0}^{N-1} e^{iq_z(n-m)D} \int_V d^2\mathbf{r} d^2\mathbf{r}' e^{i\mathbf{q}_r \cdot (\mathbf{r}-\mathbf{r}')} G(r, r', n, m), \quad (3.10)$$

where

$$\begin{aligned} G &= \left\langle e^{iq_z(u_n(\mathbf{r}) - u_m(\mathbf{r}'))} \right\rangle \\ &\approx e^{-\frac{q_z^2 \langle [u_n(\mathbf{r}) - u_m(\mathbf{r}')]^2 \rangle}{2}}. \end{aligned} \quad (3.11)$$

$G$  is called the scattering pair correlation function. The second approximation is obtained by employing the harmonic approximation [39]. Eq. (3.10) is an general expression for a system whose electron density distribution has the form given by Eq. (3.3) and (3.4).

The membrane fluctuations given by  $\langle [u_n(\mathbf{r}) - u_m(\mathbf{r}')]^2 \rangle$  in Eq. (3.11) are calculated from the free energy functional for smectic liquid crystals. The basic degrees of freedom in this free energy include (1) bending of each membrane independently of others in the stack and (2) interactions between membranes in the stack. The bending free energy is proportional to the curvature squared with a bending modulus  $K_c$  as shown in the first term in the following free energy equation

$$F_U = \frac{1}{2} \int d\mathbf{r} \sum_{n=0}^{N-1} \left\{ K_c [\nabla_r^2 u_n(\mathbf{r})]^2 + B [u_{n+1}(\mathbf{r}) - u_n(\mathbf{r})]^2 \right\}. \quad (3.12)$$

The second term is a harmonic approximation to the interactions between membranes with a modulus  $B$ . From analysis of X-ray data,  $K_c$  and  $B$  are determined.

From the free energy functional, we calculate the pair correlation function  $G$ . We

consider the Fourier representation of the displacement variables  $u$

$$u_n(r) = \sum_{\mathbf{Q}} U(\mathbf{Q}) e^{i\mathbf{Q}_r \cdot \mathbf{r} + iQ_z nD} \quad (3.13)$$

where  $Q_z$  takes the discrete value of  $Q_z = \frac{2\pi m}{DN}$  ( $m = -N/2 + 1, \dots, -1, 0, 1, \dots, N/2$ ) (where we use  $\mathbf{Q}$  to distinguish the Fourier space of the sample from the Fourier space  $\mathbf{q}$  of the scattering). The sum in Eq.(3.13) includes both an integration over  $\mathbf{Q}_r$  and a sum over  $Q_z$ .

Because the model is harmonic, Eq. (3.13) allows us to express the free energy in normal modes. Then, it can be shown that applying the equipartition theorem of statistical physics leads to

$$\langle U(\mathbf{Q}_r, Q_z) U(\mathbf{Q}'_r, Q'_z) \rangle = \frac{1}{A_r N} \frac{k_B T}{K_c Q_r^4 + 4B \sin^2(Q_z D/2)} \delta_{\mathbf{Q}_r + \mathbf{Q}'_r, 0} \delta_{Q_z + Q'_z, 0}. \quad (3.14)$$

$\langle [u_n(\mathbf{r}) - u_m(\mathbf{r}')]^2 \rangle$  can be written in terms of  $\langle U(\mathbf{Q}) U(\mathbf{Q}') \rangle$ . After some lengthy calculus [39], we arrive at

$$\begin{aligned} & \langle [u_n(\mathbf{r}) - u_m(\mathbf{r}')]^2 \rangle \\ &= \frac{D^2 \eta}{2\pi^2} \int_0^\infty dx \frac{1 - J_0(\sqrt{2x} |r - r'| / \xi) (\sqrt{1 + x^2} - x)^{2|n-m|}}{x \sqrt{1 + x^2}}. \end{aligned} \quad (3.15)$$

where  $\eta = \pi k_B T / (2D^2 \sqrt{K_c B})$ ,  $\xi^4 = K_c / B$ , and  $J_0(x)$  is the first order Bessel function. Essentially, Eq. (3.7), (3.10), (3.11), and (3.15) relate the X-ray data to the material parameters,  $K_c$  and  $B$ . Through a non-linear least square fitting, the values of  $K_c$  and  $B$  that yield the best fit of the model to the data are obtained. From these values, the absolute form factor  $|F(q_z)|$  is calculated.

### 3.2.3 Modeling the Bilayer Structure

In the case of X-rays, the features with the most contrast are the electron-dense headgroups, providing the head-head spacing  $D_{\text{HH}}$ , and also the terminal methyl groups in the bilayer center with the least electron density. Modeling of the bilayer structure was done similarly to the SDP model written by Dr. Norbert Kucerka when he was a postdoc in the Nagle/Tristram-Nagle lab [41].

Parsing of DOPC into lipid components is shown in Fig. 3.4. The phosphate/choline (PC) and carbonyl/glycerol (CG) components together make up the lipid headgroup whereas the hydrocarbon chain region (HC) is divided into two components, the methylene ( $\text{CH}_2$ ) and methine (CH) group combination (denoted as  $\text{CH}_2+\text{CH}$ ) and terminal methyl groups ( $\text{CH}_3$ ). We combine methylene ( $\text{CH}_2$ ) and methine groups (CH) in order to avoid proliferation of fitting parameters.

#### Functional forms

Our model for the electron density profile (EDP) of Tat/lipid bilayer system consists of five structural subgroups: PC, CG,  $\text{CH}_2+\text{CH}$ ,  $\text{CH}_3$ , and Tat (see Fig. 3.5). The volume probability distributions of components PC, CG,  $\text{CH}_3$ , and Tat are described by Gaussian functions,

$$P_i(z) = \frac{c_i}{\sqrt{2\pi}} \left( \exp\left\{-\frac{(z+z_i)^2}{2\sigma_i^2}\right\} + \exp\left\{-\frac{(z-z_i)^2}{2\sigma_i^2}\right\} \right), \quad (3.16)$$

where  $c_i$  is an integrated area underneath the curve and the two parts of the expression describe the two bilayer leaflets.

The hydrocarbon chain region (HC) is represented by error functions,

$$P_{\text{HC}}(z) = \frac{1}{2} [\text{erf}(z, -z_{\text{HC}}, \sigma_{\text{HC}}) - \text{erf}(z, z_{\text{HC}}, \sigma_{\text{HC}})], \quad (3.17)$$

where

$$\text{erf}(z, z_i, \sigma_i) = \frac{2}{\sqrt{\pi}} \int_0^{\frac{z-z_i}{\sqrt{2}\sigma}} dx e^{-x^2}. \quad (3.18)$$


The volume probability distribution for the methylene and methine group combination can then be expressed as

$$P_{\text{CH}_2+\text{CH}}(z) = P_{\text{HC}}(z) - P_{\text{CH}_3}(z). \quad (3.19)$$

The image is a schematic diagram of a 1,3-bis(sn-3'-phosphatidyl)-sn-glycerol (DOPC) molecule. It is represented as a large, empty rectangular box. Inside the box, the text 'figures/Tat/dopc\_schematic.pdf' is displayed in a monospaced font. This text likely serves as a placeholder for the actual schematic diagram, which would illustrate the chemical structure of the lipid and its division into components like the phosphate-choline (PC) headgroup, carbonyl-glycerol (CG) headgroup, methylene+methine (CH<sub>2</sub>+CH) hydrocarbon chain, and terminal methyl groups (CH<sub>3</sub>).

figures/Tat/dopc\_schematic.pdf

Figure 3.4: Schematic of DOPC showing each lipid component. The dash lines show where the lipid is divided into different components. The lipid headgroup is divided into two components, phosphate-choline (PC) and carbonyl-glycerol (CG). The hydrocarbon chain region is also divided into two components, methylene+methine ( $\text{CH}_2+\text{CH}$ ) and terminal methyl groups ( $\text{CH}_3$ ).



figures/Tat/SDP\_Results/EDP/DOPC\_Tat\_model\_EDP.pdf

Figure 3.5: A model electron density profile for DOPC with Tat.

This definition enforces the total probability  $P_{\text{HC}}$  in the hydrocarbon chain region to equal one, which in turn means that placement of Tat in the chain region is prohibited. We call the model defined by Eq. (3.19) model A. To allow Tat to be placed inside the hydrocarbon chain region, we also consider an alternative definition,

$$P_{\text{CH}_2+\text{CH}}(z) = P_{\text{HC}}(z) - P_{\text{CH}_3}(z) - P_{\text{Tat}}(z), \quad (3.20)$$

where the volume probability of  $\text{CH}_2+\text{CH}$  combined component is reduced by the Tat volume probability distribution. We call this model B. The spatial conservation requires the water volume probability distribution to be

$$P_{\text{W}}(z) = 1 - P_{\text{PC}}(z) - P_{\text{CG}}(z) - P_{\text{Tat}}(z) - P_{\text{HC}}(z) \quad (3.21)$$

for model A and

$$P_{\text{W}}(z) = 1 - P_{\text{PC}}(z) - P_{\text{CG}}(z) - P_{\text{HC}}(z) \quad (3.22)$$

for model B.

Because X-rays measure the contrast between the bilayer and surrounding solvents, water, the experimental form factor is compared to the water subtracted model form factor,

$$F(q_z) = 2 \int_0^{\frac{D}{2}} dz \left( \sum_i (\rho_i - \rho_{\text{W}}) P_i(z) \right) \cos(q_z z), \quad (3.23)$$

where  $i = \text{PC}, \text{CG}, \text{Tat}, \text{CH}+\text{CH}_2$ , and  $\text{CH}_3$ .

## Constraints

The height of the hydrocarbon chain error function is fixed to one by imposing spatial conservation, whereas the mean position of the terminal methyls is fixed to  $z_{\text{CH}_3} = 0$  by symmetry arguments. The total lipid volume  $V_{\text{L}}$  is fixed to the experimentally measured value. The headgroup volume  $V_{\text{HL}}$  was determined to be  $331 \text{ \AA}^3$  for gel phase phosphatidylcholine (PC) bilayers [42], and we assume the same volume for the fluid phase PC bilayers. The volumes of PC and CG components satisfy

$$V_{\text{PC}} + V_{\text{CG}} = V_{\text{HL}}, \quad (3.24)$$

and the volumes of  $\text{CH}_3$  and  $\text{CH}_2+\text{CH}$  components satisfy

$$2(16V_{\text{CH}_2+\text{CH}} + V_{\text{CH}_3}) = V_{\text{L}} - V_{\text{HL}}. \quad (3.25)$$

These component volumes constrain the height of the Gaussians as

$$c_{\text{PC}} = \frac{V_{\text{PC}}}{A_{\text{L}}\sigma_{\text{PC}}} \quad (3.26)$$

$$c_{\text{CG}} = \frac{V_{\text{CG}}}{A_{\text{L}}\sigma_{\text{CG}}} \quad (3.27)$$

$$c_{\text{CH}_3} = \frac{2V_{\text{CH}_3}}{A_{\text{L}}\sigma_{\text{CH}_3}} \quad (3.28)$$

$$c_{\text{Tat}} = \frac{V_{\text{Tat}}}{A_{\text{L}}\sigma_{\text{Tat}}} \quad (3.29)$$

where  $A_{\text{L}}$  is area per lipid.

The ratio of the carbonyl/glycerol volume to the headgroup volume  $V_{\text{HL}}$  was reported to be 0.41 [43], so we constrain the CG component volume to  $135.7 \text{ \AA}^3$  and the PC component volume to  $195.3 \text{ \AA}^3$ .

The most detailed structural study on DOPC to date was published by Braun *et al.* [43], and many of constraints on our model parameters can be derived from their study. However, in that work, the authors used the SDP model [41], which is specifically tailored for combined analysis of neutron and X-ray form factors. Therefore, we need to convert their structural results to the corresponding parameters in our simpler model. For example, from the reported values of the ratio of the volumes of the chain terminal methyl ( $\text{CH}_3$ ) to the chain methylenes ( $\text{CH}_2$ ) and the ratio of the volumes of the chain methines ( $\text{CH}$ ) to the chain methylenes, we can calculate the ratio  $r_{\text{CH}_3}$  of the volumes of  $\text{CH}_3$  to the  $\text{CH}_2$  and  $\text{CH}$  combined component. Furthermore, the study by Braun *et al.* was at  $30^\circ\text{C}$  while our study was at  $37^\circ\text{C}$ , so our measured volume of DOPC was slightly higher.

At  $30^\circ\text{C}$ , the volume of DOPC was reported to be  $1303 \text{ \AA}^3$ , so the volume of hydrocarbon chain region at the same temperature is  $1303 - 331 = 972 \text{ \AA}^3$ . The ratio  $r$  of the volumes of the chain terminal methyl ( $\text{CH}_3$ ) to the chain methylenes ( $\text{CH}_2$ ) was reported to be 1.95, and the ratio  $r_{12}$  of the volumes of the chain methines ( $\text{CH}$ ) to the chain methylenes 0.91 at  $30^\circ\text{C}$ . Because there are 14  $\text{CH}_2$  groups, 2  $\text{CH}$  groups, and 1  $\text{CH}_3$  group in each DOPC hydrocarbon chain, we have  $2 \times (14V_{\text{CH}_2} + 2V_{\text{CH}} +$

$V_{\text{CH}_3}) = 972 \text{ \AA}^3$ . Using  $r = V_{\text{CH}_3}/V_{\text{CH}_2} = 1.95$  and  $r_{12} = V_{\text{CH}}/V_{\text{CH}_2} = 0.91$ , we get  $V_{\text{CH}_2} = 27.3 \text{ \AA}^3$ ,  $V_{\text{CH}} = 24.9 \text{ \AA}^3$ , and  $V_{\text{CH}_3} = 53.3 \text{ \AA}^3$ . These calculated volumes lead to  $V_{\text{CH}_3}/V_{\text{CH}_2+\text{CH}} = 1.97$  for 30 °C.

At 37 °C, the volume of DOPC was measured to be  $1313.5 \text{ \AA}^3$ , so we have  $2 \times (16V_{\text{CH}_2+\text{CH}} + V_{\text{CH}_3}) = 1313.5 - 331$ . Assuming that the ratio  $V_{\text{CH}_3}/V_{\text{CH}_2+\text{CH}}$  at 37 °C is the same as that at 30 °C gives  $V_{\text{CH}_2+\text{CH}} = 27.3 \text{ \AA}^3$  and  $V_{\text{CH}_3} = 53.9 \text{ \AA}^3$ . We constrain the components for the hydrocarbon chain region in our model to these calculated values.

lipid	number of electrons	volume ( $\text{\AA}^3$ )
DOPC	434	1313.5
DOPE	410	1212.3
DOPC:DOPE (3:1)	428	1288.2

Table 3.2: Number of electrons per lipid and volume per lipid.

component	$n_i^e$	$V_i$ ( $\text{\AA}^3$ )	$\rho_i$ ( $\text{e}/\text{\AA}^3$ )
PC	97	195.3	0.497
PE	73	94.1	0.776
PC:PE (3:1)	91	170	0.535
CG	67	135.7	0.494
$\text{CH}_2+\text{CH}$	7.875	27.3	0.288
$\text{CH}_3$	9	53.9	0.167

Table 3.3: Some structural parameters for each component.  $n_i^e$  is the number of electrons and  $\rho_i$  is the average electron density.

number of electrons	838	mole fraction ( $x_{\text{Tat}}$ )	$n_{\text{Tat}}^e$	$V_{\text{Tat}}$ ( $\text{\AA}^3$ )
volume ( $\text{\AA}^3$ )	1877	0.016	13.6	30.5
$\rho_{\text{Tat}}$ ( $\text{e}/\text{\AA}^3$ )	0.446	0.034	29.5	66.1
		0.059	53.0	118.8

Table 3.4: Tat basic structural parameters. The notations are the same as in Table 3.3.  $x_{\text{Tat}} = \text{Tat}/(\text{Tat}+\text{Lipid})$ .

## Fits with Lower Bounds

Non-linear least squared fits with upper and lower bounds for the model parameters are implemented using an internal-external parameter transformation method. This



method is described in MINUIT User’s Guide, section 1.3 [44]. This section briefly describes the method. The details can be found in the MINUIT website [45].

Basically, instead of a model parameter, which is also called the external variable, the minimization procedure varies a related variable called the internal variable. This internal variable can take any values between  $-\infty$  to  $+\infty$ . At every  $\chi^2$  calculation, the internal variable is transformed to the external variable, which can take values only between the lower and upper bounds ( $a$  and  $b$ ). This non-linear transformation allows an existing minimization algorithm that was developed for fits with no bounds to work for fits with bounds. This point was important because it allowed us to implement bound fits in the model fitting program called the SDP program, fully developed by Dr. Norbert Kucerka, without too many additional changes. Downsides of the transformation method include turning a linear problem into a non-linear one and some computational overhead, neither of which is particularly problematic in this study.

For variables with both lower and upper bounds ( $a$  and  $b$ , respectively), the transformation between the internal and external variables is

$$P_{\text{int}} = \arcsin\left(2\frac{P_{\text{ext}} - a}{b - a} - 1\right) \quad (3.30)$$

$$P_{\text{ext}} = a + \frac{b - a}{2}(\sin P_{\text{int}} + 1). \quad (3.31)$$

For variables with a lower bound  $a$  only, the transformation is

$$P_{\text{int}} = \sqrt{(P_{\text{ext}} - a + 1)^2 - 1} \quad (3.32)$$

$$P_{\text{ext}} = a - 1 + \sqrt{P_{\text{int}}^2 + 1}, \quad (3.33)$$

and for variables with an upper bound  $b$  only,

$$P_{\text{int}} = \sqrt{(b - P_{\text{ext}} + 1)^2 - 1} \quad (3.34)$$

$$P_{\text{ext}} = b + 1 - \sqrt{P_{\text{int}}^2 + 1}. \quad (3.35)$$

### 3.2.4 Molecular Dynamics Simulation

This section describes the MD simulations performed by Dr. Kun Huang, who was a graduate student of Prof. Angel Garcia at Rensselaer Polytechnic Institute.

Systems with different DOPC/Tat mole ratios (128:0, 128:2 and 128:4, corresponding to 0, 0.015 and 0.030 mole fractions) were simulated atomistically using the Gromacs 4.6.1 package [46]. DOPC was modeled by the Slipid force field [47,48] and HIV Tat was modeled by Amber 99SB [49]. Tip3p water was used [50]. The number of Tats was divided equally on each side of the bilayer to mimic experimental conditions. All systems were simulated at 310 K with a constant area in the  $x$ - $y$  plane and 1 atm constant pressure in the  $z$  direction. Each system was simulated for 100 ns and the last 50 ns was used as the production run. At each DOPC/Tat mole ratio, we studied systems with three different area/lipid ( $A_L$ ). For the DOPC system, we fixed  $A_L = 68, 70, 72 \text{ \AA}^2$ ; DOPC/Tat (128:2), we fixed the  $A_L = 72, 74, 76 \text{ \AA}^2$ ; DOPC/Tat (128:4), we fixed the  $A_L = 72, 74, 76 \text{ \AA}^2$ . These values were based on the analysis of experimentally obtained form factors, which is discussed in Sec. 3.4.3. For each DOPC/Tat system at fixed  $A_L$ , we then conducted seven independent simulations with the center of mass (COM) of each Tat constrained at different bilayer depths from the bilayer center (18, 16, 14, 12, 10, 8 and 5  $\text{\AA}$ ). In total, 45 independent simulations were conducted. The goal of constrained simulations is to find the best match between experimental and MD simulation form factors. Comparison to the X-ray form factors was performed using the SIMtoEXP software written by Dr. Norbert Kucerka [51].

All simulations were conducted with a 2 fs time integration step. SETTLE [52] was used to constrain water molecules and LINCS [53] was used to constrain all other bond lengths in the system. VdW interactions were truncated at 1.4 nm with a twin-range cutoff scheme and a dispersion correction was applied to both energy and pressure. Electrostatics interactions were treated with the particle-mesh Ewald (PME) method [54]. The direct term for electrostatics was evaluated within 1.0 nm cutoff and the Fourier term was evaluated with a 0.12 nm grid spacing and a 4th order interpolation. Each system was simulated at 310 K using the V-rescale algorithm [55] with a 0.2 ps time coupling constant. The semi-isotropic parrinello-rahman barostat [56] was used to couple the system at 1 atm in the  $z$  direction with a 5 ps time coupling constant, while the projected area at the  $x$ - $y$  plane was fixed by setting the system compressibility to 0. We inserted the Tats into the system by initially turning off all interactions between Tats and the rest of the system, with Tats constrained at different depths. Then we slowly turned on the interactions to normal strength through thermodynamics integrations. We used umbrella potentials

to constrain Tats at desired depths with a force constant of 3000 kJ/mol/nm<sup>2</sup>.

The center of mass (COM) distance between each peptide and the bilayer was constrained by an umbrella potential with a force constant  $k$  of 3000 kJ/mol/nm<sup>2</sup>. Essentially, this potential acts as a spring, where its potential energy depends on the deviation of the distance between the center of mass of Tat and DOPC from a preferred value,  $z_0$ ,

$$U(z_1^{\text{Tat}}, \dots, z_1^{\text{DOPC}}, \dots) = -\frac{1}{2}k(z_{\text{cm}}^{\text{Tat}} - z_{\text{cm}}^{\text{DOPC}} - z_0)^2.$$

Then,  $-\partial U/\partial z_i$  is the external force acting on atom,  $i$ .

## 3.3 Analysis of Molecular Dynamics Simulation Data

### 3.3.1 SIMtoEXP program

This section briefly describes the SIMtoEXP program developed by Dr. Norbert Kucerka [51]. Essentially, for each snapshot, positional distribution of each atom averaged over the  $xy$  plane is calculated. Then, the distribution is averaged over snapshots. The product of this distribution and the average electron density gives the electron density profile of the atom. The sum over all the atoms provide the total electron density profile. This total electron density profile minus the average electron density of water is Fourier transformed to provide the X-ray form factor.

$$F^{\text{sim}}(q_z) = \int_0^\infty dz(\rho(z) - \rho_W) \cos(q_z z). \quad (3.36)$$

Electron density profiles were symmetrized and then X-ray form factors were calculated with  $\rho_W = 0.326 \text{ e}/\text{\AA}^3$ , which was the average electron density of water molecules in the MD simulations. Because  $\rho(z)$  is equal to  $\rho_W$  outside the bilayer, the upper integration limit takes on a finite value.

Because the experimental form factor is on arbitrary units, it is scaled by a single constant  $a$  to produce the best fit to the simulated form factor through a linear least squared fit that minimizes the following goodness of fit

$$\chi^2 = \sum_i \left( \frac{1}{\sigma_i} (a|F_i^{\text{exp}}| - |F^{\text{sim}}(q_{z,i})|) \right)^2 \quad (3.37)$$

where  $\sigma_i$  is the input experimental uncertainties and  $F_i^{\text{exp}}$  is the experimental form factor measured at  $q_z = q_{z,i}$ . The SIMtoEXP program does not scale the input uncertainties, so the relative errors ( $\sigma_i/|F_i^{\text{exp}}|$ ) depend on the value of the overall scaling factor  $a$ . Consequently, the  $\chi^2$  values calculated by the program had to be multiplied by  $1/a^2$ . These corrected  $\chi^2$  are reported in this chapter.

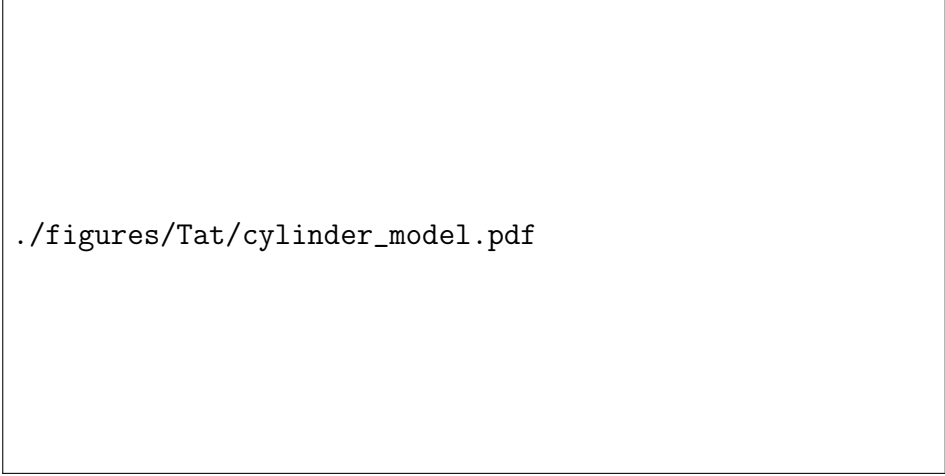
### 3.3.2 Local Thinning of Membranes

My contribution to the MD simulations was to help analyze the results.

The SIMtoEXP program only gives the average quantities for each leaflet. While our X-ray data are sensitive to the bilayer average electron density, local information

of Tat-bilayer interactions can be obtained from MD simulations. In this section, we discuss a method to extract a local membrane thickness around the Tat peptides from the MD simulation trajectories.

One of the expected effects of Tat interacting with a bilayer is compression of the lipid bilayer along the  $z$ -direction. It is reasonable to assume that this compression is greater near Tat and weaker far from Tat. If this is the case, the distance between phosphorus atoms in opposite leaflets near Tat should be different from the distance between phosphorus atoms away from Tat. For a small Tat concentration,  $D_{\text{phos-phos}}$  is the same as that of pure DOPC if the distance from all Tats is large enough. For our experimental concentrations, the thinning effect may extend throughout the bilayer because the lateral effect of Tat might have a larger lateral decay length than the distance between Tats. Whether that is the case or not, we expect that the thickness near the Tats is smaller than the average thickness, so  $D'_{\text{phos-phos}}$  is what we want to measure.



./figures/Tat/cylinder\_model.pdf

Figure 3.6: Our simple model to extract the local bilayer thickness from simulation trajectories. Tat is modeled as a cylinder with its height  $H_{\text{Tat}}$  and radius  $R_{\text{Tat}}$ . The local thickness is defined as  $D'_{\text{phos-phos}}$ . The thickness of the unperturbed DOPC bilayer is  $D_{\text{phos-phos}}$ . Blue highlighted lipids fall within the imaginary cylinder extended from the Tat. Unperturbed lipids are highlighted in green.

First, let us define what we mean by lipids close to Tat. As in Fig. 3.6, we imagine a cylinder around Tat and find all the phosphorus atoms within it. Approximating Tat as a cylinder with its height given by the FWHM of its electron density distribution, its radius  $R_{\text{Tat}} = 9 \text{ \AA}$  comes from the experimentally determined volume  $V_{\text{Tat}} = 1876$

$\text{\AA}^3$  and  $H_{\text{Tat}} = 7.6 \text{ \AA}$  measured from one of the simulations (see Sec. 3.4.6). Let us define the lateral center of the cylinder as the center of mass of each Tat. Then we define  $D'_{\text{phos-phos}}$  using only those lipids whose phosphorus atoms lie within these  $9 \text{ \AA}$  cylinders around the Tats. Then  $D_{\text{phos-phos}} = z_{\text{phos}}^+ - z_{\text{phos}}^-$  where  $z_{\text{phos}}^+$  and  $z_{\text{phos}}^-$  are the average  $z$  of the  $n_1$  ( $n_2$ ) lipids in the upper and lower monolayer, respectively.

The algorithm for doing the above was straightforward. For each time frame, the positions  $(x_i, y_i, z_i)$  of each Tat,  $i$ , are listed. We chose phosphorus atoms whose  $(x, y)$  lateral position lied within  $9 \text{ \AA}$  of any one of the Tat's lateral position. Then,  $z$  positions of the chosen phosphorus atoms were placed in a list. Then,  $z_{\text{phos}}$  were calculated from the list. We averaged over many snapshots to gain better statistics.

### 3.3.3 Lateral Decay Length of Membrane Thinning

This section describes a method to measure the lateral decay length of membrane thinning due to Tat-lipid interactions. As in the previous section, Tat is modeled here as a cylinder with its radius equal to  $R_1$ , height  $H_{\text{Tat}}$ , and volume  $V_{\text{Tat}}$  such that  $R_1 = \sqrt{V_{\text{Tat}}/(\pi H_{\text{Tat}})}$ . Let  $h(r)$  represent the phosphorus height profile of a leaflet as in Fig. 3.7. The two leaflets are assumed to be decoupled. In our model, lipids are separated into three regions: suppressed, boundary, and unperturbed region. The suppressed region extends from  $r = 0$  to  $R_1$  and is directly beneath (above) Tat in the top (bottom) leaflet. In this region, lipids are uniformly compressed by Tat toward the center of the bilayer, so that  $h(r)$  is a constant equal to  $z_{\text{phos}}$ . From  $r = R_1$  to  $R_2$  is the boundary region, where  $h(r)$  is assumed to linearly increase with the lateral distance  $r$ . The lateral decay length of membrane thinning is given by  $R_2 - R_1$ . In the unperturbed region ( $r > R_3$ ), lipids do not interact with Tat, behaving identically to DOPC, so the phosphorus position is the same as that of DOPC. A continuous  $h(r)$  that satisfies the above criteria is

$$h(r) = \begin{cases} z_{\text{phos}} & \text{if } 0 \leq r < R_1 \\ mr + b & \text{if } R_1 \leq r < R_2 \\ z_{\text{phos}}^0 & \text{if } R_2 \leq r < R_3 \end{cases} \quad (3.38)$$

with  $m = (z_{\text{phos}} - z_{\text{phos}}^0)/(R_1 - R_2)$  and  $b = (z_{\text{phos}}^0 R_1 - z_{\text{phos}} R_2)/(R_1 - R_2)$ . Approximating the simulation box as a cylinder gives  $R_3 = \sqrt{N A_L / \pi}$ , where  $N$  is the number of lipids in a leaflet.  $z_{\text{phos}}$  can be measured directly from simulation trajectories.  $z_{\text{phos}}^0$

is a half of the average phosphorus-phosphorus distance in a DOPC simulation, which can be easily obtained from the SIMtoEXP program. The average height profile over the monolayer,  $\langle h(r) \rangle$ , can be also obtained from the program in the same manner. The only unknown is  $R_2$ .

./figures/Tat/linear\_model.png

Figure 3.7: Simple model of the lateral decay of the membrane thickness perturbation due to Tat.

Let us calculate  $\langle h(r) \rangle$ . In cylindrical coordinates,

$$\langle h(r) \rangle = \frac{1}{\pi R_3^2} \int_0^{2\pi} d\phi \int_0^{R_3} dr r h(r) \quad (3.39)$$

The  $\phi$  integration is trivial. The  $r$  integration is

$$\begin{aligned} & \int_0^{R_3} dr r h(r) \\ &= \int_0^{R_1} dr z_{\text{phos}} r + \int_{R_1}^{R_2} dr (mr + b)r + \int_{R_2}^{R_3} dr z_{\text{phos}}^0 r \\ &= \frac{1}{2} [z_{\text{phos}} R_1^2 + z_{\text{phos}}^0 (R_3^2 - R_2^2)] + \frac{1}{3} m (R_2^3 - R_1^3) + \frac{1}{2} b (R_2^2 - R_1^2) \\ &= \frac{1}{2} [z_{\text{phos}} R_1^2 + z_{\text{phos}}^0 (R_3^2 - R_2^2)] + \frac{1}{3} (z_{\text{phos}}^0 - z_{\text{phos}}) (R_2^2 + R_1 R_2 + R_1^2) \\ &\quad + \frac{1}{2} (z_{\text{phos}} R_2 - z_{\text{phos}}^0 R_1) (R_1 + R_2) \end{aligned} \quad (3.40)$$

Using Eq. (3.40), we get

$$\langle h(r) \rangle = \frac{(z_{\text{phos}} - z_{\text{phos}}^0)(R_1^2 + R_1 R_2 + R_2^2) + 3z_{\text{phos}}^0 R_3^2}{3R_3^2} \quad (3.41)$$

Eq. 3.41 is a quadratic equation in terms of  $R_2$ . Solving for  $R_2$  gives

$$R_2 = \frac{-R_1 + \sqrt{R_1^2 + 4C}}{2} \quad (3.42)$$

with

$$C = \frac{3R_3^2(z_{\text{phos}}^0 - \langle h(r) \rangle)}{z_{\text{phos}}^0 - z_{\text{phos}}} - R_1^2 \quad (3.43)$$

## 3.4 Results


### 3.4.1 Bending and Bulk Modulus

(Under construction) Show X-ray data. Show fitting boxes. Show the  $K_c$  values. Also, show the resultant form factors, which qualitatively show the membrane thinning. Also describe how I got error bars.

Fig. 3.1 shows the scattering intensity pattern from DOPC/DOPE (1:1) with mole fraction  $x_{\text{Tat}} = 0.034$ . The diffuse lobes are due to equilibrium fluctuations that occur in these fully hydrated, oriented lipid/peptide samples. The intensity  $I(\mathbf{q})$  in the diffuse patterns provide the absolute values of the form factors  $F(q_z)$ , which are the Fourier transforms of the electron density profile, through the relation  $I(\mathbf{q}) = S(\mathbf{q})|F(q_z)|^2/q_z$ , where  $\mathbf{q} = (q_r, q_z)$ ,  $S(q)$  is the structure interference factor, and  $q_z^1$  is the usual LAXS approximation to the Lorentz factor [57–59]. The first step in the analysis takes advantage of the  $q_r$  dependence of the scattering to obtain the bending modulus  $K_c$  with results shown in Fig. 3.8. As positively charged Tat concentration was increased, the lamellar repeat spacing  $D$  generally increased in neutral lipid bilayers and decreased in negatively charged bilayers, consistent with changes in electrostatic repulsive interactions. With few exceptions, the water space between bilayers exceeded 20 Å.

The analysis that obtains  $K_c$  also obtains the structure factor  $S(\mathbf{q})$  and then the unsigned form factors  $|F(q_z)|$  are obtained from the intensity  $I(\mathbf{q})$  by division. Results for five different membrane mimics are shown in Fig. 3.9. Vertical lines indicate the





figures/Tat/figure2.pdf

Figure 3.8: Bilayer bending modulus,  $K_c$ , vs. Tat mole fraction  $x_{\text{Tat}}$ .  $D$ -spacings for DOPC/Tat mixtures varied from 64 to 68 Å, for DOPC/DOPE/Tat mixtures from 64 to 69 Å, for DOPC/DOPS/Tat (3:1) mixtures from 57 Å to 100 Å (pure DOPS was unbound), and for nuclear mimic/Tat mixtures from unbound (nuclear mimic) to 64 Å. Estimated uncertainty in all values is about  $\pm 2$ .

zero position between the lobes of diffuse data where  $F(q_z)$  change sign. In every sample, the zero positions shift to larger  $q_z$ , indicating a thinning of the membranes.



Figure 3.9: Form factors of lipid mixtures (arbitrarily scaled and vertically displaced) with increasing Tat mole fractions  $x_{\text{Tat}}$  indicated on figure legends. Lipid mixtures: A. DOPC B. DOPC/DOPE (3:1) C. DOPC/DOPE (1:1) D. DOPC/DOPS (3:1) E. Nuclear mimic. The entire  $q_z$  range is shown in C, while others show partial ranges. Solid vertical lines indicate the  $q_z$  values where the form factors equal zero between the lobes of diffuse data.

### 3.4.2 Volume results

Experimental and simulated volumes are given in Table 3.5. The simulated volume was obtained using the volume app in the SIMtoEXP program. The experimental Tat volume was calculated from the measured density assuming that the lipid volume was

the same as with no Tat. In general, there may be an interaction volume between the peptide and the lipid membrane as previously reported for bacteriorhodopsin [60]. As lipid was present in excess to Tat, the partial molecular volume of the lipid should be the same as with no Tat, so this way of calculating includes all the interaction volume in  $V_{\text{Tat}}$ . Comparison of  $V_{\text{Tat}}$  in water with the result for 5:1 Lipid:Tat suggests that the interaction volume may be negative, consistent with a net attractive interaction with lipid. Understandably, values of  $V_{\text{Tat}}$  were unreliable for small mole ratios of Tat:Lipid. Therefore we used simple additivity for those mimics not shown in Table 3.5 for the volumes used in the electron density profile modeling. All volumes obtained from the Gromacs MD simulations were somewhat smaller than the measured volumes, but it supports the Tat volume being closer to  $1877 \text{ \AA}^3$  than the outlying values obtained experimentally at small Tat concentrations. The measured volume was in a good agreement with the value calculated from a peptide calculator website [61], which gave  $1888 \text{ \AA}^3$ .

Experiments			
Tat in:	$V_{\text{lipid}} (\text{\AA}^3)$	Lipid:Tat	$V_{\text{Tat}} (\text{\AA}^3)$
water		1877	
DOPC:DOPE (3:1)	1288	5:1	1822
DOPC	1314	39.6:1	676
DOPC:DOPS (3:1)	1298	39.6:1	2613

Simulations			
Tat in:	$V_{\text{lipid}} (\text{\AA}^3)$	Lipid:Tat	$V_{\text{Tat}} (\text{\AA}^3)$
DOPC	1283	128:2	1694
DOPC	1294	128.4	1699

Table 3.5: Volume results at 37 °C

### 3.4.3 Electron Density Profile Modeling

(Under construction) Using the model described in section 3.2.3, we fitted our measured X-ray form factors. In all fits, the positions of component groups were free parameters, but we assumed that the lipid headgroup is somewhat rigid so that it cannot compress or expand. This assumption led to fixing the distance  $z_{\text{PC}} - z_{\text{CG}}$  between the PC and CG components as well as the distance  $z_{\text{CG}} - z_{\text{HC}}$  between the CG component and the Gibbs dividing surface for the hydrocarbon chains. We

also constrained the width of Tat Gaussian. We fitted with three different values of widths, 2.5, 3.0, and 3.5, to study the range of variation due to the Tat width. The choice was made based on MD simulation results. (Check this again) We constrained the Tat width because we found that this parameter tended to become very small when it was free. This tendency to a unphysically small value was due to lack of higher  $q_z$  data points. A very narrow feature in an electron density profile led to large magnitude of the form factor at larger  $q_z$ . Because data points at larger  $q_z$  were not available, this narrow feature did not get penalized. In wide angle X-ray scattering, which probes much larger  $q_z$  than LAXS does, we did not observe much diffuse scattering for  $q_z > 1.0 \text{ \AA}^{-1}$  (data not shown). Also, from a stereochemical point of view, a peptide width cannot be too small. These arguments allowed us to disregard the best fits with a too small value of  $\sigma_{\text{Tat}}$  and led to fixing the Tat width.

Figure 3.10 shows the results for DOPC with Tat. As shown, the fits were generally very good. Table 3.6 shows the best fit parameters for DOPC bilayers. It is clear that the area per lipid  $A_L$  increased as the Tat concentration was increased. An increase in  $A_L$  implies thinning of the bilayer which is an incompressible membrane. The results for DOPC:DOPE (3:1) are shown in Fig. 3.11 and Table 3.7, and the results for DOPC:DOPE (1:1) in Fig. 3.12 and Table 3.8. Figure 3.13 summarizes these results. For the results shown in Fig. 3.13, a consistent trend is that Tat moved away from the bilayer center as concentration increased.

$x_{\text{Tat}}$	0	0.016	0.016	0.016	0.034	0.034	0.034	0.059	0.059	0.059
$\chi^2$	2961	1554	1570	1581	1563	1587	1607	2342	2338	2363
$z_{\text{PC}}$	18.1	18.0	17.9	17.9	17.8	17.7	17.6	17.8	17.8	17.7
$\sigma_{\text{PC}}$	2.52	2.14	2.17	2.18	1.86	1.92	1.93	2.02	1.97	1.93
$z_{\text{CG}}$	15.0	14.9	14.8	14.8	14.7	14.6	14.5	14.7	14.7	14.6
$\sigma_{\text{CG}}$	3.00	2.62	2.64	2.66	2.22	2.30	2.31	2.58	2.27	2.14
$z_{\text{HC}}$	13.7	13.6	13.5	13.5	13.4	13.3	13.2	13.4	13.4	13.3
$\sigma_{\text{HC}}$	3.00	2.69	2.84	2.95	2.65	2.82	3.01	2.47	2.58	2.83
$\sigma_{\text{CH}_3}$	3.20	3.19	3.22	3.24	3.37	3.43	3.47	2.70	2.70	2.74
$z_{\text{Tat}}$	NA	12.9	13.4	14.2	13.1	13.8	14.4	15.2	15.2	15.7
$\sigma_{\text{Tat}}$	NA	2.5	3.0	3.5	2.5	3.0	3.5	2.5	3.0	3.5
$A_L$	71.5	72.4	72.5	72.7	73.6	74.0	74.4	73.6	73.5	73.9

Table 3.6: Fitting Results for DOPC membranes for the THG (Tat in headgroup) model.  $z_{\text{PC}} - z_{\text{CG}} = 3.1 \text{ \AA}$  and  $z_{\text{CG}} - z_{\text{HC}} = 1.3 \text{ \AA}$  in all fits.

As shown in Fig. 3.10, the membrane thickness can be defined as the distance  $D_{\text{PP}}$



Figure 3.10: The best fits to DOPC form factors (left) and the corresponding electron density profiles (right) with  $x_{\text{Tat}} = 0, 0.016, 0.034,$  and  $0.059$  (from top to bottom).



Figure 3.11: The best fits to DOPC:DOPE (3:1) form factors (left) and the corresponding electron density profiles (right) with  $x_{\text{Tat}} = 0, 0.016, 0.034$ , and  $0.059$  (from top to bottom).

$x_{\text{Tat}}$	0	0.016	0.016	0.016	0.034	0.034	0.034	0.059	0.059	0.059
$\chi^2$	924.5	4972	4985	4994	6758	6826	6863	2293	2280	2296
$z_{\text{PC}}$	18.3	18.5	18.5	18.4	18.5	18.4	18.3	18.2	18.2	18.1
$\sigma_{\text{PC}}$	2.66	2.23	2.26	2.27	2.25	2.31	2.34	2.31	2.19	2.11
$z_{\text{CG}}$	15.2	15.4	15.4	15.3	15.4	15.3	15.2	15.1	15.1	15.0
$\sigma_{\text{CG}}$	2.92	2.63	2.65	2.69	2.52	2.58	2.63	2.40	2.20	2.01
$z_{\text{HC}}$	13.9	14.1	14.1	14.0	14.1	14.0	13.9	13.8	13.8	13.7
$\sigma_{\text{HC}}$	2.73	2.70	2.83	2.91	2.86	2.79	2.84	2.25	2.38	2.60
$\sigma_{\text{CH}_3}$	3.24	2.94	2.97	2.98	2.87	2.90	2.91	2.63	2.61	2.65
$z_{\text{Tat}}$	NA	13.5	14.0	15.0	14.3	14.9	16.0	16.3	16.4	16.9
$\sigma_{\text{Tat}}$	NA	2.5	3.0	3.5	2.5	3.0	3.5	2.5	3.0	3.5
$A_{\text{L}}$	70.9	69.8	69.9	70.1	69.5	70.0	70.6	71.3	71.4	71.7

Table 3.7: Fitting Results for DOPC:DOPE (3:1) membranes for the THG model.  $z_{\text{PC}} - z_{\text{CG}} = 3.1 \text{ \AA}$  and  $z_{\text{CG}} - z_{\text{HC}} = 1.3 \text{ \AA}$  in all fits.

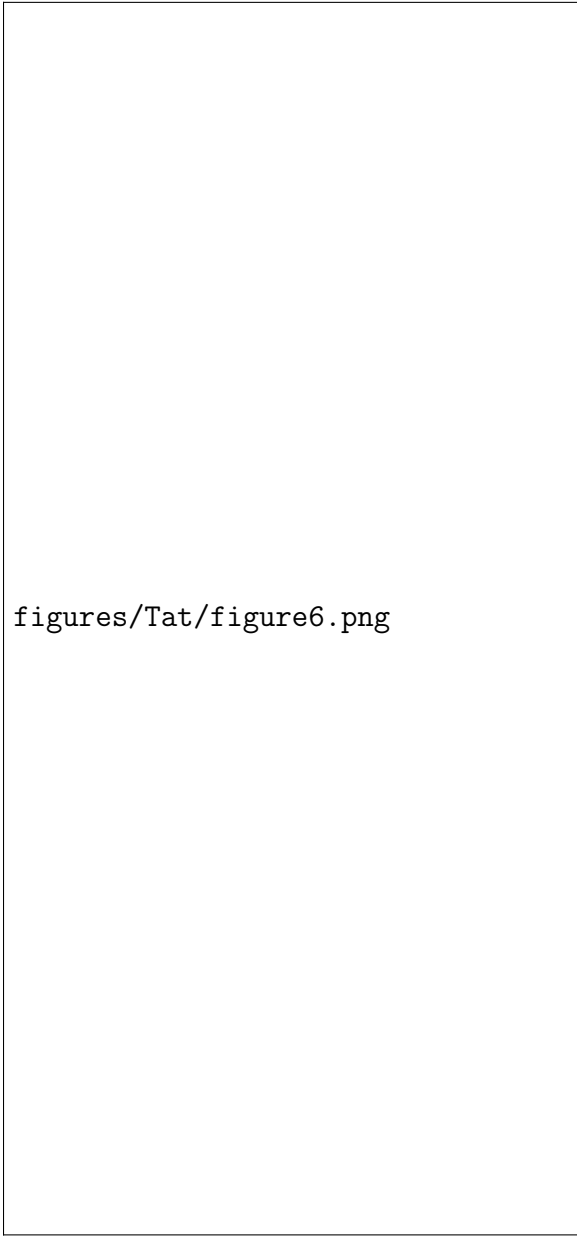
$x_{\text{Tat}}$	0	0.016	0.016	0.016	0.034	0.034	0.034	0.059	0.059	0.059
$\chi^2$	2961	1554	1570	1581	1563	1587	1607	2342	2338	2363
$z_{\text{PC}}$	18.1	18.0	17.9	17.9	17.8	17.7	17.6	17.8	17.8	17.7
$\sigma_{\text{PC}}$	2.52	2.14	2.17	2.18	1.86	1.92	1.93	2.02	1.97	1.93
$z_{\text{CG}}$	15.0	14.9	14.8	14.8	14.7	14.6	14.5	14.7	14.7	14.6
$\sigma_{\text{CG}}$	3.00	2.62	2.64	2.66	2.22	2.30	2.31	2.58	2.27	2.14
$z_{\text{HC}}$	13.7	13.6	13.5	13.5	13.4	13.3	13.2	13.4	13.4	13.3
$\sigma_{\text{HC}}$	3.00	2.69	2.84	2.95	2.65	2.82	3.01	2.47	2.58	2.83
$\sigma_{\text{CH}_3}$	3.20	3.19	3.22	3.24	3.37	3.43	3.47	2.70	2.70	2.74
$z_{\text{Tat}}$	NA	12.9	13.4	14.2	13.1	13.8	14.4	15.2	15.2	15.7
$\sigma_{\text{Tat}}$	NA	2.5	3.0	3.5	2.5	3.0	3.5	2.5	3.0	3.5
$A_{\text{L}}$	71.5	72.4	72.5	72.7	73.6	74.0	74.4	73.6	73.5	73.9

Table 3.8: (Numbers are wrong) Fitting Results for DOPC:DOPE (1:1) membranes for the THG model.  $\Delta z_1 = z_{\text{PC}} - z_{\text{CG}}$  and  $\Delta z_2 = z_{\text{CG}} - z_{\text{HC}}$ .



Figure 3.12: The best fits to DOPC:DOPE (1:1) form factors (left) and the corresponding electron density profiles (right) with  $x_{\text{Tat}} = 0, 0.016, 0.034$ , and  $0.059$  (from top to bottom).






figures/Tat/figure6.png

Figure 3.13: Modeling results for absolute electron density profiles and for the Tat location as a function of distance  $z$  along the bilayer normal. A. DOPC B. DOPC:DOPE (3:1), and C. DOPC:DOPE (1:1).

between the PC components in the opposing leaflets or the distance  $D_{\text{HH}}$  between the maxima in the opposing leaflets.  $D_{\text{HH}}$  is more reliable than  $D_{\text{PP}}$  because it is a property of the total electron density of a bilayer and, therefore, does not depend strongly on the specific model employed for fitting the data. Indeed, the total electron density profile can be determined independently of a bilayer model by writing the electron density profile in terms of Fourier series, Fourier transforming the profile, and fitting the resulting model-independent form factor to the data. On the other hand,  $D_{\text{PP}}$  is a property that depends on lipid components, which are influenced by how the lipid is parsed and what assumptions and constraints go into the specific model. A disadvantage of using  $D_{\text{HH}}$  as a measure of the membrane thickness is that  $D_{\text{HH}}$  is influenced by the electron density of Tat because the total electron density profile includes a contribution from the electron density of Tat. Especially when the mole fraction of Tat in a system becomes large, the Tat electron density contributes significantly to the total electron density profile. If the Tat resided slightly outside of the PC component, the apparent membrane thickness measured by  $D_{\text{HH}}$  would be larger than  $D_{\text{PP}}$ . Then, even if the actual bilayer thickness defined by  $D_{\text{PP}}$  were reduced by the presence of Tat, the effect of thinning might not be obvious. With the above caveat in mind, we report both quantities in what follows since they can be easily calculated from the model.

More structural detail from the modeling is shown in Fig. 3.14. Figs. 3.14A and 3.14B show that both  $D_{\text{PP}}$  and  $D_{\text{HH}}$  tended to decrease with increasing Tat mole fraction  $x_{\text{Tat}}$ , showing that Tat thins membranes, increasingly so as its concentration is increased, even though both simulation and modeling suggested that Tat moves further from the membrane center with increasing concentration as shown in Fig. 3.14D. Figure 3.14C shows that the area per lipid  $A_{\text{L}}$  usually increased with increasing mole fraction of Tat, similar to the findings from MD simulations (Sec. 3.4.6), as would be expected.

We also investigated how the goodness of fits varied as the position of the Tat Gaussian was varied. Figure 3.15 plots  $\chi^2$  as a function of the fixed Tat position  $z_{\text{Tat}}$ . We found that the two models, THG (Tat in headgroup region) and THC (Tat in hydrocarbon chain region), resulted in similar electron density profiles, yielding similar  $\chi^2$  values when Tat was placed near the hydrocarbon-water interface region. In the THC model, the error function representing the hydrocarbon chain region became wider as Tat was placed near the interface region but further from the bilayer center.



figures/Tat/figure7.pdf

Figure 3.14: A. Bilayer thickness,  $D_{PP}$ ; B. Bilayer thickness,  $D_{HH}$ ; C. Area/lipid,  $A_L$ ; D. Twice the Tat location,  $2z_{Tat}$ : all plotted vs. Tat mole fraction  $x_{Tat}$ . Error bars are standard deviations from imposing Tat Gaussian widths,  $\sigma_{Tat} = 2.5, 3.0$  or  $3.5 \text{ \AA}$ . Inverted blue triangles connected with dotted line are results from MD simulations, averaging the best fits to the X-ray data for each parameter, with standard deviations shown.

The subtraction of the Tat component from the hydrocarbon chain error function resulted in a smooth error function-like profile with an apparent smaller value of  $\sigma$  such that the total profile calculated from the THC model was very similar to that calculated from the THG model.



Figure 3.15:  $\chi^2$  as a function of  $z_{\text{Tat}}$  for DOPC, DOPC:DOPE (3:1), and DOPC:DOPE (1:1) (from left to right) with  $x_{\text{Tat}} = 0.016, 0.034,$  and  $0.059$  (from top to bottom).  $\sigma_{\text{Tat}} = 3.0$ . The THG model (black squares) and the THC model (red circles).

In general, while the total electron density profile is well determined by our modeling procedures, the values of the parameters for the components are not as well determined as the agreement of the fit to the data may suggest. In many cases, we found multiple local minima in the fitting landscape, including one with Tat closer to the center of the bilayer as shown in Fig. 3.15.  $\chi^2$  calculated at these local minima tended to be smaller for larger concentration of Tat. We also found that  $\chi^2$  with  $z_{\text{Tat}}$  in the hydrocarbon chain region and headgroup region was almost equal for the

smallest value of  $x_{\text{Tat}}$  for DOPC:DOPE (1:1) bilayer. While Fig. 3.15 shows trends for the  $\chi^2$  minima with Tat in the hydrocarbon chain region, this position seemed energetically unfavorable as Tat is a hydrophilic molecule. Also, if Tat favored to be inserted deep in a membrane, it would be difficult for Tat to leave the membrane. This difficulty seems inefficient in terms of the HIV virus infection because Tat passing through the nuclear membrane and binding to the viral integrated DNA is crucial for proliferation of HIV infected cells. These considerations suggested that the local minima in the chain region were artifact of our models. The MD simulations performed by Dr. Kun Huang suggested that the interior positions of Tat were artifacts of our model. The simulation results are found in section 3.4.6.

Electron density profiles for DOPC/DOPS (3:1) and the nuclear membrane mimic were not successful, due to loss of diffuse scattering by Tats charge neutralization of these negatively charged membranes as described in section 3.4.1.

### 3.4.4 Hard Wall Constrain Fits

(Under construction) As seen from Table 3.6, 3.7, and 3.8, the widths of the headgroup components became smaller as Tat concentration increased in all membranes. These decreases seemed somewhat unreasonable; if Tat causes a bilayer to locally become thinner near where it is bound, we would expect that the headgroup components to become wider. Therefore, we also fitted the model with hard wall constraints on these headgroup widths. Namely, the minimum values of the widths of the headgroup components, PC and CG, were limited to the corresponding values for pure bilayers without Tat.

Table 3.9 shows results from fitting the data with lower bounds on the widths of the headgroup components for DOPC:Tat. In all cases, both headgroup widths,  $\sigma_{\text{PC}}$  and  $\sigma_{\text{CG}}$ , resulted in the same value as the value of their corresponding lower bounds. Figure 3.16 shows  $\chi^2$  landscape as a function of  $z_{\text{Tat}}$  similarly to Fig. 3.15. The  $\chi^2$  minima observed for  $z_{\text{Tat}} > 25 \text{ \AA}$  were artifact; Tat are essentially in the water region while the bilayer structure was significantly perturbed. This action-at-distance seemed unreasonable, so these minima were considered as artifact of the model. Indeed, when we fixed lipid component parameters in these fits to be identical to those of the DOPC model, we did not observe any minima with Tat in the water region. Although we did not note in the previous section, we observed similar minima

in the unbound model as well.

$x_{\text{Tat}}$	0	0.016	0.016	0.16	0.034	0.034	0.034
$\chi^2$	2961	1853	1979	2118	2398	2893	3414
$z_{\text{PC}}$	18.1	17.8	17.8	17.8	17.4	17.4	17.4
$\sigma_{\text{PC}}$	2.5	2.5	2.5	2.5	2.5	2.5	2.5
$z_{\text{CG}}$	15.0	14.7	14.7	14.7	14.3	14.3	14.3
$\sigma_{\text{CG}}$	3.0	3.0	3.0	3.0	3.0	3.0	3.0
$z_{\text{HC}}$	13.7	13.4	13.4	13.4	13.0	13.0	13.0
$\sigma_{\text{HC}}$	3.0	2.7	2.7	2.7	2.7	2.7	2.7
$\sigma_{\text{CH}_3}$	3.2	3.1	3.1	3.1	3.6	3.6	3.7
$z_{\text{Tat}}$		16.9	16.8	17.0	16.4	16.5	16.7
$\sigma_{\text{Tat}}$		2.5	3.0	3.5	2.5	3.0	3.5
$\Delta z_1$	3.1	3.1	3.1	3.1	3.1	3.1	3.1
$\Delta z_2$	1.3	1.3	1.3	1.3	1.3	1.3	1.3
$A_{\text{L}}$	71.5	73.5	73.5	73.5			
$x_{\text{Tat}}$	0.059	0.059	0.059				
$\chi^2$	3160	4298	5539				
$z_{\text{PC}}$	17.5	17.4	17.3				
$\sigma_{\text{PC}}$	2.5	2.5	2.5				
$z_{\text{CG}}$	14.4	14.4	14.3				
$\sigma_{\text{CG}}$	3.0	3.0	3.0				
$z_{\text{HC}}$	13.1	13.0	12.9				
$\sigma_{\text{HC}}$	2.7	2.7	2.7				
$\sigma_{\text{CH}_3}$	2.6	2.6	2.5				
$z_{\text{Tat}}$	16.3	16.6	17.1				
$\sigma_{\text{Tat}}$	2.5	3.0	3.5				
$\Delta z_1$	3.1	3.1	3.1				
$\Delta z_2$	1.3	1.3	1.3				
$A_{\text{L}}$							

Table 3.9: Fitting Results of the bound THG model for DOPC membranes.  $\Delta z_1 = z_{\text{PC}} - z_{\text{CG}}$  and  $\Delta z_2 = z_{\text{CG}} - z_{\text{HC}}$ .

### 3.4.5 Summary of Electron Density Profile Modeling

(Under construction) Figure 3.19 shows that the area per lipid  $A_{\text{L}}$  as defined by  $(V_{\text{L}} - V_{\text{HL}})/D_{\text{C}}$  decreased as the mole fraction of DOPE in DOPC:DOPE membranes increased. This decrease of  $A_{\text{L}}$  is qualitatively consistent with previous studies which attributed the decrease to the small size of PE head group (references?). Because



figures/Tat/SDP\_Results/X2/DOPC\_Tat\_62to1\_3p0\_bound\_X2.pdf

figures/Tat/SDP\_Results/X2/DOPC\_Tat\_28to1\_3p0\_bound\_X2.pdf

figures/Tat/SDP\_Results/X2/DOPC\_Tat\_16to1\_3p0\_bound\_X2.pdf

Figure 3.16:  $\chi^2$  as a function of  $z_{\text{Tat}}$  for DOPC with  $x_{\text{Tat}} = 0.016$ ,  $0.034$ , and  $0.059$  (from top to bottom).  $\sigma_{\text{Tat}} = 3.0$ . The bound THG model was used.

Figure 3.17: DPP graph with bound fits

Figure 3.18: DHH graph with bound fits

Figure 3.19: AL graph with bound fits

Figure 3.20: zTat graph with bound fits

DOPE has a smaller headgroup than DOPC, lipids in DOPC:DOPE bilayers pack more compactly than in DOPC bilayers. Then, more compact packing of lipids leads to a smaller  $A_L$ .

Figure 3.20 shows that Tat is located further out from the bilayer center with higher content of PE lipids. This trend is consistent with a potential mean force calculated from MD simulations (ref?), which has shown that arginine insertion costs more energy in a PE membrane than PC membrane. The higher energy cost of arginine insertion has been suggested to be due to more possible hydrogen bonding between PE groups and arginines. (After I wrote this paragraph, I realized that the argument presented does not make much sense.  $z_{\text{Tat}}$  could be larger for PE simply because DOPE membranes are thicker than DOPC membrane.  $z_{\text{Tat}}$  must be measured with respect to, say, the hydrocarbon interface. Let's do this later.)

### 3.4.6 Molecular Dynamics Simulations

(Under construction) Due to the slow relaxation in lipid bilayers and limited accuracy of the force field, a good agreement between experimental and MD simulation calculated form factors may be difficult to reach. Consequently, we carried out several constrained simulations at various  $A_L$  and  $z_{\text{Tat}}$  as described in Sec. 3.2.4. We then compared the simulated form factor  $F(q_z)$  with the experimentally measured one. Figure 3.21 shows such comparison for a DOPC bilayer. As discussed earlier, the simulated form factor shifted to larger  $q_z$  as the area per lipid was increased. From this comparison, we found the simulation at  $A_L = 70 \text{ \AA}^2$  to be the best match with the experimental form factor, yielding the lowest  $\chi^2$ . However, the form factor for  $A_L = 72 \text{ \AA}^2$  matched the experiment better than that for  $70 \text{ \AA}^2$  near  $q_z = 0.3 \text{ \AA}^{-1}$ , which suggests that a better match might lie between 70 and  $72 \text{ \AA}^2$ . This case



was not investigated further. The electron density profile for the best fit is shown in Fig. 3.22. The comparison for DOPC with  $x_{\text{Tat}} = 0.015$  where there is one Tat in each monolayer is shown in Fig. 3.23. The same comparison for DOPC with  $x_{\text{Tat}} = 0.03$  is shown in Fig. 3.24.



Figure 3.21: MD simulated form factors for DOPC at  $A_L = 68 \text{ \AA}^2$  (blue solid line),  $70 \text{ \AA}^2$  (red solid line), and  $72 \text{ \AA}^2$  (green solid line) compared to the experimental form factor (open circles) scaled vertically to best match the form factor for  $70 \text{ \AA}^2$ .

The best match for DOPC/Tat (128:4) was found when the Tats were constrained at  $18 \text{ \AA}$  away from the bilayer center (Fig. 3.26). The other best fit results were: DOPC  $A_L = 70 \text{ \AA}^2$  and DOPC/Tat(128:2)  $A_L = 72 \text{ \AA}^2$ ,  $z_{\text{Tat}} = 18 \text{ \AA}$ . It clearly indicates that with increasing Tat concentration,  $A_L$  increases. The agreement worsened as Tat was constrained to be closer to the center of the bilayer. When Tats were constrained at  $5 \text{ \AA}$  away from the bilayer center, we observed a spontaneous formation of water pores in the MD simulation. However, as shown in Fig. 3.26 the corresponding form factor calculated from MD simulations does not match well with experiments.

We summarize our results for how Tat affects the lipid bilayer in Fig. 3.27. The height of Tat,  $H_{\text{Tat}} = 8.7 \text{ \AA}$ , was the full width at half maximum of the Tat electron density profiles obtained from simulations and the cylindrical radius,  $R_{\text{Tat}} = 8.3 \text{ \AA}$ ,



Figure 3.22: The simulated, symmetrized electron density profile for DOPC at  $A_L = 70 \text{ \AA}^2$  as a function of the distance away from the bilayer center. Each component profile is labeled with its name: PC (phosphate-choline), CG (carbonyl-glycerol),  $\text{CH}_2+\text{CH}$  (methylene-methine combination),  $\text{CH}_3$  (terminal methyl). The sum of all the components is labeled as total.

figures/Tat/MD\_Results/xff/dopc-tat2\_72\_sim-exp1.pdf

figures/Tat/MD\_Results/xff/dopc-tat2\_74\_sim-exp1.pdf

Figure 3.23: MD simulated form factors for DOPC with  $x_{\text{Tat}} = 0.015$  at  $A_L = 72 \text{ \AA}^2$  (top) and  $74 \text{ \AA}^2$  (bottom), with  $z_{\text{Tat}} = 18 \text{ \AA}$  (red solid lines),  $16 \text{ \AA}$  (green solid lines), and  $14 \text{ \AA}$  (blue solid lines) compared to the experimental form factor (open circles) scaled vertically to best match the form factor for  $z_{\text{Tat}} = 18 \text{ \AA}$ .

figures/Tat/MD\_Results/xff/dopc-tat4\_74\_sim-exp1.pdf

figures/Tat/MD\_Results/xff/dopc-tat4\_76\_sim-exp1.pdf

Figure 3.24: MD simulated form factors for DOPC with  $x_{\text{Tat}} = 0.030$  at  $A_L = 74 \text{ \AA}^2$  (top) and  $76 \text{ \AA}^2$  (bottom), with  $z_{\text{Tat}} = 18 \text{ \AA}$  (red solid lines),  $16 \text{ \AA}$  (green solid lines), and  $14 \text{ \AA}$  (blue solid lines) compared to the experimental form factor (open circles) scaled vertically to best match the form factor for  $z_{\text{Tat}} = 18 \text{ \AA}$ .

$x_{\text{Tat}} = 0.015$				$x_{\text{Tat}} = 0.030$			
$A_L (\text{\AA}^2)$	$z_{\text{Tat}} (\text{\AA})$	$a$	$\chi^2$	$A_L (\text{\AA}^2)$	$z_{\text{Tat}} (\text{\AA})$	$a$	$\chi^2$
70	18	0.621	60.1	70	18	0.621	60.1
70	16	0.568	69.1	70	16	0.568	69.1
70	14	0.439	131	70	14	0.439	131
70	12	0.285	391	70	12	0.285	391
70	10	0.199	440	70	10	0.199	440
70	8	0.196	374	70	8	0.196	374
70	5	0.159	527	70	5	0.159	527
72	18	0.72	18.0	72	18	0.72	18.0
72	16	0.65	24.9	72	16	0.65	24.9
72	14	0.6	31.4	72	14	0.6	31.4
72	12	0.426	104	72	12	0.426	104
72	10	0.219	443	72	10	0.219	443
72	8	0.205	336	72	8	0.205	336
72	5	0.165	448	72	5	0.165	448
74	18	0.722	21.3	74	18	0.722	21.3
74	16	0.704	25.9	74	16	0.704	25.9
74	14	0.631	24.7	74	14	0.631	24.7
74	12	0.412	81.9	74	12	0.412	81.9
74	10	0.312	194	74	10	0.312	194
74	8	0.246	351	74	8	0.246	351
74	5	0.177	427	74	5	0.177	427

Table 3.10: Comparison of the simulated form factors to the experimental form factors.

$x_{\text{Tat}}$	$A_{\text{L}}$	$z_{\text{Tat}}$	$\langle D_{\text{PP}} \rangle$	$D_{\text{PP}}$	$x$	$\Delta t$	$H_{\text{Tat}}$	$R_{\text{Tat}}$	$R_2$	$z_{\text{phos}}$	$z_{\text{guan}}$	$\chi^2$
0	70		36.3									
0.015	72	18	35.6	32.8	35.8	3.5	9.2	8.1	15.0	14.7	15.5	18
0.015	72	16	36.1	33.0	36.3	3.3	9.4	8.0	9.0	14.9	14.5	24.9
0.015	74	18	35.0	33.0	35.1	3.3	8.6	8.3	23.9	14.9	16.5	21.3
0.015	74	16	35.0	32.1	35.2	4.2	7.6	8.9	20.4	14.0	13.5	25.9
0.030	74	18	35.3	32.6	NA	3.7	7.6	8.9	NA	14.5	15.5	24.3
0.030	74	16	35.3	31.2	NA	5.1	7.7	8.8	NA	13.1	13.5	40.1
0.030	76	18	34.2	32.0	NA	4.3	7.6	8.9	NA	13.9	16.5	14.8
0.030	76	16	34.9	31.4	NA	4.9	7.8	8.7	NA	13.3	14.5	30.4

Table 3.11: Summary of simulation results.  $\langle D_{\text{PP}} \rangle$ , phosphorus-phosphorus distance averaged over all lipids;  $D_{\text{PP}}$ , Tat-perturbed phosphorus atoms;  $x$ , thickness away from Tat;  $\Delta t$ ,  $\langle D_{\text{PP}}^{\text{DOPC}} \rangle - D_{\text{PP}}$ ;  $H_{\text{Tat}}$ , Tat height;  $R_{\text{Tat}}$ , radius of Tat cylinder;  $R_2$ , radius of the calculated in-plane Tat-perturbed region;  $R_3$ , effective radius of the simulation box.

$x_{\text{Tat}}$	$A_{\text{L}}$	$z_{\text{Tat}}$	$\langle D_{\text{PP}} \rangle$	$D_{\text{PP}}$	$\Delta t$	$H_{\text{Tat}}$	$R_{\text{Tat}}$	$R_2$	$z_{\text{phos}}$	$z_{\text{guan}}$
0.015	72.9	17.1	35.4	32.7	3.6	8.7	8.3	17.1	14.6	15.1
0.030	75.2	17.3	34.8	31.9	4.4	7.7	8.8	NA	13.8	15.4

Table 3.12: Summary of weighted average results. The caption is the same as Table 3.11.

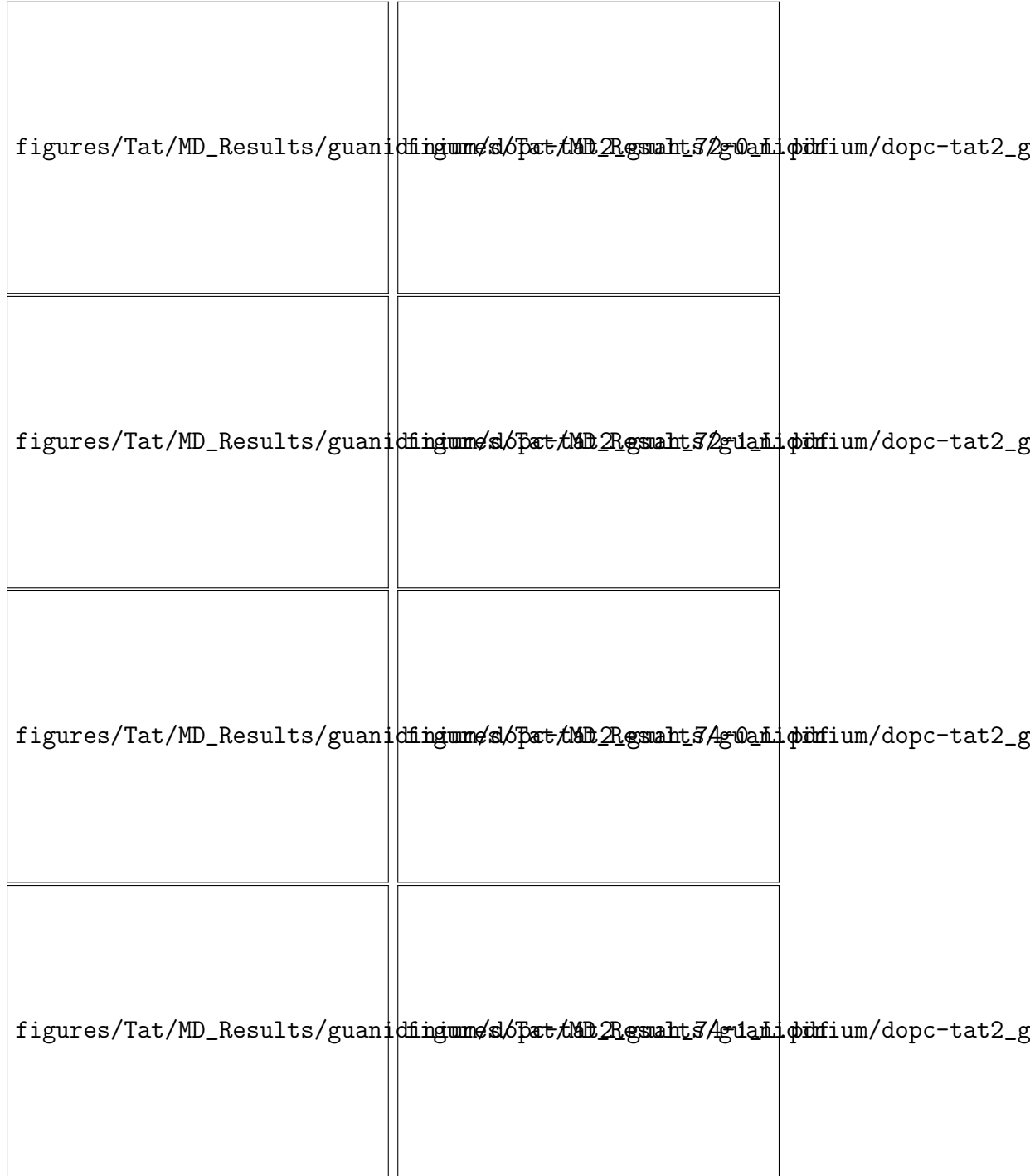


Figure 3.25: Electron density profiles of guanidinium groups from the four best matched simulations for DOPC with  $x_{\text{Tat}} = 0.015$  (one Tat on each leaflet). Tat on the lower and upper leaflets are shown on the left and right plots, respectively.

figures/Tat/figure4.pdf

Figure 3.26: MD simulated form factors (red solid lines in A and C) of Tat/(DOPC+Tat),  $x_{\text{Tat}}=0.030$ , with Tat fixed at  $z_{\text{Tat}}=18$  Å (panel A) and 5 Å (panel C) from the bilayer center compared to experimental form factors (open circles) scaled vertically to provide the best fit to the simulations. Corresponding snapshots are shown in Panels B and D in which the lipid chains are represented as grey sticks on a white background, Tats are yellow, phosphate groups are red and water is blue.



was calculated to give the measured volume. The  $Z$  distances from the center of the bilayer were derived from weighted averages of four MD simulations of Tat:DOPC 2:128. The  $\chi^2$  obtained by comparison to experiment indicated that the best  $Z_{Tat}$  lay between the simulated values of 16 Å and 18 Å and the best area/lipid  $A_L$  lay between the simulated values of 72 Å<sup>2</sup> and 74 Å<sup>2</sup>, so averages were obtained from these four combinations of  $Z_{Tat}$  and  $A_L$ , weighted inversely with their  $\chi^2$ . The average positions,  $z'_{phos}$ , of phosphates situated underneath the Tats were calculated by averaging over the phosphates whose in-plane distance,  $R$ , from the center of Tat is smaller than  $R_{Tat}$ . The simulation cell extended to 38 Å, far enough to ensure that  $z_{phos}$  for most of the lipids is the same as for DOPC. Assuming a simple linear ramp in  $z_{phos}$ , Fig. 3.27 then indicates a ring of boundary lipids that extends twice as far in  $R$  as Tat itself. Although the guanidinium electron density profile was broad (Fig. not yet included), indicating that some were pointing away from the bilayer relative to the center of Tat, more were pointing towards the bilayer center as indicated in Fig. 3.27.

figures/Tat/figure9.pdf

Figure 3.27: Location of Tat in DOPC bilayer. Tat is represented as a cylinder,  $z$  is the distance from the bilayer center, and  $R$  is the in-plane distance from the center of Tat. The average  $z$  of the lipid phosphates as a function of  $R$  and the arginine guanidiniums are shown in red and blue, respectively.

### 3.5 Discussion

Given that 8 of the 11 amino acids in Tat (47-57) are arginines and lysines, one would have suggested 20 years ago that highly charged Tat would partition strongly into solution rather than being associated with lipid bilayers. By contrast, but in agreement with more recent perspectives on arginine partitioning into the interfacial region [62], we find that Tat interacts with lipid bilayers, even with neutral DOPC and DOPC/DOPE mixtures, as well as with negatively charged DOPC/DOPS and nuclear

membrane mimic lipid mixtures. This paper presents multiple lines of evidence for a Tat/membrane interaction. Fig. ?? shows that Tat decreases the bending modulus. Although one could argue that such a decrease is only apparent and could instead be due to local changes in membrane spontaneous curvature [63], either interpretation supports a Tat-bilayer interaction. The changes with increasing Tat concentration in the X-ray membrane form factors in Fig. ?? prove that Tat affects membrane structure, and the shift of the zero positions to higher  $q_z$  suggests thinning. Thinning is substantiated by quantitative analysis of the X-ray data and by MD simulations. Fig. 7A shows that the average membrane thickness, as measured by the distance  $D_{PP}$  between phosphocholines on opposite surfaces, decreases with increasing Tat concentration. Similar thinning is shown in Fig. 7B for the distance  $D_{HH}$  between the maxima in the electron density profiles of opposite surfaces. Compared to  $D_{PP}$ ,  $D_{HH}$  is pulled towards both the carbonyl/glycerol groups and Tat because both have electron densities (  $0.4 \text{ e}/\text{\AA}^3$  ) greater than water (  $0.33 \text{ e}/\text{\AA}^3$  ) or hydrocarbon (  $0.3 \text{ e}/\text{\AA}^3$  ). Although the thinning shown in Figs. 7A and 7B is not large, it obviously requires interaction of Tat with the bilayers. Fig. 7C shows that  $A_L$  increases with increasing Tat concentration, by both model fitting and MD simulations.

It is of considerable interest to learn where Tat resides, on average, in the membrane, as this would establish a base position from which translocation would be initiated. We have combined our two main methods, MD simulations and X-ray scattering, to address this question. In general, Tats locate at the bilayer/water interface as indicated in Section 3.2, and they are close to the phosphocholine headgroup region by comparing the simulated 2ZTat in Fig. 7.D with 7.A. Although the SDP modeling of the X-ray data obtains excellent fits to the experimental form factors for a model with Tat deep in the hydrocarbon interior (see Fig. S5), the corresponding MD simulation (shown in Fig. 4.C) eliminates this spurious result. Fig. 7D also shows that modeling gives smaller values for  $z_{Tat}$  than the simulation. The modeling result is supportive of the original simulation result of Herce and Garcia that Tat resides closer to the bilayer center than do the phosphocholine groups [35]. That is a base position that would be a possibly important precursor to translocation, as would the larger  $A_L$ .

Several groups have carried out calculations and MD simulations showing that the cost of moving an arginine group from water to the bilayer center is 12-26 kcal/mol [62, 64–66] or 6-7 kcal/mol if side-chain snorkeling to the surface is taken

into account [67]. This is not inconsistent with our result that Tat interacts with the membrane because, as is well known, the bilayer is not just a hydrocarbon slab, but has interfacial headgroup regions where Tat can reside. It has been suggested that the free energy cost for charged amino acids entering the headgroup region is similar to that for partitioning into octanol, about an order of magnitude smaller free energy cost than partitioning into cyclohexane [68–70]. Simulations suggest that the free energy is smaller for an arginine residing in the interfacial region than in water, roughly by 3 kcal/mole, depending upon the lipid [62, 70]. Our results therefore appear energetically reasonable.

One concern with diffraction experiments on samples consisting of adjacent bilayers in a stack or in a multilamellar vesicle is that the samples have to be partially dried to obtain conventional diffraction data. But then there is no pure water layer between adjacent bilayers, so a hydrophilic peptide is forced into the interfacial, partially hydrophilic region of the lipid bilayer. In contrast, by using diffuse scattering, we obtained structure from experimental samples that had a range of lamellar D spacings (see Fig. 2 caption) that were considerably larger than the thickness of the bilayer in Fig. 7A, thereby providing an ample pure water space, typically greater than 20Å. The result that  $2z_{\text{Tat}}$  shown in Fig. 7D is so much smaller than our repeat spacings shows that Tat preferentially associates with the membrane rather than dissociating into water.

Tat also increases the mosaic spread observed by X-ray and neutron scattering as shown in Figs. S1-3; this is a much larger scale disordering of the stack of bilayers.

We analyzed the secondary structures of Tats from MD simulations using the Define Secondary Structure of Proteins (DSSP) program [71]. Data from the MD simulation which has the best fit to experimental X-ray form factors show that Tat contains neither  $\alpha$ -helix nor  $\beta$ -sheet structures. It appears that the membrane does not influence the conformation of solubilized Tat.

Given our structural and elastic moduli results, we now compare to other experiments in the literature. In 2008, the Wong group implicated Tats ability to induce saddle-splay curvature with a potential role of bidentate hydrogen bonding as key [25]. Rhodamine-tagged Tat only entered GUVs when the PE headgroup was included with PS and PC lipids (PS/PC/PE, 20:40:40), indicating that hydrogen-bonding, and/or curvature-promoting lipids are required for Tat translocation. In PS/PE (20:80) lipids, they found Tat caused a highly curved cubic phase using X-ray

diffraction [25]. In our experiments, there was little effect of adding DOPE to DOPC at either a 3:1 or 1:1 mole ratio on decrease in the bending modulus, bilayer thinning, or Tats outward movement with increasing concentration. Our two results are not inconsistent, however, since curvature-promotion appears not to be required for Tats ability to lower the energy required to bend nor to locate Tat in the bilayer, both of which may be important for Tat translocation. Yet Tat does translocate across membranes in their experiments only with PE in the membrane, so the ability to induce saddle-splay curvature may also be required for Tats translocation. An X-ray, neutron and AFM study reported thickening upon initial Tat binding, in contradiction to our result in Fig. 7B that shows thinning [72]. We suggest that this difference was caused by their using stiff gel phase DPPC lipid that did not allow bound Tat to perturb the bilayer. Using a variety of techniques, including high sensitivity isothermal titration calorimetry and  $^2\text{H}$ - and  $^{31}\text{P}$ -NMR, Ziegler *et al.* [?] presented evidence that the lipid bilayer remains intact upon Tat binding and our results confirm this. Finally, we compare our structural results to those obtained by solid state NMR, although at a lower hydration level than in our sample. Su *et al.* [32] found that Tat lies parallel to the bilayer surface in the headgroup region of DMPC/DMPG (8:7) bilayers, similar to our cartoon in Fig. 9.

### 3.6 Conclusion

Although a recent MD simulation using umbrella sampling [73] found that the free energy required for  $\text{R}_9\text{C}$  to traverse a membrane was smaller if a water pore was present, we could not directly test the existence of a transient water pore from our X-ray scattering experiment. This is because, even with a water pore, the translocation process still requires crossing a free energy barrier which is a non-equilibrium process. X-ray form factors measure an equilibrium state. If the form factors obtained from water pore structures agreed well with experiments, it would indicate that the pore structure was thermodynamically stable. This may be the case for some antimicrobial peptides, but certainly not for cell-penetrating peptides. Finding a kinetically competent pathway for the interesting phenomenon of translocation of highly charged Tat through hydrophobic membranes is difficult. An energetically passive translocation likely occurs very seldom on an MD simulation time scale, and it probably happens quickly, so it would not significantly change the average structure of the membrane

in which it occurs. Although our results in this paper do not reveal a kinetically competent pathway, they do show that Tat is drawn to the surface of the membrane, and is therefore ready for translocation at a region of local thinning. And they show that these interactions tend to soften (Fig. 2) the membrane and increase the area per lipid  $A_L$ , thereby likely reducing the energy barrier for passive translocation.

# Chapter 4

## Ripple Phase

When the temperature is reduced from the fluid phase, the ripple phase is observed in bilayers consisting of DMPC and DPPC lipids. This chapter discusses X-ray scattering experiments on the ripple phase formed by dimyristolphosphatidylcholine (DMPC) bilayers.

### 4.1 Introduction

(At some point, do some literature search and write up this section) The ripple phase has been a fascinating thermodynamic phase to many physicists and physical chemists since its discovery. It was originally observed in calorimetry study for alkanes by Sturtevant. Although this phase has never been reported to occur in a biologically relevant situation, it provides an interesting opportunity to study fundamental lipid interactions and their influence on the bilayer shape. (Let's find some recent papers and see if anyone says anything about biological relevance)

In the first structural study of this phase by Tardieu *et al.*, the X-ray diffraction pattern from DLPC was phased by a pattern recognition technique and the electron density map was calculated. It was shown that the structure corresponds to a 2D oblique unit cell shown in Fig. 4.1. The calculated electron density map showed that DLPC bilayers are height modulated and have a smooth, asymmetric shape. The ripple wavelength  $\lambda_r$  was reported to be 85.3 Å, the lamellar periodicity  $D$  55.3 Å, and the oblique angle  $\gamma$  110°. The electron density map reported the ripple amplitude  $A = 15$  Å in DLPC.

Various experiments have indicated the existence of two types of ripple phases: the

stable asymmetric and the metastable symmetric phase. In the asymmetric phase, a plane of reflection perpendicular to the ripple wave vector is absent. The metastable symmetric phase has been seen in DPPC bilayers, but not in DMPC.

figures/ripple/unit\_cell.pdf

Figure 4.1: Lattice structure of the asymmetric ripple phase. Unit cells are shown in dash lines. Center of bilayers are shown by thick, solid lines. Notations in the figure are (**a** and **b**: lattice unit vectors), ( $D$ :  $D$ -spacing along  $z$ ), ( $\lambda_r = |\mathbf{b}|$ : ripple wavelength), ( $\gamma$ : oblique tilt angle), ( $A$ : ripple amplitude), ( $\psi$ : chain tilt angle with respect to the  $z$  direction), and ( $x_M$ : projected length of the major arm).

The equilibrium structure of the ripple phase has been extensively studied by X-ray diffraction [1, 74–79], neutron diffraction [80, 81], AFM [], freeze fracture electron microscopy [82], and freeze fracture scanning tunneling microscopy [] techniques. In the scanning tunneling microscopy experiment [83], the three-dimensional contours of the ripple phase  $P_{\beta'}$  of dimyristoylphosphatidylcholine (DMPC) were imaged, and a ripple wavelength of 130 Å and an amplitude of 45 Å were reported.

**multilayer vs LUV. Any LUV paper report on ripple?**

From X-ray data of the DMPC ripple of unoriented samples, Wack and Webb [76] argued that the ripples have a sawtooth shape, but were unable to phase the observed pattern. Their X-ray form factor data were later phased by employing a modeling and fitting technique by Sun *et al.* [78], and the electron density map was calculated, which indicated that the ripples indeed have a sawtooth shape. The map also showed that the major arm is about twice as long as the minor arm. The bilayer thickness was found to be larger than that of the minor arm. The value of the bilayer thickness in the major arm was comparable to the thickness of DMPC bilayers in the gel phase whereas the thickness of the minor arm was comparable to that in the fluid phase.

A structural investigation by X-ray diffraction of the ripple phase of oriented dipalmitoylphosphatidylcholine (DPPC) samples indicated that hydrocarbon chains are packed in a hexagonal lattice with chains tilted in the plane perpendicular to the ripple wave vector [84]. In that study, the oblique angle  $\gamma$  was found to be 90°.

### Katsaras and Raghathan papers

Several MD (molecular dynamics) simulations have been carried out, indicating various lipid packing. de Vrie *et al.* has suggested interdigitated chain in the minor side [85].

### Some theory papers

$D$ (Å)	$\lambda_r$ (Å)	$\gamma$ (deg)
55.0	159.4	99.0
57.0	140.8	97.6
57.3	151.6	97.8
57.4	148.4	97.6
57.5	144.1	97.8
57.5	141.9	98.0
58.0	140.1	98.2
57.8	145.0	98.2
58.0	141.7	98.4
59.8	129.6	97.3
60.6	130.1	97.0
61.5	130.8	96.5
62.4	122.0	95.9
63.9	123.1	94.9
64.9	120.3	92.3

Table 4.1: Lattice constants for DMPC at  $T = 18.0$  °C reported by Wack and Webb [76]. The data collected and analyzed in this thesis are colored blue.

## 4.2 Materials and Methods

### 4.2.1 Sample Preparation

DMPC was purchased from Avanti Polar Lipids and used without further purification. Oriented thin films were deposited on clean silicon wafers with a chloroform:methanol 2:1 (volume ratio) mixture following the rock and roll procedure [86]. In previous synchrotron experiments, the samples were created and annealed more than a week in advance and stored in a refrigerator. The quality of these samples measured by their mosaic spread was found to worsen over time after the samples were annealed. Therefore, to ensure the best sample quality, the samples were annealed for approximately



12 hours just before the X-ray experiment. Figure 4.2 shows a picture of the annealing chamber. To achieve gentle but efficient hydration of a sample, filter papers were installed. For successful annealing, it must be emphasized that the annealing chamber should equilibrate in an annealing oven prior to putting a sample in the chamber. When a sample was put in the chamber sitting at a room temperature and then the system was placed inside the oven, warmer water vapor inside the chamber condensed on the cooler sample, causing so called flooding of oriented sample. A small drop of water on an oriented film is detrimental for the orientation quality because the entropy-driven formation of unilamellar vesicles causes oriented bilayers to peel off one by one.

Figure 4.2: A picture of an annealing chamber. Need to take a picture

The sample for the grazing incident wide angle study was prepared in the same way as for low angle study. In order to minimize the geometric broadening, the sample was trimmed to 1 mm in width along the beam direction.

The sample for transmission study was deposited on a thin, 35 micron, silicon wafer, and oriented following the rock and roll procedure [86]. See also Sec. 3.2.1. Because the wafer was very fragile, attaching the sample to a sticky thing was impossible. Instead, the sample was attached to a plastic cap on a small vial with a small amount of heat sink compound at a corner of the wafer. The wafer was stable enough for rocking.

## 4.2.2 Instrumental Resolution

Talk about divergence, dispersion, and geometric broadening.

### Divergence

### Energy dispersion

multilayer vs Si crystal

### Geometric Broadening

WAXS vs LAXS Make a table (in pixel and  $q$ )



### 4.2.3 Low Angle X-ray Scattering Experiment

(Transmission was in 2011) The low resolution X-ray scattering experiment was carried out at the Cornell High Energy Synchrotron Source (CHESS) G1 station in three different runs (2011, 2012, and 2013). The low angle X-ray scattering (LAXS) data analyzed in this thesis were collected in 2013. The X-ray beam was set up by the station scientist, Dr. Arthur Woll. A W/B<sub>4</sub>C multilayer monochromator with energy bandwidth  $\Delta E/E$  of 1.5% was used, providing a very intense X-ray beam. The energy of the X-ray beam was 10.55 keV, corresponding to a wavelength of 1.175 Å. The horizontal and vertical divergence of the beam were  $4.2 \times 10^{-5}$  rad and  $1.6 \times 10^{-4}$  rad, respectively. The beam shape, measured through a semi-transparent 200  $\mu\text{m}$  thick molybdenum (Mo) beam stop, is shown in Fig. 4.3 and 4.4. The horizontal beam width was 2.3 pixels (0.16 mm). The vertical beam width was approximately 1 mm, tall enough to cover the entire sample when the sample was tilted by 7°. The sample was rocked during X-ray exposure between -1.6° and 7° in order to observe many diffraction peaks in one data collection. The sample to detector distance was 359.7 mm, measured by indexing silver behenate Bragg peaks. The D-spacing of silver behenate is known to be 58.367 Å.

Occasionally, sheets of molybdenum (Mo), each nominally 25  $\mu\text{m}$  were used to attenuate the incoming beam. These sheets were installed by Dr. Arthur Woll in the upstream of the sample chamber. The attenuation length  $\mu$  of 10.55 keV X-ray in Mo is 13.74  $\mu\text{m}$  [87]. For a 25  $\mu\text{m}$  thick Mo attenuator, the attenuation factor is calculated to be  $[\exp(-25/13.74)]^{-1} = 6.2$ . The exact attenuation factor was determined by comparing X-ray images collected with and without the attenuator, shown in Fig. 4.6 and 4.7. The attenuation factor of the nominally 25  $\mu\text{m}$  thick Mo was found to be 6.9 for the wavelength used (1.175 Å).

Sheets of Mo were also used as a beam stop downstream of the sample, just outside the hydration chamber, to attenuate the beam and strong orders. 100 and 200  $\mu\text{m}$  were used to attenuate strong orders and 225  $\mu\text{m}$  to attenuate the beam. To avoid saturation of CCD pixels by the very intense beam, the beam stop was always set to block the beam.

A few Bragg peaks in the low angle X-ray scattering of the ripple phase were very strong, leading to saturation of CCD pixels for data collection with a long exposure time. In order to probe a wide range of  $q$ -space, three images were taken: 1) a short, one second exposure with a nominally 25 micron molybdenum attenuator installed in



Figure 4.3: The horizontal profile of the beam used in the low resolution study. Each pixel was 0.07113 mm, which gave a CCD angular resolution  $\Delta\theta$  of  $0.0057^\circ$ , corresponding to  $\Delta q = 0.0011 \text{ \AA}^{-1}$  at the sample to detector distance of 359.7 mm. The beam FWHM = 1.7 pixels, giving  $\Delta\theta = 0.010^\circ$  or  $\Delta q = 0.0019 \text{ \AA}^{-1}$ .



Figure 4.4: The vertical profile of the beam used in the low resolution study. The beam height = 15 pixels = 1.1 mm.

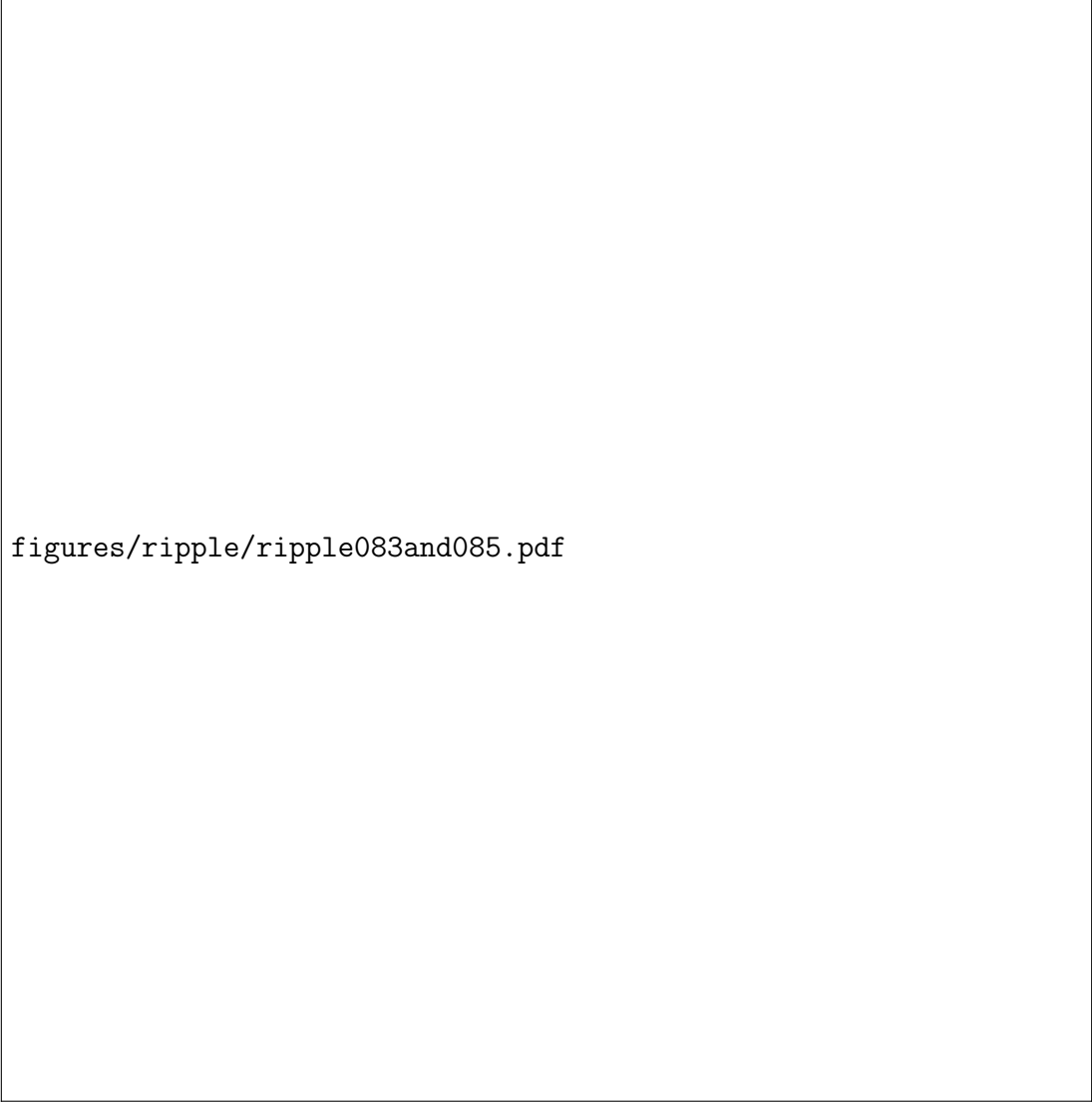
the upstream of the sample to reduce the intensity of the incoming X-ray beam, 2) one second exposure without the beam attenuator, and 3) 60 second exposure with a beam stop blocking the very intense (1,0) and (2,0) peaks. See Fig. 4.5. Then, the integrated intensity of (1,0) peak was measured from the first image. This value was multiplied by 6.9 to account for the beam attenuation and by 60 to scale with the exposure time. The intensity of (2,0) and (2,-1) were measured from the second image, also multiplied by 60 to account for the shorter exposure time. The intensity of the rest of the observed peaks were measured from the third image.

The integrated intensity of each peak was obtained using the Nagle lab tvview software developed by Dr. Yufeng Liu [39] by putting a box around a peak and summing up the intensity in those pixels that fall inside the box. The background scattering was estimated by measuring the intensity in pixels near the peak but not containing any peak tail. The choice of box size was made according to the width of each peak. Because of mosaic spread in the sample, the peaks were wider for higher orders. Consequently, the box was made wider for higher orders. The box size was chosen so that approximately 80% of the peak intensity was counted toward the integrated intensity.

#### 4.2.4 Near Grazing Incidence Wide Angle X-ray Scattering Experiment

The high resolution X-ray scattering experiment was also carried out at the G1 station. To achieve a higher instrumental resolution than that for the low angle X-ray scattering experiment described in a previous section, a (111) silicon monochromator was used, which gave  $\Delta E/E$  of 0.01%. Due to the geometry of the G1 station, the Si monochromator was placed in the G1 hutch, in series with the multilayer monochromator. The instrument was set up by the G1 station scientist, Author Woll, and the assistant scientist, Dr. Robin Baur.

The energy of the beam was 10.55 keV (wavelength = 1.175 Å). The horizontal and vertical divergence of the X-ray beam were  $4.2 \times 10^{-5}$  rad and  $1.6 \times 10^{-4}$  rad, respectively. The horizontal beam width was 4 pixels (0.28 mm) as shown in Fig. ???. With this beam, the scattering resolution in the wide angle region was dominated by the geometric broadening. The broadening was due to the sample width along the beam direction and the horizontal beam width (Fig. 4.10. From the geometry of the



figures/ripple/ripple083and085.pdf

Figure 4.5: 1 second exposure (left) and 60 second exposure (right) of the low angle X-ray scattering from the DMPC ripple phase in gray log scales. The index  $h$  is labeled in green.  $(3, k)$  reflections are identified in cyan. The shadow cast by 100  $\mu\text{m}$  thick molybdenum attenuator blocking strong  $(1,0)$  and  $(2,0)$  orders in the right image is labeled as attenuator and extends from  $q_z = 0 \text{ \AA}^{-1}$  to  $0.2 \text{ \AA}^{-1}$ .  $D = 57.8 \text{ \AA}$ ,  $\lambda_r = 145.0 \text{ \AA}$ , and  $\gamma = 97.8^\circ$ .

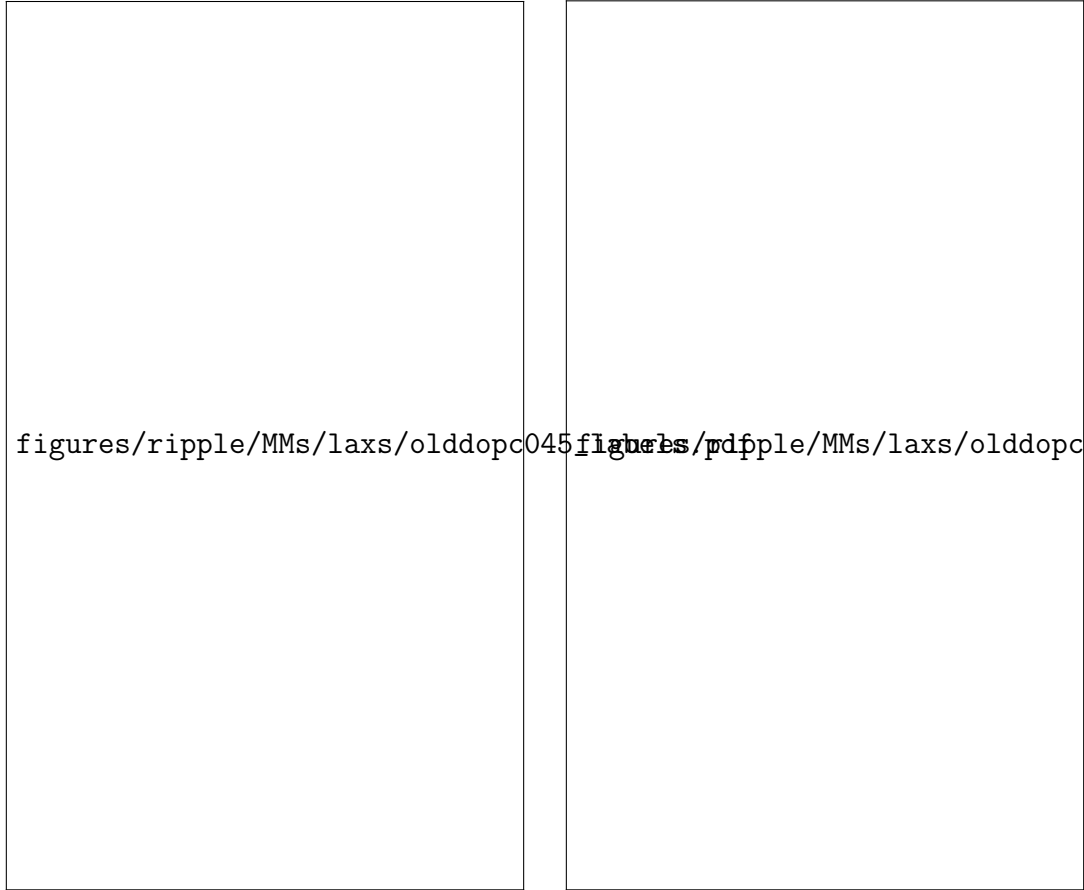


Figure 4.6: CCD images of X-ray scattering taken with (left) and without (right) a nominally  $25\text{ }\mu\text{m}$  thick Mo attenuator. These data were taken at a fixed angle of incidence  $\omega = 0.8^\circ$ . The sample was an oriented film of DOPC:DOPE (3:1) in the fluid phase at  $37^\circ\text{C}$ . The wavelength was  $1.175\text{ }\text{\AA}$ , the same as the one used for the ripple phase experiment. The same gray scale is used in both images.  $100\text{ pixel} = 0.11\text{ }\text{\AA}^{-1}$  in  $q$ . A small dot located about  $(p_x, p_z) = (520, 170)$  between the first and second orders is a specular reflection from the substrate. The exposure times were 1 second.

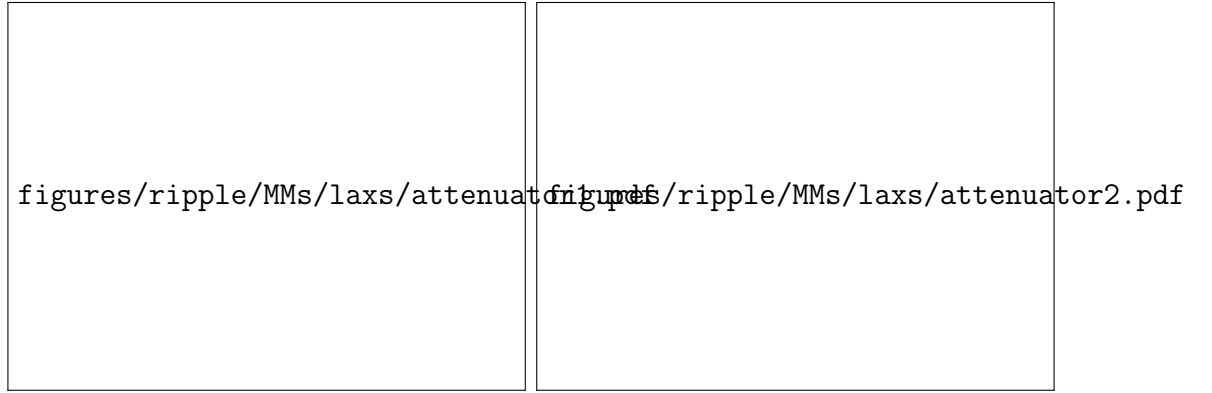


Figure 4.7: Vertical  $p_z$  slices of X-ray images shown in Fig. 4.6 (left). The scattering intensity measured with the attenuator (red solid circles) was multiplied by a factor of 6.9 and compared to the intensity measured without the attenuator (black solid circles, right).



experiment, the geometric broadening  $\Delta x$  can be determined,

$$\Delta x = \Delta x_{\text{beam}} + w_s \tan(2\theta).$$

The total scattering angle  $2\theta$  for the ripple WAXS was approximately  $16^\circ$ . To minimize the contribution from the sample, the sample was trimmed to 1 mm along the beam direction. (edge effect) The width of 1 mm was chosen because (1) I could not trim more without a more sophisticated device than a simple razor blade, (2) a very narrow sample would be a weak scattering body, and (3) any effect from the sample edge might become too significant to ignore. Given the above reasons and due to limited availability of synchrotron beam time, I considered a 1 mm width to be reasonable. With these values, the resolution is  $\Delta x = 0.57 \text{ mm} = 8 \text{ pixels}$ , which would be the unresolved width of an intrinsically infinitely sharp wide angle peak. The sample to detector distance were 220.6 mm, measured using silver behenate. Then, the minimum peak width measured in  $q$ -space would be  $\Delta q \approx 0.014 \text{ \AA}^{-1}$ . Wide angle X-ray scattering was collected at an incident angle of  $0.2^\circ$ . The total external reflection from an air-lipid interface occurs approximately at  $0.1^\circ$  and  $0.17^\circ$  for air-silicon interface, so  $0.2^\circ$  is not quite grazing incidence. Grazing incidence usually implies that the incident angle is less than the critical angle for a total external reflection. Therefore,  $0.2^\circ$  is called near grazing incidence in this thesis.

#### 4.2.5 Transmission Wide Angle X-ray Scattering Experiment


The transmission wide angle X-ray scattering (TWAXS) experiment was also carried out at the G1 station, and a similar instrumental resolution to the one in Sec. 4.2.3 was used. The sample to detector distance was measured to be 170 mm using silver behenate when the angle of incidence  $\omega$  was  $0^\circ$ . The incident angle was set to  $-45^\circ$  for transmission data collection. A  $35 \text{ }\mu\text{m}$  thick silicon substrate absorbs an X-ray at 10.5 keV by 20% [87]. To measure a D-spacing, mosaic spread of the sample was exploited. Unfortunately, the axis of the rotation motor did not coincide with the sample axis, so the sample to detector distance varied as  $\omega$  was varied. To accurately measure the sample to detector distance, low angle scattering was collected at a fixed  $\omega$ . Due to the sample mosaic spread, many orders were visible. While the relative intensity of each order was inaccurate, the position of peaks was the same as that observed with a rotating sample. The sample to detector distance was accurately measured at  $\omega =$



Figure 4.8: The horizontal profile of the beam used in the high resolution experiment. The CCD angular resolution  $\Delta\theta = 0.0092^\circ$  corresponding to  $\Delta q = 0.0017 \text{ \AA}^{-1}$ , at the sample to detector distance of 220.6 mm. The beam FWHM = 3.7 pixels = 0.26 mm, giving  $\Delta\theta = 0.034^\circ$  or  $\Delta q = 0.0063 \text{ \AA}^{-1}$ .



Figure 4.9: The vertical profile of the beam used in the high resolution experiment. The beam height = 9 pixels = 0.64 mm.



figures/ripple/MMs/waxs/geometric\_broadening.pdf

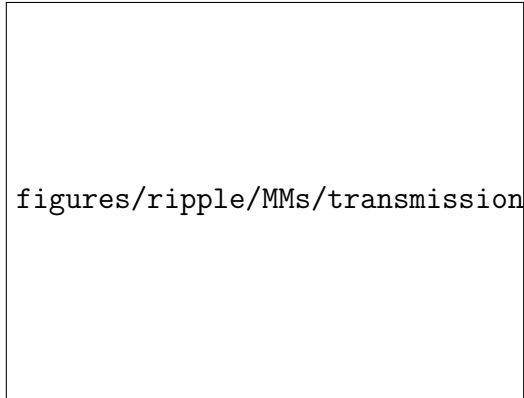
Figure 4.10: In-plane geometric broadening due to the sample width  $w_s$  and the beam width  $\Delta x_{\text{beam}}$ . A top view of the sample (green) on the Si wafer (gray) and the incoming and diffracted X-rays (bounded by red solid lines) are shown. The total in-plane scattering angle for a lipid chain-chain correlation is labeled as  $2\theta$ , and the geometric broadening as  $\Delta x$ .

$0^\circ$  using a silver behenate sample. From the geometry of the sample holder, a shift in the sample to detector distance was estimated for an arbitrary incident angle  $\omega$ .

Explain how we estimated the sample to detector distance at  $\omega = -45^\circ$ . Explain how we leveled the sample (using the sample scattering and ascan). The background scattering was collected by replacing the sample with a bare wafer.

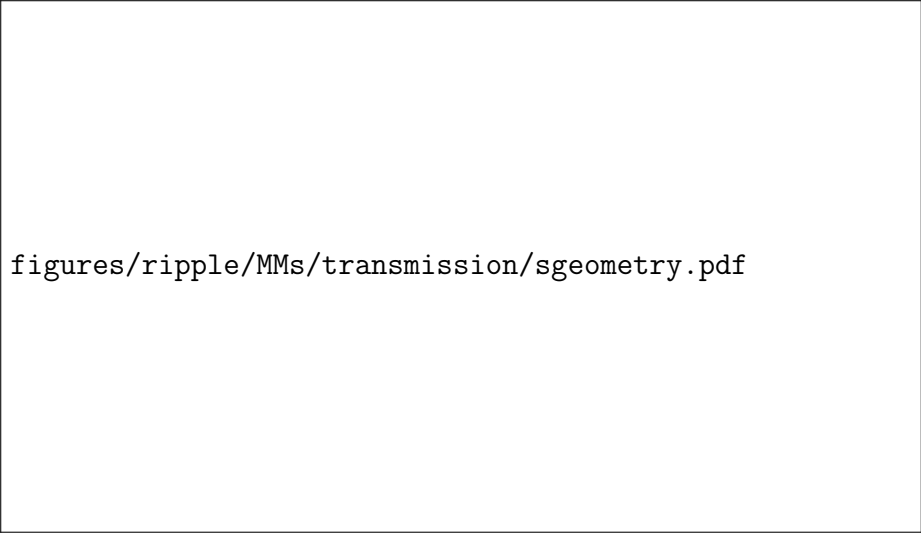


Figure 4.11: Schematics of the sample holder in the transmission mode. Side (left) and top (right) views are shown. The thickness of the Si wafer =  $35 \mu\text{m}$ . The thickness of the sample  $\approx 10 \mu\text{m}$ . The distance between the axis of rotation and sample =  $21.1 \text{ mm}$ .




figures/ripple/MMs/transmission/sample\_holder1.pdf

Figure 4.12: Picture of the sample holder looking from above. A lead tape was attached to the back of the sample holder to help reduce the background scattering, typically coming from the air gap between the flightpath snout and the mylar window of the chamber.




figures/ripple/MMs/transmission/sgeometry.pdf

Figure 4.13: Circular path followed by the sample as the angle of incidence  $\omega$  was changed. The sample to detector distance and  $D$ -spacing of the sample were measured in the LAXS mode, where  $\omega = 1^\circ$ . WAXS images were collected at the transmission mode, where  $\omega = -45^\circ$ . The  $z$  position of the sample was slightly higher at the LAXS mode than at the transmission mode, so the sample holder was vertically shifted for different modes.




figures/ripple/MMs/transmission/geometric\_broadening1.pdf

Figure 4.14: Geometric broadening in TWAXS. The cross section of the incoming X-ray with the sample and the CCD detector are both shaded in red.



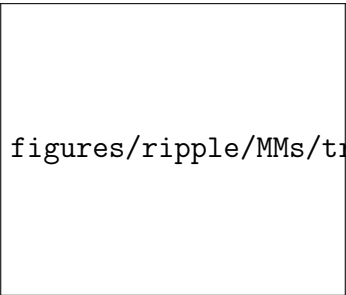
figures/ripple/MMs/transmission/geometric\_broadening2.pdf

Figure 4.15: Top view of geometric broadening in TWAXS. The cross section of the incoming X-ray with the sample is shaded in red.



figures/ripple/MMs/transmission/geometric\_broadening3.pdf

Figure 4.16: Side view of geometric broadening in TWAXS. The cross section of the outgoing X-ray with the CCD detector is shaded in red.



figures/ripple/MMs/transmission/geometric\_broadening4.pdf

Figure 4.17: Projection of rectangular beam on the detector.

## 4.3 LAXS: analysis

### 4.3.1 Lattice Structure

The unit cell vectors for the two-dimensional oblique lattice shown in Fig. 4.1 can be expressed as

$$\mathbf{a} = \frac{D}{\tan \gamma} \hat{\mathbf{x}} + D \hat{\mathbf{z}} \quad (4.1)$$

and

$$\mathbf{b} = \lambda_r \hat{\mathbf{x}}. \quad (4.2)$$

The corresponding reciprocal lattice unit cell vectors are

$$\mathbf{A} = \frac{2\pi}{D} \hat{\mathbf{z}} \quad (4.3)$$

and

$$\mathbf{B} = \frac{2\pi}{\lambda_r} \hat{\mathbf{x}} - \frac{2\pi}{\lambda_r \tan \gamma} \hat{\mathbf{z}}. \quad (4.4)$$

The reciprocal lattice vector,  $\mathbf{q}_{hk}$  for the Bragg peak with Miller indices  $(h, k)$  is

$$\mathbf{q}_{hk} = h\mathbf{A} + k\mathbf{B}, \quad (4.5)$$

so its Cartesian components are

$$\mathbf{q}_{hk} \cdot \hat{\mathbf{x}} = q_{hk}^x = \frac{2\pi k}{\lambda_r} \equiv q_k^x \quad (4.6)$$

$$\mathbf{q}_{hk} \cdot \hat{\mathbf{y}} = q_{hk}^y = 0 \quad (4.7)$$

$$\mathbf{q}_{hk} \cdot \hat{\mathbf{z}} = q_{hk}^z = \frac{2\pi h}{D} - \frac{2\pi k}{\lambda_r \tan \gamma}. \quad (4.8)$$

Our sample consists of many ripple domains with a uniform distribution of in-plane directions of the ripple wave vector,  $\mathbf{b}$  in Fig. 4.1. In this case,  $q_{hk}^x$  and  $q_{hk}^y$  are combined to give  $q_{hk}^r = 2\pi k/\lambda_r$ .



### 4.3.2 Sample $q$ -space

The incoming and outgoing wavevectors of the x-ray beam in Fig. 4.18 are given by

$$\mathbf{k}_{\text{in}} = \frac{2\pi}{\lambda} \hat{\mathbf{y}}, \quad \mathbf{k}_{\text{out}} = \frac{2\pi}{\lambda} (\sin 2\theta \cos \phi \hat{\mathbf{x}} + \cos 2\theta \hat{\mathbf{y}} + \sin 2\theta \sin \phi \hat{\mathbf{z}}), \quad (4.9)$$

where  $\lambda$  is the wavelength of x-ray,  $2\theta$  is the total scattering angle, and  $\phi$  is the angle measured from the equator on the detector. The scattering vector (also called momentum transfer vector) is the difference between  $\mathbf{k}_{\text{in}}$  and  $\mathbf{k}_{\text{out}}$ ,

$$\begin{aligned} \mathbf{q} &= \mathbf{k}_{\text{out}} - \mathbf{k}_{\text{in}} \\ &= q (\cos \theta \cos \phi \hat{\mathbf{x}} - \sin \theta \hat{\mathbf{y}} + \cos \theta \sin \phi \hat{\mathbf{z}}), \end{aligned} \quad (4.10)$$

where  $q = 4\pi \sin \theta / \lambda$  is the magnitude of the scattering vector. When the sample is rotated by  $\omega$  about the lab x-axis in the clockwise direction as shown in Fig. 4.18, the sample  $q$ -space also rotates and are given by

$$\hat{\mathbf{e}}_{\mathbf{x}} = \hat{\mathbf{x}}, \quad \hat{\mathbf{e}}_{\mathbf{y}} = \cos \omega \hat{\mathbf{y}} + \sin \omega \hat{\mathbf{z}}, \quad \hat{\mathbf{e}}_{\mathbf{z}} = -\sin \omega \hat{\mathbf{y}} + \cos \omega \hat{\mathbf{z}}. \quad (4.11)$$

From Eq. (4.10) and (4.11), we find Cartesian components of the sample  $q$ -space to be


$$\begin{aligned} q_x &= \mathbf{q} \cdot \hat{\mathbf{e}}_{\mathbf{x}} = q \cos \theta \cos \phi, \\ q_y &= \mathbf{q} \cdot \hat{\mathbf{e}}_{\mathbf{y}} = q (-\sin \theta \cos \omega + \cos \theta \sin \phi \sin \omega), \\ q_z &= \mathbf{q} \cdot \hat{\mathbf{e}}_{\mathbf{z}} = q (\sin \theta \sin \omega + \cos \theta \sin \phi \cos \omega). \end{aligned} \quad (4.12)$$

The position,  $(X, Z)$ , of a CCD pixel is measured with respect to the beam and given by

$$X = S \tan 2\theta \cos \phi, \quad Z = S \tan 2\theta \sin \phi, \quad (4.13)$$

where  $S$  is the distance between the sample and detector.

From a model for the electron density of a lipid bilayer, one calculates the X-ray scattering intensity pattern,  $I(\mathbf{q})$ . Then, Eq. (4.12) and (4.13) relate  $I(\mathbf{q})$  to the experimentally measured intensity pattern,  $I(X, Z)$ . It is important to remember that a given pixel position,  $(X, Z)$ , corresponds to a triplet  $(q_x, q_y, q_z)$ . Fully exploring the sample  $q$ -space requires changing  $\omega$  for a fixed wavelength, which was achieved



figures/ripple/analysis/laxs\_setup.pdf

Figure 4.18: Experimental reflectivity geometry.

by continuously rotating the sample with a motor. In the ripple phase, because our sample has in-plane rotational symmetry, the ripple side peaks ( $h, k \neq 0$ ) make up Bragg rings while the main peaks ( $h, k = 0$ ) are still delta function like (see Fig. 4.19) in  $q$ -space. In order for the main peak to be observed,  $\omega$  must be equal to  $\theta_B$ , but the side peaks are observed at any  $\omega$ . Those side peaks get slightly smeared due to integration over  $q_y$ .

For low angle x-ray scattering (LAXS), it is convenient to linearize the above equations in terms of  $\theta$  and  $\omega$ . In the small angle approximation,  $\sin \phi \approx Z/(2S\theta)$  and  $\cos \phi \approx X/(2S\theta)$ , and

$$\begin{aligned} q_x &\approx \frac{4\pi\theta \cos \phi}{\lambda} \approx kX/S \\ q_y &\approx q_z\omega - \frac{4\pi\theta^2}{\lambda} \approx q_z\omega - \frac{\lambda q_z^2}{4\pi} \\ q_z &\approx \frac{4\pi\theta \sin \phi}{\lambda} \approx kZ/S, \end{aligned} \tag{4.14}$$

with  $k = 2\pi/\lambda$ . For wide angle X-ray scattering, the exact relations given by Eq. (4.12) are necessary. Especially in the transmission experiment, where  $\omega$  is large, an observed X-ray pattern appears nontrivial and becomes almost impossible to analyze without the use of Eq. (4.12). The transmission experiment is discussed in Sec.4.9.

### 4.3.3 Lorentz Correction

Our sample has in-plane rotational symmetry about the  $z$ -axis. Ignoring mosaic spread to which we will come back later, this means that the sample consists of many domains with differing ripple directions, all domains being parallel to the substrate. In sample  $q$ -space, ripple ( $h, k \neq 0$ ) side peaks are represented as rings centered at the meridian, or  $q_z$ -axis, while ( $h, k = 0$ ) main peaks are still points on the meridian (see Fig. 4.19). Then, for an arbitrary incident angle  $\omega$ , ( $h, 0$ ) peaks are not observed while side peaks are observed for a range of  $\omega$  as will now be explained.

In order to capture all ( $h, k$ ) peaks in one X-ray exposure, the sample was continuously rotated over a range of  $\omega$ ,  $\Delta\omega$ , about the  $x$ -axis. As a result of this rotation, the ( $h, 0$ ) main peaks become arcs that subtend an angle  $\Delta\omega$ , as shown in Fig. 4.20, with its length equal to  $\Delta\omega q_{h0}^z$ . The detector records the intersections of these arcs

figures/ripple/analysis/ripple\_sample\_qspace.pdf

Figure 4.19: Ewald sphere construction for the ripple phase diffraction in the low angle regime. A ripple  $k = 0$  peak is the solid, black circle on the  $q_z$ -axis. A ripple  $k \neq 0$  ring is the black ring centered about the  $q_z$ -axis. The portion of the ring that is inside the Ewald sphere is shown as a red dashed line and the portion of the ring that is outside but behind the Ewald sphere is shown as a black dotted line. The magnitude of the total scattering angle is exaggerated. With a wavelength of  $1.175 \text{ \AA}$ , the magnitude  $|\mathbf{k}_{\text{in}}| = 5.35 \text{ \AA}^{-1}$ . For a  $h = 5$  peak,  $q_{50}^z = 0.54 \text{ \AA}^{-1}$ , one tenth of  $k_{\text{in}}$ .

with the Ewald sphere, so the intrinsic scattering intensity of the  $(h, k = 0)$  reflections is the product of the observed intensity,  $I_{hk}^{\text{obs}}$  with the arc length, that is,

$$I_{h0} = \Delta\omega q_{h0}^z I_{h0}^{\text{obs}}. \quad (4.15)$$

This is the usual Lorentz correction for lamellar orders.

Now, we consider relative intensity of side peaks for a given order  $h$ . As described earlier,  $(h, k \neq 0)$  side peaks are represented as rings whose radius is  $q_{hk}^r$  in the sample  $q$ -space. Because only the domains with the right ripple direction can satisfy the Bragg's condition at a given fixed angle  $\omega$ , the intrinsic scattering intensity in this ring is reduced by a factor of  $2\pi q_k^r$  compared to the  $(h, 0)$  reflections. This reduction of intensity can be nicely visualized by the Ewald sphere construction shown in Fig. 4.19, which shows that the entire rings are not intersected by the Ewald sphere at a fixed angle. Then, the intrinsic scattering intensity in a ring is

$$I_{hk \neq 0} \propto 2\pi q_{hk}^r I_{hk}^{\text{obs}}. \quad (4.16)$$

During an X-ray exposure, the sample  $q$ -space rotates and the rings are intersected by the Ewald sphere at all our experimental incident angles  $\omega$ . However, as Fig. 4.21 shows, only small parts of the rings are actually intersected with the Ewald sphere. To obtain the full expression for  $(h, k \neq 0)$  reflections, we now turn to a more rigorous calculation.

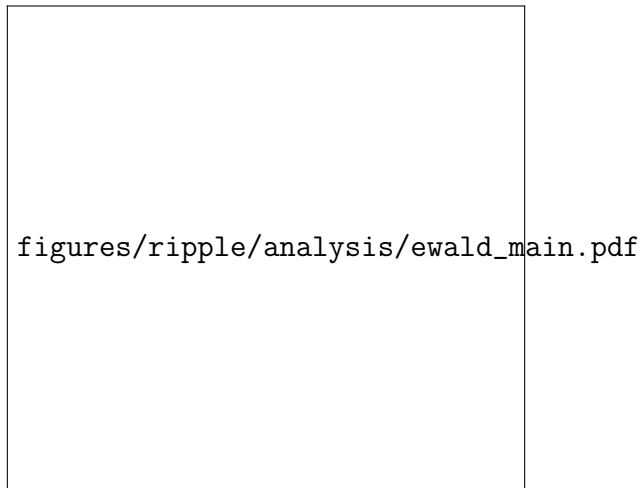


Figure 4.20: Side view of an arc of  $k = 0$  peak shown as a thick blue line.

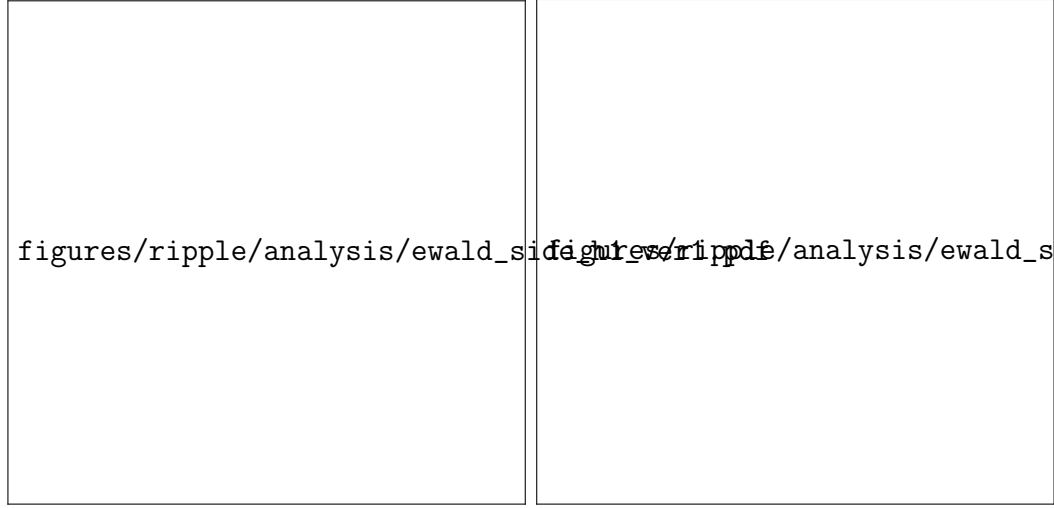


Figure 4.21:  $q$ -space representations of Bragg peaks and Bragg rings for  $h = 1$  and  $2$  and  $k = 0, 1$ , and  $2$  in  $q_{hk}^z$  planes. The intersection between the Ewald sphere and a Bragg peak/ring is indicated in red. The observed intensity for the  $k \neq 0$  orders is proportional to the fraction of the length of red arcs in the circumference. This fraction is equal to one for  $k = 0$  reflections. Because the reflections are not in the same  $q_z$  plane, the range of  $q_y$  integration indicated by the height of the gray rectangle is different for different  $h$  orders. For  $\gamma \neq 90^\circ$ , the range of  $q_y$  integration is slightly different for different  $k$  reflections with the same  $h$ . The values shown are for  $D = 58$  Å,  $\lambda_r = 145$  Å,  $\gamma = 90^\circ$ , and  $\lambda = 1.175$  Å. The magnitude of curvature of arcs is exaggerated.

Mathematically, the rotation is equivalent to an integration over  $\omega$ . In low angle X-ray scattering,  $q_z$  is nearly constant at a given pixel as  $\omega$  is changed, which can be seen from Eq. (4.14). As Eq. (4.14) shows,  $\omega$  dependence appears only through  $q_y$ , so rotating the sample is realized by integrating over  $q_y$ ; formally, we write  $d\omega = dq_y/q_z$ . To derive the integration limits on  $q_y$ , let us consider two cases: (1) When  $\omega \leq 0$ , the incoming X-ray beam is blocked by the back of the substrate. This sets the lower limit of  $\omega$  to 0. Plugging  $\omega = 0$  in Eq. 4.14), we find the lower limit of the  $q_y$  integration to be  $-\lambda q_z^2/(4\pi)$ . (2) When  $\omega \geq 2\theta$ , the substrate blocks the outgoing X-ray, so the maximum  $\omega = 2\theta$ . Within the small angle approximation,  $q_z \approx 4\pi\theta/\lambda$ . Then, the maximum  $\omega$  can be expressed as  $\lambda q_z/(2\pi)$ . Plugging this expression for  $\omega$  in Eq. (4.14), we find the upper limit of the  $q_y$  integration to be  $\lambda q_z^2/(4\pi)$ . Also integrating over the detector pixels  $X$  and  $Z$  to obtain integrated intensity, we write the observed intensity as

$$\begin{aligned} I_{hk}^{\text{obs}} &\propto \int dX \int dZ \int d\omega I_{hk} \\ &\propto \int dq_x \int dq_z \int_{-\frac{\lambda q_z^2}{4\pi}}^{\frac{\lambda q_z^2}{4\pi}} \frac{dq_y}{q_z} I_{hk}(\mathbf{q}), \end{aligned} \quad (4.17)$$

where  $1/q_z$  factor in  $q_y$  integration is the usual Lorentz polarization factor in the small angle approximation.

For a crystalline sample with in-plane rotational symmetry, the structure factor of a ripple Bragg peak is

$$S_{hk}(\mathbf{q}) = S_{hk}(q_r, q_z) = \frac{1}{2\pi q_r} \delta(q_r - q_{hk}^r) \delta(q_z - q_{hk}^z), \quad (4.18)$$

where  $q_{hk}^r = 2\pi|k|/\lambda_r$ . Thus, the scattering pattern in the ripple phase is a collection of Bragg rings for  $k \neq 0$  centered at the meridian and the Bragg peaks for  $k = 0$  located along the meridian. The scattering intensity is  $I(\mathbf{q}) = |F(\mathbf{q})|^2 S(\mathbf{q})$ , where  $F(\mathbf{q})$  is the form factor. After the  $q_z$  integration, the observed, integrated intensity of  $(h, k)$  peak is proportional to

$$I_{hk}^{\text{obs}} \propto \frac{|F_{hk}|^2}{q_{hk}^z} \int dq_x \int_{-q_{hk}^{y0}}^{q_{hk}^{y0}} dq_y \frac{\delta(q_r - q_{hk}^r)}{2\pi q_r}, \quad (4.19)$$

where  $q_{hk}^{y0} = \lambda(q_{hk}^z)^2/(4\pi)$ . For side peaks ( $k \neq 0$ ), we have

$$\begin{aligned} \int dq_x \int_{-q_{hk}^{y0}}^{q_{hk}^{y0}} dq_y \frac{\delta(q_r - q_{hk}^r)}{2\pi q_r} &\approx \int_{-q_{hk}^{y0}/q_{hk}^r}^{q_{hk}^{y0}/q_{hk}^r} d\phi \int dq_r q_r \frac{\delta(q_r - q_{hk}^r)}{2\pi q_r} \\ &= \frac{q_{hk}^{y0}}{\pi q_{hk}^r}. \end{aligned} \quad (4.20)$$

For main peaks ( $k = 0$ ), we have

$$\begin{aligned} \int dq_x \int_{-q_{hk}^{y0}}^{q_{hk}^{y0}} dq_y \frac{\delta(q_r - q_{hk}^r)}{2\pi q_r} &= \int_0^{2\pi} d\phi \int dq_r q_r \frac{\delta(q_r - q_{hk}^r)}{2\pi q_r} \\ &= 1 \end{aligned} \quad (4.21)$$

Using Eq. (4.19 – 4.21), we write the observed integrated intensity as

$$I_{h0}^{\text{obs}} \propto \frac{|F_{h0}|^2}{q_{h0}^z} \quad (4.22)$$

$$I_{hk}^{\text{obs}} \propto \frac{|F_{hk}|^2}{q_{hk}^z} \frac{q_{hk}^{y0}}{\pi q_{hk}^r} = |F_{hk}|^2 \frac{\lambda q_{hk}^z}{2\pi} \frac{1}{2\pi q_{hk}^r} = |F_{hk}|^2 \frac{2\theta_{hk}}{2\pi q_{hk}^r}, \quad (4.23)$$

where  $2\theta_{hk} = \lambda q_{hk}^z/(2\pi)$  is the incident angle at which the outgoing X-ray for the peak ( $h, k$ ) is blocked by the substrate. Eq. (4.22) and (4.23) relate the form factor calculated from a model to the experimentally observed intensity, and are partially equivalent to Eq. (4.15) and (4.16).

In non-linear least squares fitting procedure, we fitted the observed integrated intensity to the calculated intensity from a bilayer model using these Lorentz corrections. This is because we can determine experimental uncertainties on observed intensity rather than the Lorentz-corrected form factors. We avoid propagating the uncertainties by fitting a model to observed intensity.

#### 4.3.4 Absorption Correction for LAXS

In this section, we derive the absorption correction for an oriented sample. The calculation involves an explicit integration over the incident angle,  $\omega$ , which is necessitated by the sample rotation during an X-ray exposure. The procedure is to write down an absorption factor,  $A(\omega, \theta)$ , for a given scattering angle at a given incident angle,



and then integrate over  $\omega$ . We ignore  $q_x$  dependence because the X-ray path inside the sample is nearly within the  $y$ - $z$  plane for low angle scattering. The correction for wide angle scattering is described in a later section.

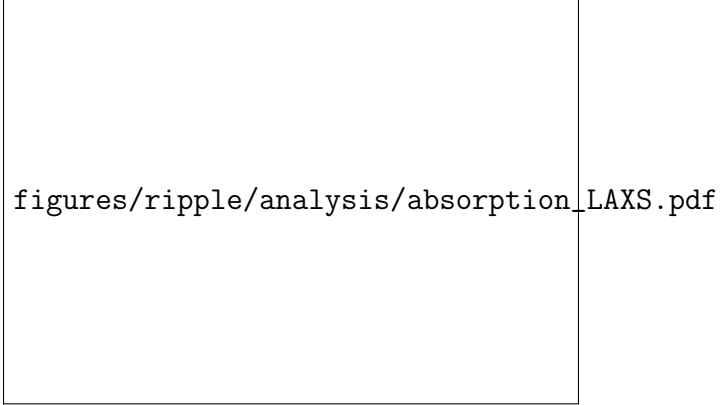


Figure 4.22: The path of X-rays within the sample. The incident angle is  $\omega$  and the total scattering angle is  $2\theta$ . An X-ray with a penetration depth of  $z$  is shown. The total thickness of the sample is  $t$ .

Assume that all the X-rays enter the sample from the top surface. The total scattering angle is given by  $2\theta$  (see Fig. 4.22). Let the  $z$ -axis point downward. At the top surface (air-sample interface),  $z = 0$ . For X-rays that travel to  $z$  and then scatter, the total path length within the sample is

$$L_{\text{tot}}(z, \omega, \theta) = \frac{z}{\sin \omega} + \frac{z}{\sin(2\theta - \omega)} = zg(\omega, \theta), \quad (4.24)$$

where  $g(\omega, \theta) = (\sin \omega)^{-1} + (\sin(2\theta - \omega))^{-1}$ . For each ray, the intensity is attenuated by the sample absorption. If non-attenuated intensity is equal to  $I_0$ , then the attenuated intensity is

$$I(z, \omega, \theta) = I_0 \exp\left(-\frac{L_{\text{tot}}}{\mu}\right), \quad (4.25)$$

where  $\mu$  is the absorption length of an X-ray.  $\mu$  is 2.6 mm for 10.5 keV [87]. The observed intensity of scattering from a sample fixed at an angle  $\omega$  is equal to the

integration of Eq. (4.25) over the total thickness of the sample and given by

$$\begin{aligned} I_{\text{obs}}(\omega, \theta) &= \int_0^t dz I(z, \omega, \theta) = I_0 \int_0^t dz \exp\left(-\frac{g(\omega, \theta)}{\mu} z\right) \\ &= I_0 \mu \frac{1 - \exp\left(-\frac{t}{\mu} g(\omega, \theta)\right)}{g(\omega, \theta)}. \end{aligned} \quad (4.26)$$

Defining the absorption factor at a fixed angle to be  $A(\omega, \theta)$ , the observed intensity can also be written as

$$I_{\text{obs}}(\omega, \theta) = A(\omega, \theta) t I_0, \quad (4.27)$$

where  $tI_0$  is the intensity we would observe for non-absorbed X-rays. Equating Eq. (4.26) and (4.27), we get

$$A(\omega, \theta) = \frac{\mu}{t} \frac{1 - \exp\left(-\frac{t}{\mu} g(\omega, \theta)\right)}{g(\omega, \theta)}. \quad (4.28)$$

If  $\mu$  is taken to infinity (no absorption),  $A(\omega, \theta)$  goes to 1 as expected. The absorption factor  $A_{h0}$  for the  $k = 0$  peaks is given by  $A(\omega = \theta = \theta_B)$ , plotted in Fig. 4.23. As shown, this factor is about 30 % for  $h = 1$  peak, so it is not negligible.

For  $k \neq 0$  side peaks, an integration over the incident angle  $\omega$  is necessary because these peaks are observable at all our experimental incident angles as described in section 4.3.3. The total observed intensity from a rotating sample is simply

$$I_{\text{total}}(\theta) = \int_0^{2\theta} d\omega I_{\text{obs}}(\omega, \theta). \quad (4.29)$$

The upper integration limit is equal to  $2\theta$  because the substrate completely blocks the scattered X-rays above this angle as discussed in section 4.3.3. The total non-attenuated intensity is equal to  $2\theta t I_0$ . We, then, define the absorption factor  $A(\theta)$  to be the ratio of the total observed intensity to the total non-attenuated intensity,

$$A(\theta) \equiv \frac{I_{\text{total}}(\theta)}{2\theta t I_0}. \quad (4.30)$$

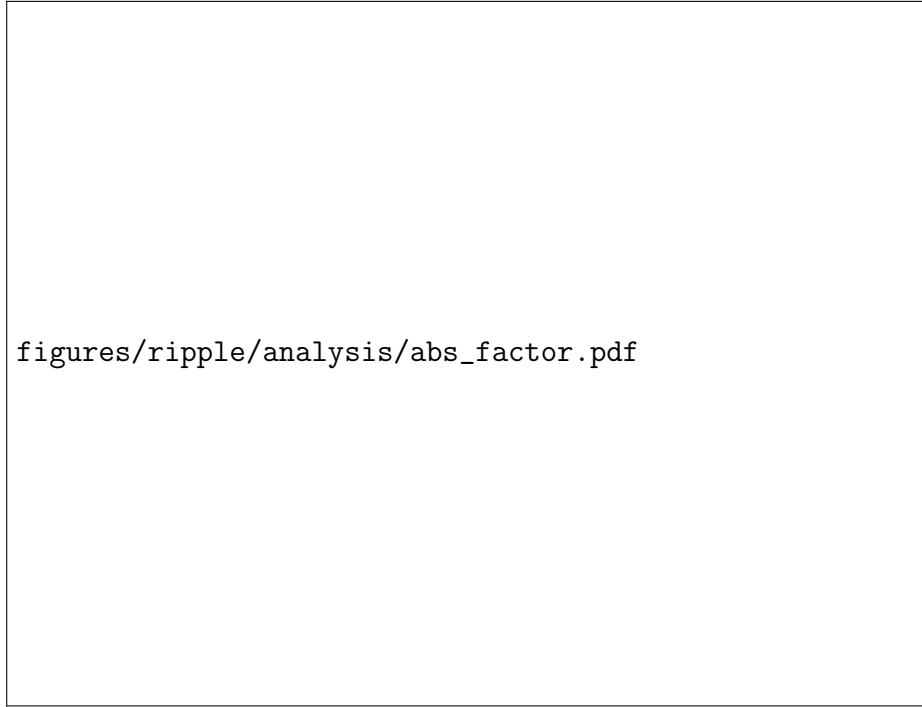


Figure 4.23: Absorption factors as a function of  $q_z \approx 4\pi\theta/\lambda$ . Values at  $q_z = 2\pi h/D$  corresponding to  $D = 57.8 \text{ \AA}$  are shown as squares.  $\mu = 2600 \text{ }\mu\text{m}$ ,  $t = 10 \text{ }\mu\text{m}$ , and  $\lambda = 1.175 \text{ \AA}$ .

Using Eq. (4.28) and (4.29) in (4.30), we arrive at the final absorption factor

$$A(\theta) = \frac{1}{2\theta} \int_0^{2\theta} d\omega A(\omega, \theta) = \frac{\mu}{2\theta t} \int_0^{2\theta} d\omega \frac{1 - \exp\left(-\frac{t}{\mu} g(\omega, \theta)\right)}{g(\omega, \theta)}. \quad (4.31)$$

$A_{hk} = A(\theta)$  is plotted in Fig. 4.23. The absorption correction  $A_c(\theta)$  is the inverse of Eq. (4.31).

### 4.3.5 Correction due to mosaic spread

(Under construction) Integrated intensity needs to be corrected for mosaic spread. During an X-ray exposure, the sample was continuously rotated. Due to this rotation, each pixel integrates intensity over the incident angle  $\omega$ . As described in appendix A.2.2, a rocking scan probes a mosaic spread distribution as a function of  $\omega$ , so integrated intensity observed on a detector is proportional to an integrated mosaic spread distribution. Because the range of the distribution probed is limited by  $\omega = 2\theta_B$ , this range is larger for higher orders. The observed integrated intensity is then larger for higher orders even if the intrinsic relative intensity of different orders is the same. This effect is illustrated in Fig. 4.24.

We limit  $\chi$  to go from  $-1.4^\circ$  to  $1.4^\circ$ . This simplifies a calculation because we can ignore the curvature of the sphere on which the mosaic spread distribution  $P(\alpha)$  is defined as described in Appendix A.2.1. The effect of cutoff on  $\chi$  is not very important because most of observed intensity was included in integration boxes. In contrast, cutoff on  $\omega$  due to substrate blocking the scattering is important, especially for lower  $h$  orders.


We take the distribution to be Lorentzian, which has been experimentally observed.

$$P(\alpha) = \frac{N}{\alpha^2 + \alpha_M^2}, \quad (4.32)$$

where  $N$  is a normalization constant and  $\alpha_M$  is the HWHM of the distribution.  $N$  satisfies

$$N \approx \frac{1}{2\pi} \left( \int_0^{\frac{\pi}{2}} d\alpha \frac{\alpha}{\alpha^2 + \alpha_M^2} \right)^{-1}, \quad (4.33)$$

where a small angle approximation is assumed for  $\alpha$ . We then imagine a two dimensional contour map on a  $\omega\chi$  plane. Observed intensity for a Bragg peak with a Bragg



figures/ripple/analysis/mosaic\_contour.pdf

Figure 4.24: Contours of a mosaic spread distribution projected on the  $xy$ -plane. The distribution function takes a form of Lorentzian centered at  $\alpha = 0$ . Domains with  $\alpha = 0$  are probed at  $\omega = \theta_B$  and  $\chi = 0$ . Integrated intensity of  $(1,0)$  reflection is proportional to the green shaded area while that of  $(3,0)$  reflection is proportional to the blue shaded area, which is three times larger. The rocking scan axis is centered at  $\theta_B$ .

figures/ripple/analysis/mosaic\_correction.pdf

Figure 4.25: Mosaic factor given by Eq. (4.35) as a function of  $q_z \approx 4\pi\theta/\lambda$ . Values at  $q_z = 2\pi h/D$  corresponding to  $D = 57.8 \text{ \AA}$  are shown as squares.  $\alpha_M = 0.05^\circ$  and  $\chi_0 = 1.4^\circ$ .

angle of  $\theta_B$  is given by

$$I_{h0}^{\text{obs}} = \int_{-\theta_B}^{\theta_B} d\omega \int_{-\chi_0}^{\chi_0} d\chi P(\alpha) = \int_{-\theta_B}^{\theta_B} d\omega \int_{-\chi_0}^{\chi_0} d\chi \frac{N}{(\omega - \theta_B)^2 + \chi^2 + \alpha_M^2} \quad (4.34)$$

After  $\chi$  integration, Eq. (4.34) is

$$I_{h0}^{\text{obs}} = 4N \int_0^{\theta_B} \frac{d\omega}{\sqrt{\omega^2 + \alpha_M^2}} \arctan\left(\frac{\chi_0}{\sqrt{\omega^2 + \alpha_M^2}}\right). \quad (4.35)$$

Eq. (4.35) is plotted in Fig. 4.25.

figures/ripple/analysis/21peaks.pdf

## 4.4 LAXS: model

### 4.4.1 Contour Part of the Form Factor


As in Ref. [78], we take the ripple profile to have a sawtooth profile. Its amplitude is  $A$  and the projection of the major arm on the ripple direction is  $x_M$  as shown in Fig. 4.1. Then, we write the ripple profile as

$$u(x) = \begin{cases} -\frac{A}{\lambda_r - x_0} \left(x + \frac{\lambda_r}{2}\right) & \text{for } -\frac{\lambda_r}{2} \leq x < -\frac{x_0}{2}, \\ \frac{A}{x_0} x & \text{for } -\frac{x_0}{2} \leq x \leq \frac{x_0}{2}, \\ -\frac{A}{\lambda_r - x_0} \left(x - \frac{\lambda_r}{2}\right) & \text{for } \frac{x_0}{2} < x \leq \frac{\lambda_r}{2}. \end{cases} \quad (4.36)$$

The ripple profile has inversion symmetry, so that the resulting form factor is real.  $A$  and  $x_M$  are fitting parameters that depend on the integrated intensity of each peak while  $D$ ,  $\lambda_r$ , and  $\gamma$  are determined from measuring the positions of the Bragg peaks.

In order to allow the electron density along the ripple direction to modulate, we include two additional parameters, one to allow for the electron density across the minor side to be different by a ratio  $f_1$  from the electron density across the major side and a second parameter  $f_2$ , which is multiplied by  $\delta$  functions  $\delta(x \pm x_M/2)$  to allow for a different electron density near the kink between the major and the minor sides.

The contour part of the form factor  $F_C$  calculated from Eq. (4.36) is plotted in Fig. (4.26).



figures/ripple/model/F\_contour.pdf

Figure 4.26: Not sure if this plot is useful.



## 4.4.2 Transbilayer Part of the Form Factor

### Delta function model

Delta function model is described here.

### 1G and 2G hybrid model

In the hybrid model, the terminal methyl region of the bilayer is represented as a Gaussian function [88]. The headgroups are represented by one and two Gaussian functions in 1G and 2G hybrid model, respectively. The methylene and water regions are each treated as a constant. The gap between the two constants is represented by a sine function. Then, for half of the bilayer,  $0 \leq z \leq D/2$ , the electron density has the form,

$$\rho(z) = \rho_G(z) + \rho_S(z) + \rho_B(z), \quad (4.37)$$

where the Gaussian part is given by

$$\rho_G(z) = \sum_{i=1}^{1 \text{ or } 2} \rho_{Hi} e^{-(z-Z_{Hi})^2/(2\sigma_{Hi}^2)} + \rho_M e^{-z^2/(2\sigma_M^2)}, \quad (4.38)$$

the strip part is given by

$$\rho_S(z) = \begin{cases} \rho_{CH_2} & \text{for } 0 \leq z < Z_{CH_2}, \\ \rho_W & \text{for } Z_W \leq z \leq D/2, \end{cases} \quad (4.39)$$

and the bridging part is given by

$$\rho_B(z) = \frac{\rho_W - \rho_{CH_2}}{2} \cos \left[ \frac{-\pi}{\Delta Z_H} (z - Z_W) \right] + \frac{\rho_W + \rho_{CH_2}}{2} \quad \text{for } Z_{CH_2} < z < Z_W. \quad (4.40)$$

with  $\Delta Z_H = Z_W - Z_{CH_2}$ . Here, we assume  $Z_{H2} > Z_{H1}$ . Table 4.2 shows some of the definitions.

	1G	2G
$Z_{CH_2}$	$Z_{H1} - \sigma_{H1}$	$Z_{H1} - \sigma_{H1}$
$Z_W$	$Z_{H1} + \sigma_{H1}$	$Z_{H2} + \sigma_{H2}$

Table 4.2: Definitions of  $Z_{CH_2}$  and  $Z_W$

The transbilayer profile along  $x = -z \tan \psi$  can be obtained by rotating the

coordinates  $x$  and  $z$  by  $\psi$  in the clockwise direction and reexpressing  $\rho(z)$  in terms of the rotated coordinates. This leads to replacing  $x$  with  $x' = x \cos \psi + z \sin \psi$  and  $z$  with  $z' = -x \sin \psi + z \cos \psi$ . Then, the rotated transbilayer profile is

$$\rho(x, z) = \delta(x + z \tan \psi) [\rho_G(z') + \rho_S(z') + \rho_B(z')]. \quad (4.41)$$

Taking the two dimensional Fourier transform of Eq. (4.41) leads to the transbilayer part of the form factor,

$$F_T = \int_{-\frac{D}{2}}^{\frac{D}{2}} \int_{-\frac{\lambda_r}{2}}^{\frac{\lambda_r}{2}} [\rho(x, z) - \rho_W] e^{i(q_x x + q_z z)} dx dz \quad (4.42)$$

$$= F_G + F_S + F_B. \quad (4.43)$$

The form factor is calculated in the minus fluid convention, where the bilayer electron density is measured with respect to the electron density of the surrounding solvent. The expression for  $F_T$  is rather messy, so the derivation and full expression are in the appendix. Here, we note that the fitting parameters in this model are  $Z_{Hi}$ ,  $\sigma_{Hi}$ , and  $R_{HiM}$  for each of the two headgroup Gaussian functions,  $\sigma_M$  for the terminal methyl Gaussian,  $\Delta R$  for the methylene region,  $\psi$  for the lipid tilt, and an overall scaling factor. The contour part of the form factor has four more parameters ( $A$ ,  $x_M$ ,  $f_1$ , and  $f_2$ ). In total, the modified 2G hybrid model implements 14 structural parameters.

## 4.5 LAXS: results

### 4.5.1 Data and Electron Density Profile

Table 4.3 and 4.4 summarize observed intensity from data shown in Fig. 4.5.  $q_z$  values for observed peaks were corrected for index of refraction (Appendix B.4). We measured scattering on oriented samples in almost identical conditions as the best unoriented sample of Wack and Webb. As discussed earlier, these two types of samples have different Lorentz corrections, so this allowed us to check our data obtained on oriented samples against an unoriented sample. As Table 4.3 shows, agreement between our oriented data and the unoriented data was good, but integrated intensity from our oriented sample was in many cases larger than that from an unoriented sample. We attribute this discrepancy to the way intensity was extracted. In an

X-ray data from an oriented sample, each peak was nicely separated, so integrating a peak intensity was rather trivial. In contrast, some reflections in unoriented data were overlapping with each other (three pairs of overlapping peaks are highlighted in Table 4.3), making separation of intensity difficult. If the (1, 0) peak in the unoriented data were overestimated, that would account for the observed discrepancy. Indeed, the microdensitometer trace in [76] suggests that the (1, 0) and (1, 1) reflections should have similar intensity.

$h$	$k$	$q_z$ ( $\text{\AA}^{-1}$ )	$q_r$ ( $\text{\AA}^{-1}$ )	$I_{hk}^{\text{obs}}$	box size (pixels)	$h$	$k$	$q^*$ ( $\text{\AA}^{-1}$ )	oriented $ F_{hk} $	unoriented $ F_{hk} ^*$
1	-1	0.102	-0.043	726	$10 \times 7$	1	-1	0.111	83.0	60.8
1	0	0.109	0.000	180818	$10 \times 7$	1	0	0.108	100.0	100.0
1	1	0.114	0.043	241	$10 \times 7$	1	1	0.123	44.0	26.9
1	3	0.128	0.130	4.8	$10 \times 7$	1	3	0.185	9.9	7.6
2	-2	0.206	-0.087	51.4	$10 \times 7$	2	-2	0.224	19.4	15.1
2	-1	0.212	0.044	1818	$10 \times 7$	2	-1	0.215	80.2	71.2
2	0	0.218	0.000	10200	$10 \times 7$	2	0	0.217	30.8	39.7
2	1	0.224	0.043	558	$10 \times 7$	2	1	0.228	42.4	33.9
2	2	0.231	0.086	116	$10 \times 7$	2	2	0.246	26.8	22.7
2	3	0.23	0.129	27	$10 \times 7$	2	3	0.271	15.6	14.2
2	4	0.243	0.173	7.6	$10 \times 7$	2	4	0.301	9.5	7.8
2	5	0.250	0.214	2.9	$10 \times 7$	2	5	0.329	6.4	
3	-2	0.314	-0.087	305	$15 \times 7$	3	-2	0.325	36.2	29.3
3	-1	0.321	-0.043	1205	$15 \times 7$	3	-1	0.322	50.0	44.2
3	0	0.326	0.000	1566	$15 \times 7$	3	0	0.325	14.4	12.0
3	1	0.333	0.043	31.7	$15 \times 7$	3	1		7.9	
3	2	0.339	0.086	32.4	$15 \times 7$	3	2	0.350	11.2	10.5
3	3	0.345	0.129	38.2	$15 \times 7$	3	3	0.370	14.8	14.9
3	4	0.352	0.172	26.1	$15 \times 7$	3	4	0.394	13.9	10.0
3	5	0.358	0.215	8.6	$15 \times 7$	3	5		8.8	

Table 4.3: Observed intensity for  $h = 1$  to 3 at  $D = 57.8$ ,  $\lambda_r = 145$ , and  $\gamma = 98.2^\circ$ . \*Unoriented data are from Wack and Webb [76].

Show in a table, fitting results. Show an edp. Show the thicknesses of both arms. Comment on some fine features.

$h$	$k$	$q_z$ ( $\text{\AA}^{-1}$ )	$q_r$ ( $\text{\AA}^{-1}$ )	$I_{hk}^{\text{obs}}$	box size (pixels)	$h$	$k$	oriented $ F_{hk} $
4	-3	0.417	-0.131	143	20 by 8	4	-3	25.7
4	-2	0.423	-0.087	730	20 by 8	4	-2	46.8
4	-1	0.429	-0.043	415	20 by 8	4	-1	24.7
4	0	0.435	0.000	1938	20 by 8	4	0	18.1
4	1			51.5	20 by 8	4	1	8.5
4	2	0.448	0.085	39	20 by 8	4	2	10.4
4	3			weak		4	3	
4	4	0.461	0.173	2.1	20 by 8	4	4	3.4
4	5	0.467	0.215	3.2	20 by 8	4	5	4.6
4	6	0.473	0.259	1.0	20 by 8	4	6	2.8
5	-3	0.525	-0.132	84.4	25 by 9	5	-3	17.3
5	-2	0.532	-0.087	146	25 by 9	5	-2	18.4
5	-1	0.538	-0.042	64.6	25 by 9	5	-1	8.5
5	0	0.544	0.000	259	25 by 9	5	0	7.3
5	1	0.550	0.040	50.2	25 by 9	5	1	7.2
6	-4	0.628	-0.175	10.3	30 by 10	6	-4	6.3
6	-3	0.635	-0.131	13.8	30 by 10	6	-3	6.3
6	-2	0.641	-0.085	9.7	30 by 10	6	-2	4.2
6	-1	0.647	-0.043	2.0	30 by 10	6	-1	0.0
6	0	0.653	0.000	69.0	30 by 10	6	0	4.1
6	1	0.659	0.043	2.5	30 by 10	6	1	0.0
6	2			weak		6	2	weak
6	3	0.672	0.128	42	30 by 10	6	3	10.5
6	4	0.679	0.170	40	30 by 10	6	4	11.7
7	-4	0.737	-0.174	42	35 by 10	7	-4	11.6
7	-3	0.743	-0.130	40	35 by 10	7	-3	9.7
7	-2	0.749	-0.085	15	35 by 10	7	-2	4.8
7	-1	0.755	-0.042	27	35 by 10	7	-1	4.5
7	0	0.760	0.000	41	35 by 10	7	0	3.4
9	-5			weak		9	-5	
9	-4	0.951	-0.174	19	35 by 10	9	-4	
9	-3			weak		9	-3	
9	-2	0.963	-0.085	21.0	35 by 10	9	-2	
9	-1			weak		9	-1	
9	0	0.974	0.000	21.0	35 by 10	9	0	

Table 4.4: Observed intensity for  $h = 4$  to  $9$  at  $D = 57.8$ ,  $\lambda_r = 145$ , and  $\gamma = 98.2^\circ$  (continued from Table 4.3).

## 4.6 NGIWAXS: analysis

### 4.6.1 Absorption Correction

(Under construction)

## 4.7 NGIWAXS: model

### 4.7.1 Thin rod model

## 4.8 NGIWAXS: results

Figure 4.27 shows near grazing incidence Wide Angle X-ray scattering (NGIWAXS) from an oriented DMPC film in the ripple phase. As can be seen, hydrocarbon chain scattering did not vary considerably between the two  $D$ -spacings. A weak feature that looks like an arc coming from the chain peak was observed. This feature extended out from  $\phi = 0^\circ$  to at least  $70^\circ$ . This feature might simply be mosaic spread scattering due to the peak near the equator. Because mosaic spread of this sample was very small, it may also be possible that the feature is not mosaic spread arc, but comes from the minor arm, indicating that tilt modulation may occur in the minor arm. Chains are packed quite tightly, unlike in the fluid phase. (I did rocking scan, so show the data, and maybe estimate what scattering would look like based on Lorentzian distribution.)

Figure 4.28 shows an enlarged image of the ripple phase WAXS at  $D = 60.8$  Å. We observed a strong peak off the equator and a weak one, the center of which was not determined. The maximum intensity of the strong peak was at  $(q_r, q_z) \approx (1.49 \text{Å}^{-1}, 0.19 \text{Å}^{-1})$  as shown in Fig. 4.29. The weak peak was observed near the equator, but separation of this peak from the strong one was most visible at  $q_z = 0.13 \text{Å}^{-1}$  as Fig. 4.29 shows. Separation of the two peaks was possible because of the high resolution experiment. In previous runs with the low resolution setup, the ripple peak appeared as a single wide peak.

(some thought) Can we say that the observed arc like scattering is not the mosaic spread, but true sample scattering? Comment on the widths of the peaks observed. Possibly make use of both low and high resolution data. Apply the absorption correction. Show  $q$  swaths for various  $\phi$ .

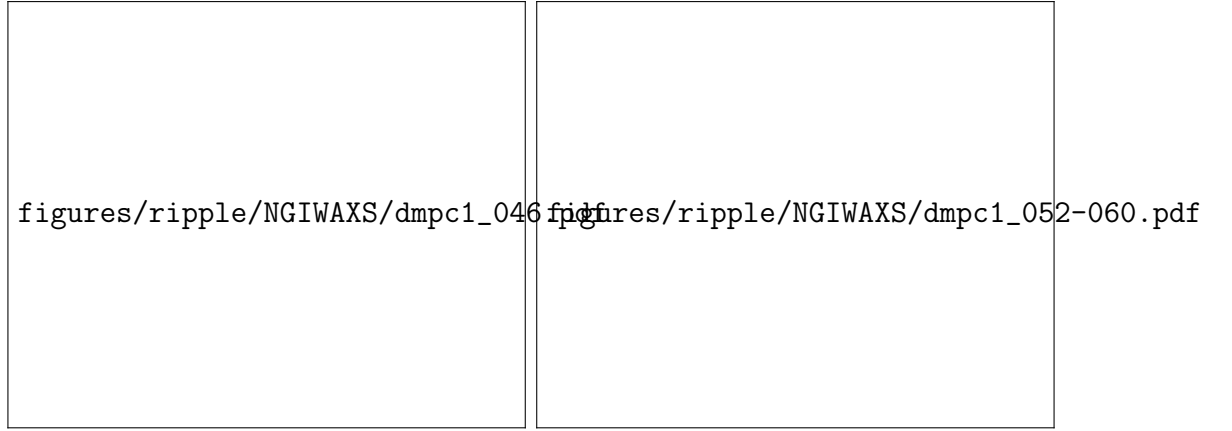


Figure 4.27: NGIWAXS of the DMPC ripple phase for  $D = 59.2 \text{ \AA}$  (left) and  $60.8 \text{ \AA}$  (right). The angle of incidence  $\omega$  was  $0.2^\circ$ . The black regions around the edge of each image are the  $q$ -space that was not probed. The distorted, non rectangular shape of the probed  $q$ -space signifies non-linear relation between the CCD space and sample  $q$ -space.

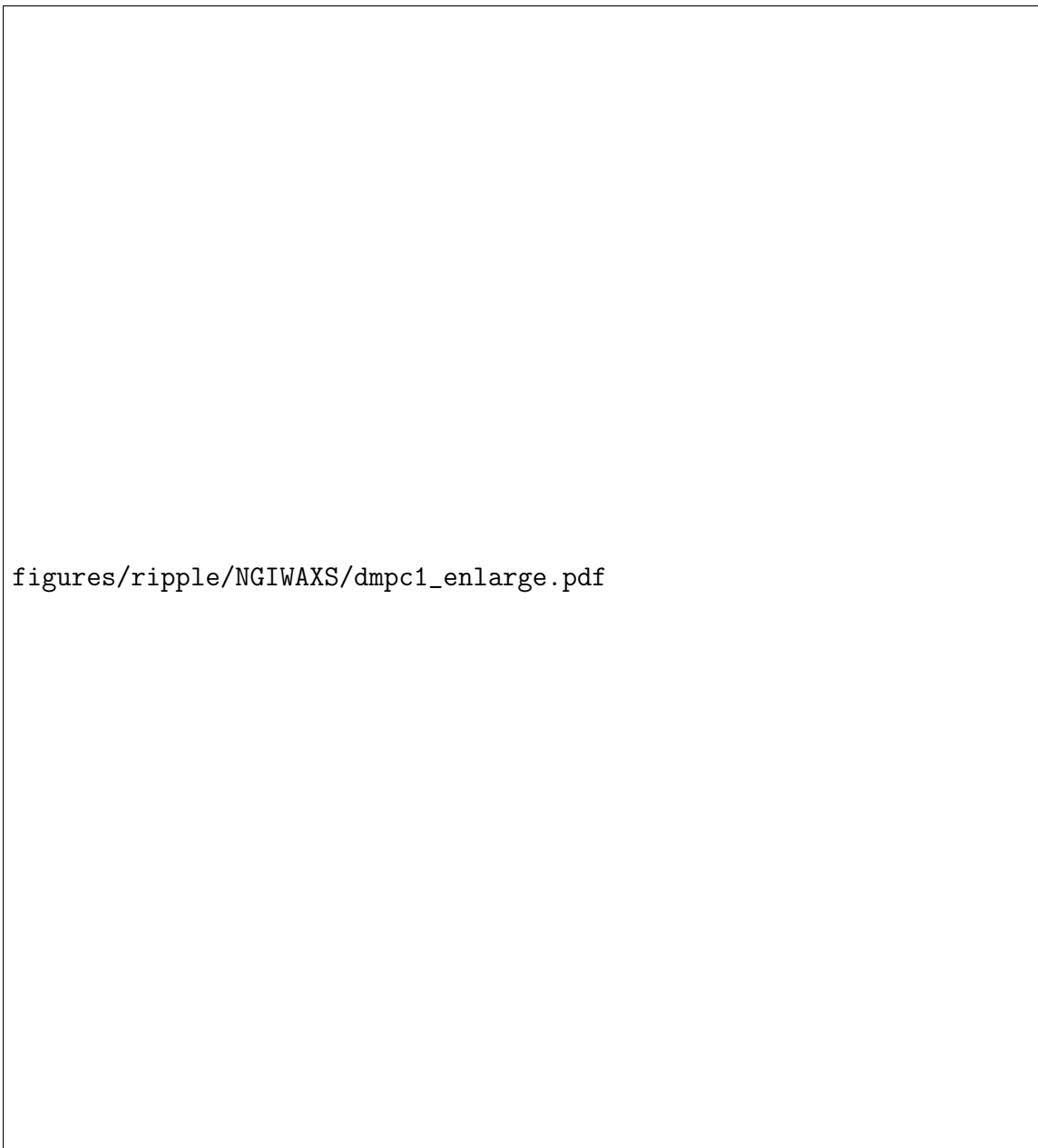


Figure 4.28: Enlarged view of the right image in Fig. 4.27. To show smaller features around the peak, a different contrast is used.

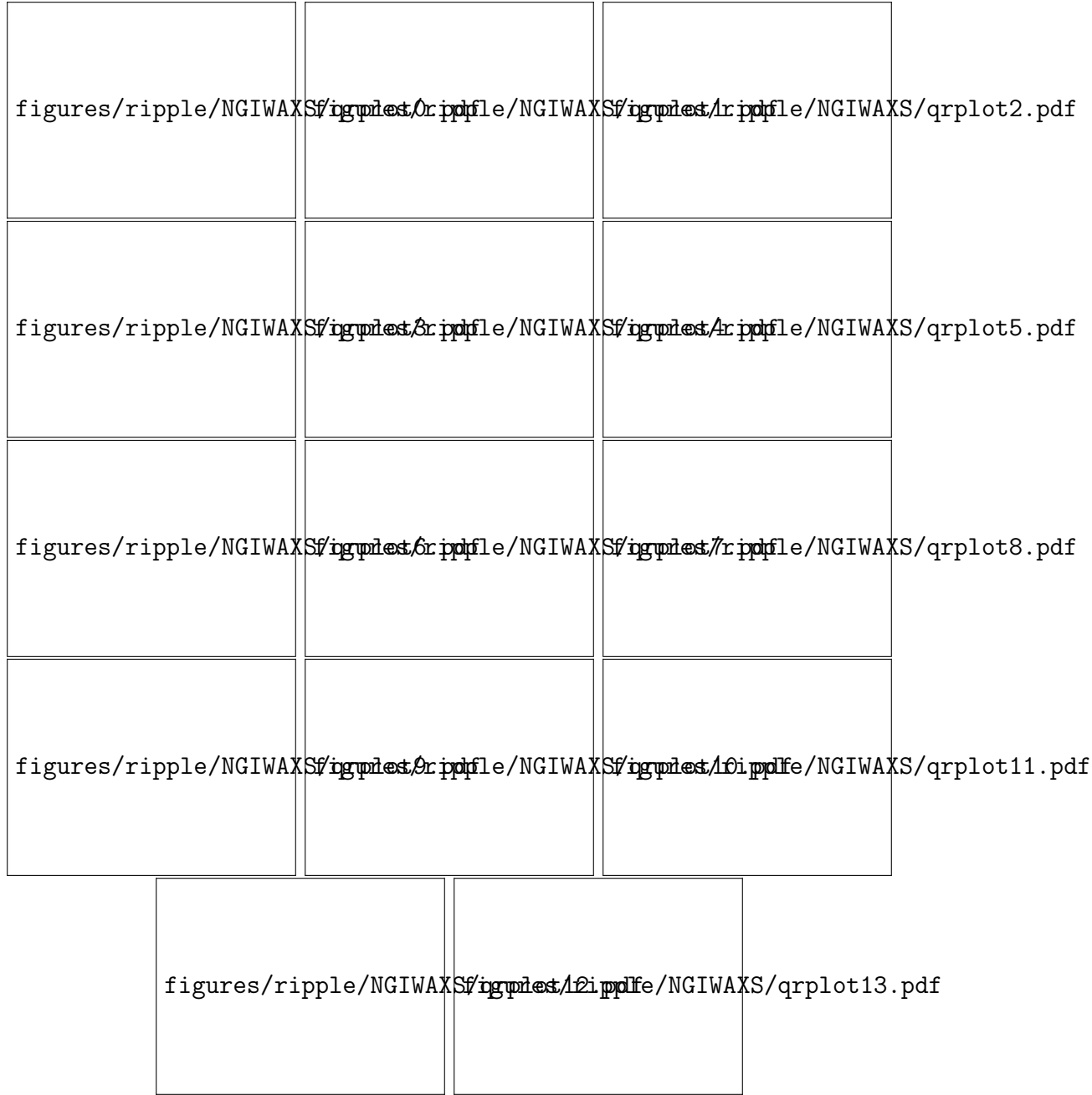


Figure 4.29:  $q_r$  swaths, each averaged over  $0.02 \text{ \AA}^{-1}$ . The center  $q_z$  value of a swath is shown in the figure legends.



## 4.9 TWAXS: results

Convert the image to  $q$ -space. No strong order on the equator. Compare to NGI-WAXS and comment on the absorption effect in NGIWAXS data.

## 4.10 Discussion

Comparison with previous unoriented/oriented stuff.

## 4.11 Conclusion

Future possible experiments include the high resolution transmission experiment, where both geometric broadening and energy dispersion are minimized. The expected resolution is the width of the X-ray beam, which is about 3 pixels. This experiment doubles the best resolution achieved in this work. Another slightly different high resolution experiment is to use silicon crystal analyzer downstream of the sample, which completely remove geometric broadening. The downside of this type of high resolution experiment is that only one point in  $q$ -space is probed at any given exposure, so to get a full 2D map of wide angle scattering is time consuming.

# Appendices

# Appendix A

## Tat

### A.1 Analysis of Fixed Angle Data using NFIT

In this section, I propose a slightly new method to analyze the diffuse scattering data. This method may ease measurement of the X-ray form factor at lower  $q_z$  ( $\leq 0.25 \text{ \AA}^{-1}$ ).

#### A.1.1 Theory

#### A.1.2 Results

### A.2 Mosaic Spread for NFIT analysis

First we describe an analysis of mosaic spread for diffuse scattering. Next we discuss some experimental methods. Third, we discuss the updated NFIT program. Fourth, we show the results.

#### A.2.1 Mosaic Spread: Calculation

In this section, an analytical framework for dealing with mosaic spread is developed. A sample of oriented stacks of bilayers consists of many small domains, within which layers are registered in an array. An ideal domain is a domain where the layers are parallel to the substrate, whose surface is in the sample  $xy$ -plane, so the orientation  $\mathbf{n}$  of an ideal domain is perpendicular to the substrate as shown in Fig. A.1. In general, the orientation  $\mathbf{n}'$  of a domain is tilted from that of an ideal domain by some angle  $\alpha$ . Then, we consider a mosaic spread distribution function,  $P(\alpha)$ , representing a

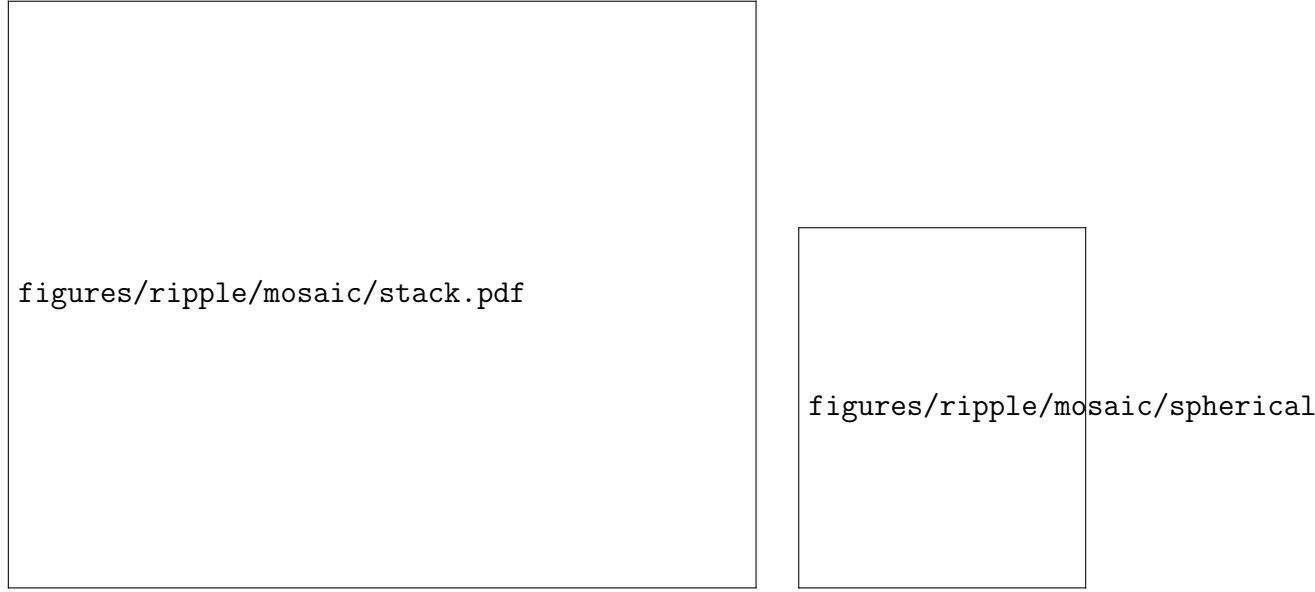


Figure A.1: Two dimensional view of mosaic spread (left) and notations used in this section (right). The stacking direction of an ideal domain is  $\mathbf{n}$  and that of a tilted domain  $\mathbf{n}'$ . The deviation of  $\mathbf{n}'$  from  $\mathbf{n}$  denoted as  $\alpha$  quantifies the degree of misorientation of a domain. The  $x$ ,  $y$ , and  $z$ -axes are the sample coordinates.

probability of finding a domain with a tilt  $\alpha$ . We assume that the sample is symmetric about the substrate normal, so that the distribution  $P(\alpha)$  does not depend on the azimuthal angle,  $\beta$ . The normalization condition on  $P(\alpha)$  is

$$1 = \int_0^{2\pi} d\beta \int_0^{\frac{\pi}{2}} d\alpha \sin \alpha P(\alpha). \quad (\text{A.1})$$

The object of this section is to derive the X-ray scattering structure factor including the distribution function  $P(\alpha)$ .

First, let us consider a two dimensional example. Our sample consists of two identical domains except a tilt  $\alpha$  shown in Fig. A.2. Then, the sample structure factor  $S^{\text{sam}}(\mathbf{q})$  is a superposition of the structure factor  $S(\mathbf{q})$  of the ideal domain and  $S(\mathbf{q}')$  of the tilted domain,

$$S^{\text{sam}}(\mathbf{q}) = S(q_x, q_z) + S(q'_x, q'_z). \quad (\text{A.2})$$

To express  $S(q'_x, q'_z)$  in terms of the sample  $q$ -space  $(q_x, q_z)$ , we write  $q'_x$  and  $q'_z$  in

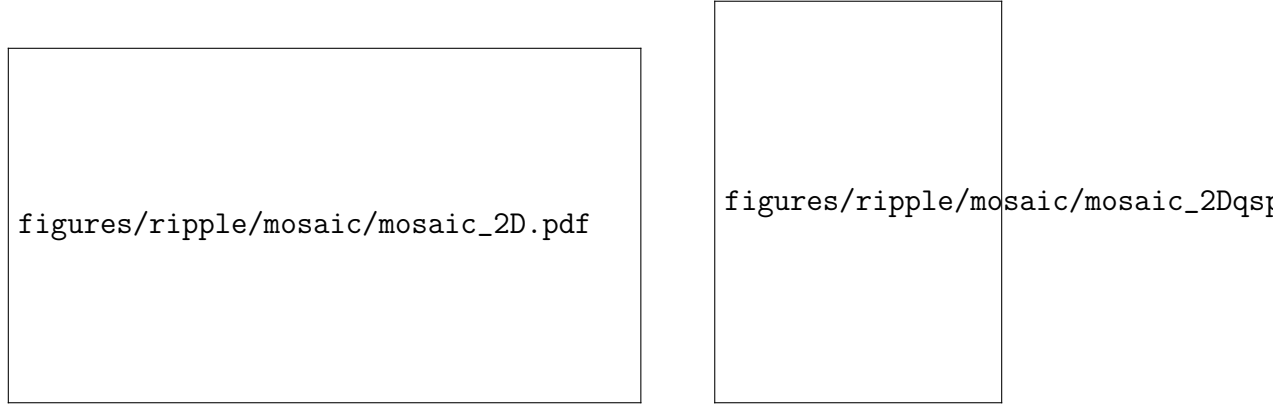


Figure A.2: Example of a two dimensional sample consisting of an ideal and tilted domains.  $\mathbf{q} = (q_x, q_z)$  is the sample  $q$ -space and  $\mathbf{q}' = (q'_x, q'_z)$  is the domain  $q$ -space. The two  $q$ -spaces are related by a rotation of  $\alpha$  about the  $y$ -axis, which is into the page.

terms of  $q_x$ ,  $q_z$ , and  $\alpha$ ,

$$\begin{aligned}
 q'_x &= \mathbf{q} \cdot \hat{\mathbf{x}}' = q \cos\left(\frac{\pi}{2} - \theta + \alpha\right) \\
 q'_z &= \mathbf{q} \cdot \hat{\mathbf{z}}' = q \sin\left(\frac{\pi}{2} - \theta + \alpha\right) \\
 q_x &= q \cos(\pi/2 - \theta) \\
 q_z &= q \sin(\pi/2 - \theta)
 \end{aligned} \tag{A.3}$$

where  $q = |\mathbf{q}|$ . Eq. (A.2) and (A.3) give the structure factor of a sample consisting of the two domains. With a continuous distribution of  $\mathbf{n}'$ , we integrate over the angle  $\alpha$  with each structure factor modulated by the distribution function  $P(\alpha)$ ,

$$S_M(\mathbf{q}) = S_M(q, \theta) = \int_{-\pi/2}^{\pi/2} d\alpha S(q'_x, q'_z) P(\alpha), \tag{A.4}$$

Variables  $q$  and  $\theta$  are used in the above equation to make a connection with the three dimensional case, where the spherical coordinates are convenient, which we discuss now.

For a three dimensional sample, the basic idea is the same as the two dimensional case. In the three dimensional case, we also rotate the vector  $\mathbf{n}'$  about the  $z$ -axis by an angle  $\beta$  after the rotation about the  $y$ -axis by an angle  $\alpha$ , so all we need to do is to apply appropriate rotation matrices to the sample  $xyz$ -axes which define the domain

coordinates  $x'y'z'$ .

The rotation matrix for rotating a vector about the  $y$ -axis is given by

$$R_y = \begin{pmatrix} \cos \alpha & 0 & \sin \alpha \\ 0 & 1 & 0 \\ -\sin \alpha & 0 & \cos \alpha \end{pmatrix} \quad (\text{A.5})$$

and for rotating about the  $z$ -axis

$$R_z = \begin{pmatrix} \cos \beta & -\sin \beta & 0 \\ \sin \beta & \cos \beta & 0 \\ 0 & 0 & 1 \end{pmatrix}. \quad (\text{A.6})$$

Then, what we want is

$$\hat{\mathbf{x}}' = R_z R_y \begin{pmatrix} 1 \\ 0 \\ 0 \end{pmatrix} = \begin{pmatrix} \cos \alpha \cos \beta \\ \cos \alpha \sin \beta \\ -\sin \alpha \end{pmatrix} \quad (\text{A.7})$$

$$\hat{\mathbf{y}}' = R_z R_y \begin{pmatrix} 0 \\ 1 \\ 0 \end{pmatrix} = \begin{pmatrix} -\sin \beta \\ \cos \beta \\ 0 \end{pmatrix} \quad (\text{A.8})$$

$$\hat{\mathbf{z}}' = R_z R_y \begin{pmatrix} 0 \\ 0 \\ 1 \end{pmatrix} = \begin{pmatrix} \sin \alpha \cos \beta \\ \sin \alpha \sin \beta \\ \cos \alpha \end{pmatrix}. \quad (\text{A.9})$$

The domain  $q$ -space,  $(q'_x, q'_y, q'_z)$ , in terms of the sample  $q$ -space  $(q_x, q_y, q_z)$  is given by

$$q'_x = \mathbf{q} \cdot \hat{\mathbf{x}}' = q_x \cos \alpha \cos \beta + q_y \cos \alpha \sin \beta - q_z \sin \alpha, \quad (\text{A.10})$$

$$q'_y = \mathbf{q} \cdot \hat{\mathbf{y}}' = -q_x \sin \beta + q_y \cos \beta, \quad (\text{A.11})$$

$$q'_z = \mathbf{q} \cdot \hat{\mathbf{z}}' = q_x \sin \alpha \cos \beta + q_y \sin \alpha \sin \beta + q_z \cos \alpha. \quad (\text{A.12})$$

The transformation expressed in the spherical coordinates is

$$\cos \theta' = \frac{q'_z}{q} = \sin \theta \sin \alpha \cos(\phi - \beta) + \cos \theta \cos \alpha, \quad (\text{A.13})$$

$$\tan \phi' = \frac{q'_y}{q'_x} = \frac{\sin \theta \sin(\phi - \beta)}{\sin \theta \cos \alpha \cos(\phi - \beta) - \cos \theta \sin \alpha}. \quad (\text{A.14})$$

Summing over all the domains, we get for the mosaic spread modified structure factor

$$S_M(q, \theta, \phi) = \int_0^{2\pi} d\beta \int_0^{\frac{\pi}{2}} d\alpha S(q, \theta', \phi') P(\alpha) \quad (\text{A.15})$$

with Eq. (A.13) and Eq. (A.14).

The structure factor for a stack of rigid layers with their normals parallel to the  $z$ -axis in spherical coordinates is

$$S(q, \theta, \phi) = \frac{\delta(q - \frac{2\pi h}{D})}{q^2} \delta(\cos \theta - 1) \delta(\phi) \quad (\text{A.16})$$

where  $\delta(x)$  is the Dirac delta function. From Eq. (A.14),  $\delta(\phi')$  is equivalent to  $\delta(\beta - \phi)$ . Setting  $\beta = \phi$  in Eq. (A.13) gives  $\cos \theta' = \cos(\alpha - \theta)$ . Then, the mosaic spread modified structure factor  $S_M(\mathbf{q})$  is

$$\begin{aligned} S_M(q, \theta, \phi) &= \int d\alpha \int d\beta \frac{\delta(q - \frac{2\pi h}{D})}{q^2} \delta(\cos \theta' - 1) \delta(\beta - \phi) P(\alpha) \\ &= \frac{\delta(q - \frac{2\pi h}{D})}{q^2} \int d\alpha \delta(\cos[\alpha - \theta] - 1) P(\alpha) \\ &= \frac{\delta(q - \frac{2\pi h}{D})}{q^2} P(\theta). \end{aligned} \quad (\text{A.17})$$

Eq. (A.17) describes hemispherical shells during a scattering experiment with radii of  $2\pi h/D$  in the sample  $q$ -space. As will be described in the next section, a 2D detector records cross sections of these shells, which give rise to mosaic arcs along  $q = 2\pi h/D$ .

The structure factor of thermally fluctuating layers is not simple delta functions and gives rise to diffuse scattering. Analysis of the diffuse scattering from a sample with mosaic spread requires Eq. (A.15).

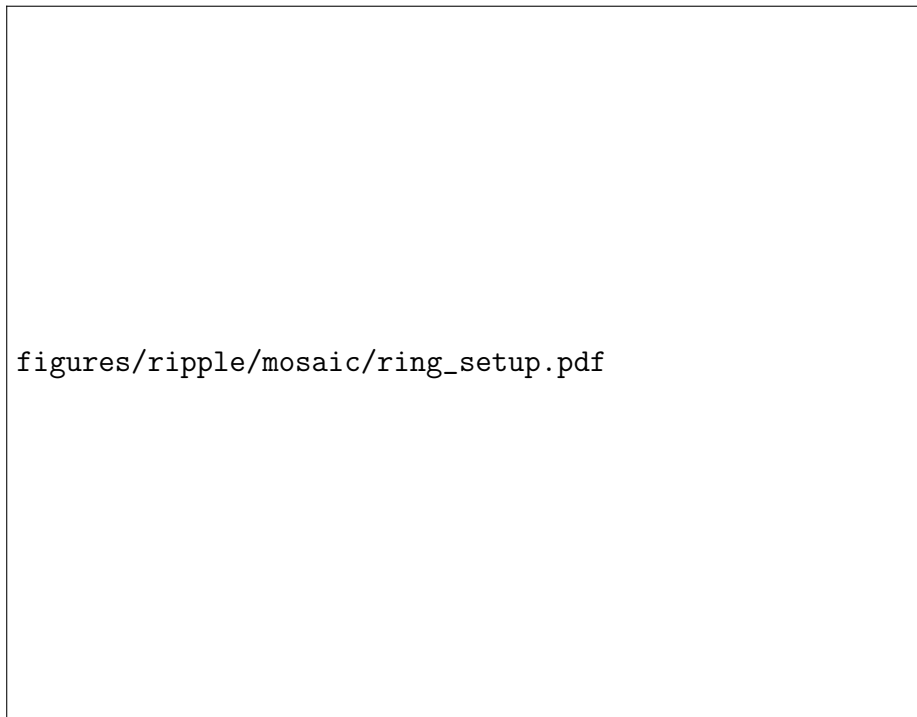


Figure A.3: Notations used in this section. The arc originating from the  $Z$ -axis is the mosaic arc due to the mosaic spread distribution.

### A.2.2 Mosaic Spread: Experiment

In this section, we discuss experimental procedures to probe appropriate  $q$ -space to measure the mosaic spread distribution,  $P(\alpha)$ . In our setup, the angle of incidence between the beam and substrate, denoted by  $\omega$ , can be varied. A conventional method to measure  $P(\alpha)$  is a rocking scan, where one measures the integrated intensity of a given Bragg peak as a function of  $\omega$  with a fixed detector position. Another method that takes an advantage of an area detector [89] measures the intensity as a function of  $\chi$  on a two dimensional detector (see Fig. A.3). This method has been used to quantify complete pole figures for thin films with fiber texture (isotropic in-plane orientation) [90]. First, we want to compare the two methods mentioned above and determine their relationship.





Figure A.4: Rocking scan trace in  $q$ -space.

Eq. (4.12) expressed in terms of the coordinates defined in Fig. A.3 is

$$\begin{aligned}
 q_x &= q \cos \theta \sin \chi \\
 q_y &= q (-\sin \theta \cos \omega + \cos \theta \cos \chi \sin \omega) \\
 q_z &= q (\sin \theta \sin \omega + \cos \theta \cos \chi \cos \omega) .
 \end{aligned}
 \tag{A.18}$$

For a rocking scan focused on a particular order,  $\chi = 0$  and  $\theta = \theta_B$  while  $\omega$  is varied about  $\theta_B$ , where  $\theta_B$  is the Bragg angle. Then,

$$\begin{aligned}
 q_x &= 0 \\
 q_y &= q \sin(\omega - \theta_B) \\
 q_z &= q \cos(\omega - \theta_B),
 \end{aligned}
 \tag{A.19}$$

which shows that this scan traces a part of the circular path in the  $q_x = 0$  plane as shown in Fig. A.4. As Fig. A.4 shows, however, the rocking scan only probes a small fraction of the entire distribution, limited by  $2\theta_B$ . As discussed in section 4.3.3, beyond  $\omega = 2\theta_B$ , the substrate blocks scattering. On the other hand, the ring analysis takes advantage of a two dimensional detector and can probe a substantially wider range of the distribution in principle: approximately  $\pm 45^\circ$  at  $\omega = \theta_B$ . This method is now described.

In the ring method, we set  $\omega = \theta_B$  and scan on the detector along  $\theta = \theta_B$  as a function of  $\chi$ . Then, Eq. (A.18) becomes

$$\begin{aligned} q_x &= q \cos \theta_B \sin \chi \\ q_y &= q \sin \theta_B \cos \theta_B (\cos \chi - 1) \\ q_z &= q(\sin^2 \theta_B + \cos^2 \theta_B \cos \chi), \end{aligned} \tag{A.20}$$

where  $q = 4\pi \sin \theta_B / \lambda$ . For small  $\theta_B$ , Eq. (A.20) reduces to

$$\begin{aligned} q_x &\approx q \sin \chi \\ q_y &\approx 0 \\ q_z &\approx q \cos \chi. \end{aligned} \tag{A.21}$$

Thus, by comparing Eq. (A.19) and Eq. (A.21), the rocking scan and ring analysis have been shown to be equivalent for small  $\theta_B$ , the condition which is satisfied for low angle X-ray scattering.

### A.2.3 NFIT

The updated NFIT first calculates a theoretical structure factor in cylindrical coordinates [37]. This calculated structure factor  $S(q_r, q_z)$  has rotational symmetry about the  $z$ -axis, which eliminates the  $\phi'$  dependence in Eq. (A.15). The program interpolates  $S(q_r, q_z)$  in terms of the spherical coordinates  $q$  and  $\theta$  with  $\phi = 0$  to perform the double integration in Eq. (A.15). After the mosaic spread integration, the program performs the  $q_y$  integration described in section 3.2.2. For this integration, the calculated  $S_M$  is interpolated in terms of  $q_x$ ,  $q_y$ , and  $q_z$ .

If the structure factor defined in the Cartesian coordinates are desired (for a case of square domains instead of circular ones), Eq. (A.10 – A.12) can be used instead of Eq. (A.13) and (A.14).

An issue with the current analysis comes from the form factor  $|F(q_z)|$ , which is not calculated from a model in NFIT. Because the mosaic spread integration mixes up intensity at different  $q_z$  values, the separation of  $|F(q_z)|$  from  $S(\mathbf{q})$  is in principle impossible. One way to deal with this issue is to combine the SDP and NFIT programs, but that will end up with too many non-linear parameters. Another pos-

sibility is to limit the fitting range to regions close to the meridian and truncate the distribution at an angle much smaller than  $\pi/2$ . For a small range of integration, it is not unreasonable to assume that the form factor is approximately constant as can be seen from Eq. (A.12) with small  $q_x$ ,  $q_y$ , and  $\alpha$ . Therefore, the analysis developed in this appendix ignores the form factor.

#### **A.2.4 Results**

### **A.3 Some More Details of Tat Stuff if needed**

# Appendix B

## Ripple Phase

### B.1 Derivation of the contour part of the form factor

In this section, we derive  $F_C$ . The ripple profile,  $u(x)$  is given by

$$u(x) = \begin{cases} -\frac{A}{\lambda_r - x_0} \left(x + \frac{\lambda_r}{2}\right) & \text{for } -\frac{\lambda_r}{2} \leq x < -\frac{x_0}{2} \\ \frac{A}{x_0} x & \text{for } -\frac{x_0}{2} \leq x \leq \frac{x_0}{2} \\ -\frac{A}{\lambda_r - x_0} \left(x - \frac{\lambda_r}{2}\right) & \text{for } \frac{x_0}{2} < x \leq \frac{\lambda_r}{2} \end{cases} \quad (\text{B.1})$$

The contour part of the form factor is the Fourier transform of the contour function,  $C(x, z)$ ,

$$F_C(\mathbf{q}) = \frac{1}{\lambda_r} \int_{-\frac{\lambda_r}{2}}^{\frac{\lambda_r}{2}} dx \int_{-\frac{D}{2}}^{\frac{D}{2}} dz C(x, z) e^{iq_z z} e^{iq_x x}$$

As discussed in section X, the modulated models allow the electron density to modulate along the ripple direction,  $x$ . This means

$$C(x, z) = \begin{cases} f_1 \delta[z - u(x)] & \text{for } -\frac{\lambda_r}{2} \leq x < -\frac{x_0}{2} \\ \delta[z - u(x)] & \text{for } -\frac{x_0}{2} < x < \frac{x_0}{2} \\ f_1 \delta[z - u(x)] & \text{for } \frac{x_0}{2} \leq x < \frac{\lambda_r}{2} \end{cases} + f_2 \delta\left(x + \frac{x_0}{2}\right) \delta\left(z + \frac{A}{2}\right) + f_2 \delta\left(x - \frac{x_0}{2}\right) \delta\left(z - \frac{A}{2}\right). \quad (\text{B.2})$$

The contribution from the minor arm is

$$\begin{aligned}
& \frac{1}{\lambda_r} \int_{-\frac{\lambda_r}{2}}^{-\frac{x_0}{2}} dx e^{iq_x x} e^{iq_z u(x)} + \int_{\frac{x_0}{2}}^{\frac{\lambda_r}{2}} dx e^{iq_x x} e^{iq_z u(x)} \\
&= \frac{1}{\lambda_r} \int_{\frac{x_0}{2}}^{\frac{\lambda_r}{2}} dx e^{-i[q_x x - q_z \frac{A}{\lambda_r - x_0}(x - \frac{\lambda_r}{2})]} + \int_{\frac{x_0}{2}}^{\frac{\lambda_r}{2}} dx e^{i[q_x x - q_z \frac{A}{\lambda_r - x_0}(x - \frac{\lambda_r}{2})]} \\
&= \frac{2}{\lambda_r} \int_{\frac{x_0}{2}}^{\frac{\lambda_r}{2}} \cos \left[ \left( q_x - q_z \frac{A}{\lambda_r - x_0} \right) x + q_z \frac{A}{\lambda_r - x_0} \frac{\lambda_r}{2} \right] dx
\end{aligned} \tag{B.3}$$

Using a trigonometric identity,

$$\sin u - \sin v = 2 \cos[(u + v)/2] \sin[(u - v)/2],$$

and defining

$$\omega(\mathbf{q}) = \frac{1}{2} (q_x x_0 + q_z A), \tag{B.4}$$

we further simplify Eq. (B.3),

$$\begin{aligned}
&= \frac{2}{\lambda_r} \frac{\lambda_r - x_0}{\frac{1}{2} q_x \lambda_r - \omega} \cos \left[ \frac{1}{2} \left( \frac{1}{2} q_x \lambda_r + \omega \right) \right] \sin \left[ \frac{1}{2} \left( \frac{1}{2} q_x \lambda_r - \omega \right) \right] \\
&= \frac{1}{\lambda_r} \frac{\lambda_r - x_0}{\frac{1}{2} q_x \lambda_r - \omega} \cos \left[ \frac{1}{2} \left( \frac{1}{2} q_x \lambda_r + \omega \right) \right] \frac{\sin \left( \frac{1}{2} q_x \lambda_r - \omega \right)}{\cos \left[ \frac{1}{2} \left( \frac{1}{2} q_x \lambda_r - \omega \right) \right]} \\
&= \frac{\lambda_r - x_0}{\lambda_r} \frac{\cos \left[ \frac{1}{2} \left( \frac{1}{2} q_x \lambda_r + \omega \right) \right] \sin \left( \frac{1}{2} q_x \lambda_r - \omega \right)}{\cos \left[ \frac{1}{2} \left( \frac{1}{2} q_x \lambda_r - \omega \right) \right] \frac{1}{2} q_x \lambda_r - \omega}.
\end{aligned} \tag{B.5}$$

Similarly, we calculate the contribution from the major arm,

$$\begin{aligned}
\frac{1}{\lambda_r} \int_{-\frac{x_0}{2}}^{\frac{x_0}{2}} dx e^{i \left( \frac{q_z A}{x_0} + q_x \right) x} &= \frac{2}{\lambda_r} \int_0^{\frac{x_0}{2}} dx \cos \left( \frac{q_z A}{x_0} + q_x \right) x \\
&= \frac{x_0}{\lambda_r} \frac{\sin \omega}{\omega}
\end{aligned} \tag{B.6}$$

The contribution from the kink region is

$$\begin{aligned}
& \frac{1}{\lambda_r} \iint dx dz \left[ \delta \left( x + \frac{x_0}{2} \right) \delta \left( z + \frac{A}{2} \right) + \delta \left( x - \frac{x_0}{2} \right) \delta \left( z - \frac{A}{2} \right) \right] e^{iq_x x} e^{iq_z z} \\
&= \frac{2}{\lambda_r} \cos \omega.
\end{aligned} \tag{B.7}$$

Therefore,

$$F_C(\mathbf{q}) = \frac{x_0}{\lambda_r} \frac{\sin \omega}{\omega} + f_1 \frac{\lambda_r - x_0}{\lambda_r} \frac{\cos \left[ \frac{1}{2} \left( \frac{1}{2} q_x \lambda_r + \omega \right) \right]}{\cos \left[ \frac{1}{2} \left( \frac{1}{2} q_x \lambda_r - \omega \right) \right]} \frac{\sin \left( \frac{1}{2} q_x \lambda_r - \omega \right)}{\frac{1}{2} q_x \lambda_r - \omega} + \frac{2f_2}{\lambda_r} \cos \omega \quad (\text{B.8})$$

## B.2 Rotation of a Two-Dimensional Function

Let us consider rotating a function,  $f(x, z)$  in two dimensions by an angle,  $\psi$ , in the counterclockwise direction (see Fig. X). This is easily achieved by rotating the coordinate system by  $\psi$  in the clockwise direction. Let rotated coordinates be  $x'$  and  $z'$ . A point in the original coordinates,  $(x, z)$ , is written as  $(x', z')$  in the new coordinates. More specifically, the point  $\mathbf{P}$  is written as  $\mathbf{P} = x\hat{\mathbf{x}} + z\hat{\mathbf{z}} = x'\hat{\mathbf{x}}' + z'\hat{\mathbf{z}}'$ .  $\hat{\mathbf{x}}$  and  $\hat{\mathbf{z}}$  in the  $x'z'$  coordinate system are written as

$$\hat{\mathbf{x}} = \cos \psi \hat{\mathbf{x}}' + \sin \psi \hat{\mathbf{z}}' \quad (\text{B.9})$$

$$\hat{\mathbf{z}} = -\sin \psi \hat{\mathbf{x}}' + \cos \psi \hat{\mathbf{z}}'. \quad (\text{B.10})$$

Plugging these in  $\mathbf{P} = x\hat{\mathbf{x}} + z\hat{\mathbf{z}}$  leads to

$$x' = x \cos \psi - z \sin \psi \quad (\text{B.11})$$

$$z' = z \cos \psi + x \sin \psi, \quad (\text{B.12})$$

the inverse of which is

$$x = x' \cos \psi + z' \sin \psi \quad (\text{B.13})$$

$$z = -x' \sin \psi + z' \cos \psi. \quad (\text{B.14})$$

Using the latter equations,  $f(x, z)$  can be expressed in terms of  $x'$  and  $z'$ . The resulting function  $f(x', z')$  is the rotated version of  $f(x, z)$ .

As an example, let us consider a Dirac delta function located at  $(x, z) = (0, Z_H)$ ,

that is,  $f(x, z) = \delta(x)\delta(z - Z_{\text{H}})$ . After the rotation by  $\psi$ , it becomes

$$\begin{aligned}
f(x, z) &\rightarrow \delta(x \cos \psi + z \sin \psi) \delta(-x \sin \psi + z \cos \psi - Z_{\text{H}}) \\
&= \frac{\delta(x + z \tan \psi)}{|\cos \psi|} \frac{\delta(-x \sin \psi \cos \psi + z \cos^2 \psi - Z_{\text{H}} \cos \psi)}{1/|\cos \psi|} \\
&= \delta(x + z \tan \psi) \delta(z \tan \psi \sin \psi \cos \psi + z \cos^2 \psi - Z_{\text{H}} \cos \psi) \\
&= \delta(x + z \tan \psi) \delta(z - Z_{\text{H}} \cos \psi),
\end{aligned}$$

which is a part of the expression for  $T_\psi(x, z)$  in the simple delta function model.

### B.3 Derivation of the transbilayer part of the form factor in the 2G hybrid model

In this section, we derive the trasbilayer part of the form factor calculated from the 2G hybrid model discussed in section X. Defining  $z' = -x \sin \psi + z \cos \psi$ , the Fourier transform of a Gaussian function along the line tilted from  $z$ -axis by  $\psi$  is

$$\begin{aligned}
&\iint dz dx \rho_{\text{Hi}} \exp\left\{-\frac{(z' - Z_{\text{Hi}})^2}{2\sigma_{\text{Hi}}^2}\right\} \delta(x \cos \psi + z \sin \psi) e^{iq_x x} e^{iq_z z} \\
&= \frac{1}{\cos \psi} \int_{-\frac{D}{2}}^{\frac{D}{2}} dz \rho_{\text{Hi}} \exp\left\{-\frac{(z - Z_{\text{Hi}} \cos \psi)^2}{2\sigma_{\text{Hi}}^2 \cos^2 \psi} + i(q_z - q_x \tan \psi)z\right\} \\
&\approx \rho_{\text{Hi}} \sqrt{2\pi} \sigma_{\text{Hi}} \exp\left\{i\alpha Z_{\text{Hi}} - \frac{1}{2}\alpha^2 \sigma_{\text{Hi}}^2\right\}
\end{aligned} \tag{B.15}$$

with  $\alpha = q_z \cos \psi - q_x \sin \psi$ . Using Eq. (B.15) and adding the other side of the bilayer and the terminal methyl term, we get

$$\begin{aligned}
F_{\text{G}} &= \sqrt{2\pi} \left[ -\rho_{\text{M}} \sigma_{\text{M}} \exp\left\{-\frac{1}{2}\alpha^2 \sigma_{\text{M}}^2\right\} \right. \\
&\quad \left. + \sum_{i=1}^{1 \text{ or } 2} 2\rho_{\text{Hi}} \sigma_{\text{Hi}} \cos(\alpha Z_{\text{Hi}}) \exp\left\{-\frac{1}{2}\alpha^2 \sigma_{\text{Hi}}^2\right\} \right]. \tag{B.16}
\end{aligned}$$

The strip part of the model in the minus fluid convention is

$$\rho_S(z) = \begin{cases} -\Delta\rho & \text{for } 0 \leq z < Z_{\text{CH}_2} \cos \psi, \\ 0 & \text{for } Z_W \cos \psi \leq z \leq D/2, \end{cases} \quad (\text{B.17})$$

where  $\Delta\rho = \rho_W - \rho_{\text{CH}_2}$ . Then, the corresponding Fourier transform is

$$\begin{aligned} F_S &= \iint dz dx e^{iq_x x} e^{iq_z z} \rho_S(z) \delta(x \cos \psi + z \sin \psi) \\ &= \frac{2}{\cos \psi} \int_0^{Z_{\text{CH}_2} \cos \psi} dz \cos\left(\frac{\alpha}{\cos \psi} z\right) (-\Delta\rho) \\ &= -2\Delta\rho \frac{\sin(\alpha Z_{\text{CH}_2})}{\alpha}. \end{aligned} \quad (\text{B.18})$$

The bridging part of the model in the minus fluid convention is

$$\rho_B(x, z) = \frac{\Delta\rho}{2} \cos\left[\frac{-\pi}{\Delta Z_H}(z' - Z_W)\right] - \frac{\Delta\rho}{2} \quad (\text{B.19})$$

for  $Z_{\text{CH}_2} \cos \psi < z < Z_W \cos \psi$ , and 0 otherwise. Here,  $\Delta Z_H = Z_W - Z_{\text{CH}_2}$ . Then, for the strip part of the form factor, we have

$$\begin{aligned} F_B &= \iint dz dx e^{iq_x x} e^{iq_z z} \delta(x \cos \psi + z \sin \psi) \rho_B(x, z) \\ &= \frac{\Delta\rho}{\cos \psi} \int_{Z_{\text{CH}_2} \cos \psi}^{Z_W \cos \psi} dz \cos\left(\alpha \frac{z}{\cos \psi}\right) \left\{ \cos\left[-\frac{\pi}{\Delta Z_H} \left(\frac{z}{\cos \psi} - Z_W\right)\right] - 1 \right\} \\ &= \Delta\rho \left\{ \frac{\Delta Z_H \sin\left[\frac{\pi(-u+Z_W)}{\Delta Z_H} + \alpha u\right]}{-2\pi + 2\alpha \Delta Z_H} + \frac{\Delta Z_H \sin\left[\frac{\pi(u-Z_W)}{\Delta Z_H} + \alpha u\right]}{2\pi + 2\alpha \Delta Z_H} - \frac{\sin(\alpha u)}{\alpha} \right\} \Bigg|_{Z_{\text{CH}_2}}^{Z_W} \\ &= -\frac{\Delta\rho}{\alpha} [\sin(\alpha Z_W) - \sin(\alpha Z_{\text{CH}_2})] \\ &\quad + \frac{\Delta\rho}{2} \left( \frac{1}{\alpha + \frac{\pi}{\Delta Z_H}} + \frac{1}{\alpha - \frac{\pi}{\Delta Z_H}} \right) [\sin(\alpha Z_W) + \sin(\alpha Z_{\text{CH}_2})]. \end{aligned} \quad (\text{B.20})$$

Because our X-ray scattering intensity was measured in a relative scale, an overall scaling factor was necessary for a non linear least square fitting procedure. This means that  $\Delta\rho$  can be absorbed in the scaling factor. Doing so means that the values of  $\rho_{\text{Hi}}$  and  $\rho_{\text{M}}$  resulting from a fitting procedure are relative to  $\Delta\rho$ . One way to have these parameters in the absolute scale is to integrate the bilayer electron density over



the lipid volume and equate the result to the total number of electrons in the lipid, which can easily be calculated from the chemical formula. For the ripple phase study in this thesis, the absolute values of the electron density were not of importance, so the discussion was omitted in the main text.

## B.4 Correction due to refractive index

$q_z$  needs to be corrected for index of refraction [39].

Let  $\theta'$  and  $\lambda'$  be the true scattering angle and wavelength within the sample. The wavelength by an energy analyzer,  $\lambda$ , and the scattering angle calculated from a position on a CCD detector,  $\theta$  are apparent. The correction is not necessary in the horizontal direction. The Snell's law in Fig. X gives

$$n \cos \theta = n' \cos \theta' \quad (\text{B.21})$$

$$n\lambda = n'\lambda'. \quad (\text{B.22})$$

For low angle X-ray scattering, the momentum transfer along  $z$  direction is

$$q_z = \frac{4\pi \sin \theta'}{\lambda'} \quad (\text{B.23})$$

$$= \frac{4\pi n'}{n\lambda} \sin \theta' \quad (\text{B.24})$$

$$= \frac{4\pi n'}{n\lambda} \sqrt{1 - \cos^2 \theta'} \quad (\text{B.25})$$

$$= \frac{4\pi n'}{n\lambda} \sqrt{1 - \left(\frac{n}{n'} \cos \theta\right)^2}. \quad (\text{B.26})$$

The apparent scattering angle,  $\theta$ , is directly related to the vertical pixel position,  $p_z$ , by

$$\theta = \frac{1}{2} \tan^{-1} \left( \frac{p_z}{S} \right), \quad (\text{B.27})$$

where  $S$  is the sample-to-detector distance. The typical units of  $S$  and  $p_z$  are in mm. In our experimental setup,  $n = 1$  and  $n' = 0.9999978$  for lipids at  $\lambda = 1.18 \text{ \AA}$ .  $S = 359.7 \text{ mm}$ .

# Bibliography

- [1] Martin J. Janiak, Donald M. Small, and G. Graham Shipley. Nature of the thermal pretransition of synthetic phospholipids: dimyristoyl- and dipalmitoyl-lecithin. *Biochemistry*, 15(21):4575–4580, 1976.
- [2] Rainer Fischer, Mariola Fotin-Mleczek, Hansjrg Hufnagel, and Roland Brock. Break on through to the other sidebiophysics and cell biology shed light on cell-penetrating peptides. *ChemBioChem*, 6(12):2126–2142, 2005.
- [3] Alain Joliot and Alain Prochiantz. Transduction peptides: from technology to physiology. *Nat Cell Biol*, 6(3), 2004.
- [4] Maria Lindgren, Mattias Hillbrink, Alain Prochiantz, and lo Langel. Cell-penetrating peptides. *Trends in Pharmacological Sciences*, 21(3):99 – 103, 2000.
- [5] Alan D. Frankel and Carl O. Pabo. Cellular uptake of the tat protein from human immunodeficiency virus. *Cell*, 55(6):1189 – 1193, 1988.
- [6] Maurice Green and Paul M. Loewenstein. Autonomous functional domains of chemically synthesized human immunodeficiency virus tat trans-activator protein. *Cell*, 55(6):1179 – 1188, 1988.
- [7] Eric Vivs, Priscille Brodin, and Bernard Lebleu. Hiv-1 tat protein basic domain rapidly translocates through the plasma membrane and accumulates in the cell nucleus. *Journal of Biological Chemistry*, 272(25):16010–16017, 1997.
- [8] Gohar Ter-Avetisyan, Gisela Tnnemann, Danny Nowak, Matthias Nitschke, Andreas Herrmann, Marek Drab, and M. Cristina Cardoso. Cell entry of arginine-rich peptides is independent of endocytosis. *Journal of Biological Chemistry*, 284(6):3370–3378, 2009.

- [9] Gisela Tnnemann, Robert M. Martin, Simone Haupt, Christoph Patsch, Frank Edenhofer, and M. Cristina Cardoso. Cargo-dependent mode of uptake and bioavailability of tat-containing proteins and peptides in living cells. *The FASEB Journal*, 20(11):1775–1784, 2006.
- [10] Andr Ziegler, Pierluigi Nervi, Markus Drrenberger, and Joachim Seelig. The cationic cell-penetrating peptide cpptat derived from the hiv-1 protein tat is rapidly transported into living fibroblasts: optical, biophysical, and metabolic evidence. *Biochemistry*, 44(1):138–148, 2005. PMID: 15628854.
- [11] J. S. Wadia, R. V. Stan, and S. F. Dowdy. Transducible tat-ha fusogenic peptide enhances escape of tat-fusion proteins after lipid raft macropinocytosis. *Nature Medicine*, 10(3):310–315, 2004.
- [12] I. M. Kaplan, J. S. Wadia, and S. F. Dowdy. Cationic tat peptide transduction domain enters cells by macropinocytosis. *Journal of Controlled Release*, 102(1):247–253, 2005.
- [13] David A Mann and Alan D Frankel. Endocytosis and targeting of exogenous hiv-1 tat protein. *The EMBO journal*, 10(7):1733, 1991.
- [14] Jean Philippe Richard, Kamran Melikov, Hilary Brooks, Paul Prevot, Bernard Lebleu, and Leonid V Chernomordik. Cellular uptake of unconjugated tat peptide involves clathrin-dependent endocytosis and heparan sulfate receptors. *Journal of Biological Chemistry*, 280(15):15300–15306, 2005.
- [15] Simon W Jones, Richard Christison, Ken Bundell, Catherine J Voyce, Sarah Brockbank, Peter Newham, and Mark A Lindsay. Characterisation of cell-penetrating peptide-mediated peptide delivery. *British journal of pharmacology*, 145(8):1093–1102, 2005.
- [16] Agnès Vendeville, Fabienne Rayne, Anne Bonhoure, Nadir Bettache, Philippe Montcourrier, and Bruno Beaumelle. Hiv-1 tat enters t cells using coated pits before translocating from acidified endosomes and eliciting biological responses. *Molecular biology of the cell*, 15(5):2347–2360, 2004.
- [17] Christina Foerg, Urs Ziegler, Jimena Fernandez-Carneado, Ernest Giralt, Robert Rennert, Annette G Beck-Sickinger, and Hans P Merkle. Decoding the entry of

- two novel cell-penetrating peptides in hela cells: lipid raft-mediated endocytosis and endosomal escape. *Biochemistry*, 44(1):72–81, 2005.
- [18] Antonio Fittipaldi and Mauro Giacca. Transcellular protein transduction using the tat protein of hiv-1. *Advanced drug delivery reviews*, 57(4):597–608, 2005.
- [19] Ying Liu, Melina Jones, Cynthia M Hingtgen, Guojun Bu, Nick Laribee, Rudolph E Tanzi, Robert D Moir, Avindra Nath, and Johnny J He. Uptake of hiv-1 tat protein mediated by low-density lipoprotein receptor-related protein disrupts the neuronal metabolic balance of the receptor ligands. *Nature medicine*, 6(12):1380–1387, 2000.
- [20] Vladimir P Torchilin, Ram Rammohan, Volkmar Weissig, and Tatyana S Levchenko. Tat peptide on the surface of liposomes affords their efficient intracellular delivery even at low temperature and in the presence of metabolic inhibitors. *Proceedings of the National Academy of Sciences*, 98(15):8786–8791, 2001.
- [21] Vladimir P Torchilin, Tatyana S Levchenko, Ram Rammohan, Natalia Volodina, Brigitte Papahadjopoulos-Sternberg, and Gerard GM D’Souza. Cell transfection in vitro and in vivo with nontoxic tat peptide-liposome-dna complexes. *Proceedings of the National Academy of Sciences*, 100(4):1972–1977, 2003.
- [22] Carsten Rudolph, Christian Plank, James Lausier, Ulrike Schillinger, Rainer H Müller, and Joseph Rosenecker. Oligomers of the arginine-rich motif of the hiv-1 tat protein are capable of transferring plasmid dna into cells. *Journal of Biological Chemistry*, 278(13):11411–11418, 2003.
- [23] Ashok Chauhan, Akshay Tikoo, Arvinder K Kapur, and Mahavir Singh. The taming of the cell penetrating domain of the hiv tat: myths and realities. *Journal of Controlled Release*, 117(2):148–162, 2007.
- [24] JM Sabatier, E Vives, K Mabrouk, ABDELAZIZ Benjouad, H Rochat, A Duval, B Hue, and ELMOSTAFA Bahraoui. Evidence for neurotoxic activity of tat from human immunodeficiency virus type 1. *Journal of virology*, 65(2):961–967, 1991.
- [25] A. Mishra, V. D. Gordon, L. H. Yang, R. Coridan, and G. C. L. Wong. Hiv tat forms pores in membranes by inducing saddle-splay curvature: Potential

- role of bidentate hydrogen bonding. *Angewandte Chemie-International Edition*, 47(16):2986–2989, 2008.
- [26] S. T. Yang, E. Zaitseva, L. V. Chernomordik, and K. Melikov. Cell-penetrating peptide induces leaky fusion of liposomes containing late endosome-specific anionic lipid. *Biophysical Journal*, 99(8):2525–2533, 2010.
- [27] P. E. G. Thoren, D. Persson, E. K. Esbjorner, M. Goksor, P. Lincoln, and B. Norden. Membrane binding and translocation of cell-penetrating peptides. *Biochemistry*, 43(12):3471–3489, 2004.
- [28] SD Krämer and H Wunderli-Allenspach. No entry for tat (44–57) into liposomes and intact mdck cells: novel approach to study membrane permeation of cell-penetrating peptides. *Biochimica et Biophysica Acta (BBA)-Biomembranes*, 1609(2):161–169, 2003.
- [29] C. Ciobanasu, J. P. Siebrasse, and U. Kubitscheck. Cell-penetrating hiv1 tat peptides can generate pores in model membranes. *Biophysical Journal*, 99(1):153–62, 2010.
- [30] Philip A Gurnev, Sung-Tae Yang, Kamran C Melikov, Leonid V Chernomordik, and Sergey M Bezrukov. Cationic cell-penetrating peptide binds to planar lipid bilayers containing negatively charged lipids but does not induce conductive pores. *Biophysical journal*, 104(9):1933–1939, 2013.
- [31] H. D. Herce, A. E. Garcia, J. Litt, R. S. Kane, P. Martin, N. Enrique, A. Rebolledo, and V. Milesi. Arginine-rich peptides destabilize the plasma membrane, consistent with a pore formation translocation mechanism of cell-penetrating peptides. *Biophysical Journal*, 97(7):1917–1925, 2009.
- [32] Y. C. Su, A. J. Waring, P. Ruchala, and M. Hong. Membrane-bound dynamic structure of an arginine-rich cell-penetrating peptide, the protein transduction domain of hiv tat, from solid-state nmr. *Biochemistry*, 49(29):6009–6020, 2010.
- [33] S. Shojania and J. D. O’Neil. Hiv-1 tat is a natively unfolded protein - the solution conformation and dynamics of reduced hiv-1 tat-(1-72) by nmr spectroscopy. *Journal of Biological Chemistry*, 281(13):8347–8356, 2006.

- [34] P. Bayer, M. Kraft, A. Ejchart, M. Westendorp, R. Frank, and P. Rosch. Structural studies of hiv-1 tat protein. *Journal of Molecular Biology*, 247(4):529–535, 1995.
- [35] H. D. Herce and A. E. Garcia. Molecular dynamics simulations suggest a mechanism for translocation of the hiv-1 tat peptide across lipid membranes. *Proceedings of the National Academy of Sciences of the United States of America*, 104(52):20805–20810, 2007.
- [36] S. Yesylevsky, S. J. Marrink, and A. E. Mark. Alternative mechanisms for the interaction of the cell-penetrating peptides penetratin and the tat peptide with lipid bilayers. *Biophysical Journal*, 97(1):40–49, 2009.
- [37] Y. Lyatskaya, Y. F. Liu, S. Tristram-Nagle, J. Katsaras, and J. F. Nagle. Method for obtaining structure and interactions from oriented lipid bilayers. *Physical Review E*, 63(1):0119071–0119079, 2001.
- [38] Y. F. Liu and J. F. Nagle. Diffuse scattering provides material parameters and electron density profiles of biomembranes. *Physical Review E*, 69(4):040901–040904(R), 2004.
- [39] Yufeng Liu. *NEW METHOD TO OBTAIN STRUCTURE OF BIOMEMBRANES USING DIFFUSE -RAY SCATTERING: APPLICATION TO FLUID PHASE DOPC LIPID BILAYERS*. PhD thesis, Carnegie Mellon University, 2003.
- [40] John F Nagle and Stephanie Tristram-Nagle. Structure of lipid bilayers. *Biochimica et Biophysica Acta (BBA)-Reviews on Biomembranes*, 1469(3):159–195, 2000.
- [41] Norbert Kuerka, John F. Nagle, Jonathan N. Sachs, Scott E. Feller, Jeremy Pencer, Andrew Jackson, and John Katsaras. Lipid bilayer structure determined by the simultaneous analysis of neutron and x-ray scattering data. *Biophysical Journal*, 95(5):2356 – 2367, 2008.
- [42] Stephanie Tristram-Nagle, Yufeng Liu, Justin Legleiter, and John F. Nagle. Structure of gel phase DMPC determined by x-ray diffraction. *Biophysical Journal*, 83(6):3324 – 3335, 2002.

- [43] Anthony R. Braun, Jonathan N. Sachs, and John F. Nagle. Comparing simulations of lipid bilayers to scattering data: The gromos 43a1-s3 force field. *The Journal of Physical Chemistry B*, 117(17):5065–5072, 2013.
- [44] <http://seal.web.cern.ch/seal/documents/minuit/mnusersguide.pdf>.
- [45] <http://lcgapp.cern.ch/project/cls/work-packages/mathlibs/minuit/index.html>.
- [46] Berk Hess, Carsten Kutzner, David van der Spoel, and Erik Lindahl. Gromacs 4: Algorithms for highly efficient, load-balanced, and scalable molecular simulation. *Journal of Chemical Theory and Computation*, 4(3):435–447, 2008.
- [47] Joakim P. M. Jmbeck and Alexander P. Lyubartsev. Derivation and systematic validation of a refined all-atom force field for phosphatidylcholine lipids. *The Journal of Physical Chemistry B*, 116(10):3164–3179, 2012.
- [48] Joakim P. M. Jmbeck and Alexander P. Lyubartsev. An extension and further validation of an all-atomistic force field for biological membranes. *Journal of Chemical Theory and Computation*, 8(8):2938–2948, 2012.
- [49] Viktor Hornak, Robert Abel, Asim Okur, Bentley Strockbine, Adrian Roitberg, and Carlos Simmerling. Comparison of multiple amber force fields and development of improved protein backbone parameters. *Proteins: Structure, Function, and Bioinformatics*, 65(3):712–725, 2006.
- [50] W. L. Jorgensen, J. Chandrasekhar, J. D. Madura, R. W. Impey, and M. L. Klein. Comparison of simple potential functions for simulating liquid water. *Journal of Chemical Physics*, 79(2):926–935, 1983.
- [51] Norbert Kuerka, John Katsaras, and JohnF. Nagle. Comparing membrane simulations to scattering experiments: Introducing the simtoexp software. *Journal of Membrane Biology*, 235(1):43–50, 2010.
- [52] Shuichi Miyamoto and Peter A Kollman. Settle: an analytical version of the shake and rattle algorithm for rigid water models. *Journal of computational chemistry*, 13(8):952–962, 1992.

- [53] B. Hess, H. Bekker, H. J. C. Berendsen, and J. G. E. M. Fraaije. Lincs: A linear constraint solver for molecular simulations. *J Comput Chem*, 18(12):1463–1472, 1997.
- [54] Tom Darden, Darrin York, and Lee Pedersen. Particle mesh ewald: An  $n \log(n)$  method for ewald sums in large systems. *The Journal of chemical physics*, 98(12):10089–10092, 1993.
- [55] Giovanni Bussi, Davide Donadio, and Michele Parrinello. Canonical sampling through velocity rescaling. *The Journal of chemical physics*, 126(1):014101, 2007.
- [56] Michele Parrinello and Aneesur Rahman. Polymorphic transitions in single crystals: A new molecular dynamics method. *Journal of Applied physics*, 52(12):7182–7190, 1981.
- [57] Norbert Kučerka, Yufeng Liu, Nanjun Chu, Horia I Petrache, Stephanie Tristram-Nagle, and John F Nagle. Structure of fully hydrated fluid phase DMPC and DLPC lipid bilayers using X-ray scattering from oriented multilamellar arrays and from unilamellar vesicles. *Biophysical journal*, 88(4):2626–2637, 2005.
- [58] Norbert Kučerka, Stephanie Tristram-Nagle, and John F Nagle. Closer look at structure of fully hydrated fluid phase dppc bilayers. *Biophysical journal*, 90(11):L83–L85, 2006.
- [59] Norbert Kučerka, Stephanie Tristram-Nagle, and John F Nagle. Structure of fully hydrated fluid phase lipid bilayers with monounsaturated chains. *The Journal of membrane biology*, 208(3):193–202, 2005.
- [60] Stephanie Tristram-Nagle, Chao-Ping Yang, and John F Nagle. Thermodynamic studies of purple membrane. *Biochimica et Biophysica Acta (BBA)-Biomembranes*, 854(1):58–66, 1986.
- [61] <http://www.basic.northwestern.edu/biotools/proteincalc.html>.
- [62] A. C. V. Johansson and E. Lindahl. The role of lipid composition for insertion and stabilization of amino acids in membranes. *Journal of Chemical Physics*, 130(18), 2009.



- [63] S. Tristram-Nagle and J. F. Nagle. Hiv-1 fusion peptide decreases bending energy and promotes curved fusion intermediates. *Biophysical Journal*, 93(6):2048–2055, 2007.
- [64] L. B. Li, I. Vorobyov, and T. W. Allen. Potential of mean force and pk(a) profile calculation for a lipid membrane-exposed arginine side chain. *Journal of Physical Chemistry B*, 112(32):9574–9587, 2008.
- [65] I. Vorobyov, L. B. Li, and T. W. Allen. Assessing atomistic and coarse-grained force fields for protein-lipid interactions: The formidable challenge of an ionizable side chain in a membrane. *Journal of Physical Chemistry B*, 112(32):9588–9602, 2008.
- [66] J. L. MacCallum, W. F. D. Bennett, and D. P. Tieleman. Distribution of amino acids in a lipid bilayer from computer simulations. *Biophysical Journal*, 94(9):3393–3404, 2008.
- [67] E. V. Schow, J. A. Freites, P. Cheng, A. Bernsel, G. von Heijne, S. H. White, and D. J. Tobias. Arginine in membranes: The connection between molecular dynamics simulations and translocon-mediated insertion experiments. *Journal of Membrane Biology*, 239(1-2):35–48, 2011.
- [68] W. C. Wimley, T. P. Creamer, and S. H. White. Solvation energies of amino acid side chains and backbone in a family of host-guest pentapeptides. *Biochemistry*, 35(16):5109–5124, 1996.
- [69] W. C. Wimley and S. H. White. Experimentally determined hydrophobicity scale for proteins at membrane interfaces. *Nature Structural Biology*, 3(10):842–848, 1996.
- [70] B. Roux. Lonely arginine seeks friendly environment. *Journal of General Physiology*, 130(2):233–236, 2007.
- [71] W. Kabsch and C. Sander. Dictionary of protein secondary structure: pattern recognition of hydrogen-bonded and geometrical features. *Biopolymers*, 22(12):2577–637, 1983.
- [72] D. Choi, J. H. Moon, H. Kim, B. J. Sung, M. W. Kim, G. Y. Tae, S. K. Satija, B. Akgun, C. J. Yu, H. W. Lee, D. R. Lee, J. M. Henderson, J. W. Kwong,

- K. L. Lam, K. Y. C. Lee, and K. Shin. Insertion mechanism of cell-penetrating peptides into supported phospholipid membranes revealed by x-ray and neutron reflection. *Soft Matter*, 8(32):8294–8297, 2012.
- [73] K. Huang and A. E. Garcia. Free energy of translocating an arginine-rich cell-penetrating peptide across a lipid bilayer suggests pore formation. *Biophysical Journal*, 104(2):412–420, 2013.
- [74] Martin J Janiak, Donald M Small, and G Graham Shipley. Temperature and compositional dependence of the structure of hydrated dimyristoyl lecithin. *Journal of Biological Chemistry*, 254(13):6068–6078, 1979.
- [75] A. Tardieu, Vittorio Luzzati, and F.C. Reman. Structure and polymorphism of the hydrocarbon chains of lipids: A study of lecithin-water phases. *Journal of Molecular Biology*, 75(4):711 – 733, 1973.
- [76] Daniel C. Wack and Watt W. Webb. Synchrotron x-ray study of the modulated lamellar phase  $p\beta'$  in the lecithin-water system. *Phys. Rev. A*, 40:2712–2730, Sep 1989.
- [77] Haruhiko Yao, Sinzi Matuoka, Boris Tenchov, and Ichiro Hatta. Metastable ripple phase of fully hydrated dipalmitoylphosphatidylcholine as studied by small angle x-ray scattering. *Biophysical journal*, 59(1):252–255, 1991.
- [78] W J Sun, S Tristram-Nagle, R M Suter, and J F Nagle. Structure of the ripple phase in lecithin bilayers. *Proceedings of the National Academy of Sciences*, 93(14):7008–7012, 1996.
- [79] Beth A Cunningham, Ari-David Brown, David H Wolfe, W Patrick Williams, and Anthony Brain. Ripple phase formation in phosphatidylcholine: Effect of acyl chain relative length, position, and unsaturation. *Physical Review E*, 58(3):3662, 1998.
- [80] Kell Mortensen, Walter Pfeiffer, Erich Sackmann, and Wolfgang Knoll. Structural properties of a phosphatidylcholine-cholesterol system as studied by small-angle neutron scattering: ripple structure and phase diagram. *Biochimica et Biophysica Acta (BBA)-Biomembranes*, 945(2):221–245, 1988.

- [81] Jeremy P Bradshaw, Michael S Edenborough, Philip JH Sizer, and Anthony Watts. Observation of rippled dioleoylphosphatidylcholine bilayers by neutron diffraction. *Biochimica et Biophysica Acta (BBA)-Biomembranes*, 987(1):111–114, 1989.
- [82] JT Woodward IV and JA Zasadzinski. Amplitude, wave form, and temperature dependence of bilayer ripples in the  $p\beta$  phase. *Physical Review E*, 53(4):R3044, 1996.
- [83] JA Zasadzinski, J Schneir, J Gurley, V Elings, and PK Hansma. Scanning tunneling microscopy of freeze-fracture replicas of biomembranes. *Science*, 239(4843):1013–1015, 1988.
- [84] M. P. Hentschel and F. Rustichelli. Structure of the ripple phase  $P'_\beta$  in hydrated phosphatidylcholine multimembranes. *Phys. Rev. Lett.*, 66:903–906, Feb 1991.
- [85] Alex H. de Vries, Serge Yefimov, Alan E. Mark, and Siewert J. Marrink. Molecular structure of the lecithin ripple phase. *Proceedings of the National Academy of Sciences of the United States of America*, 102(15):5392–5396, 2005.
- [86] S. A. Tristram-Nagle. Preparation of oriented, fully hydrated lipid samples for structure determination using x-ray scattering. *Methods Mol Biol*, 400:63–75, 2007.
- [87] [http://henke.lbl.gov/optical\\_constants](http://henke.lbl.gov/optical_constants).
- [88] M.C. Wiener, R.M. Suter, and J.F. Nagle. Structure of the fully hydrated gel phase of dipalmitoylphosphatidylcholine. *Biophysical Journal*, 55(2):315 – 325, 1989.
- [89] Alejandro B. Rodriguez-Navarro. Registering pole figures using an X-ray single-crystal diffractometer equipped with an area detector. *Journal of Applied Crystallography*, 40(3):631–634, Jun 2007.
- [90] Jessy L. Baker, Leslie H. Jimison, Stefan Mannsfeld, Steven Volkman, Shong Yin, Vivek Subramanian, Alberto Salleo, A. Paul Alivisatos, and Michael F. Toney. Quantification of thin film crystallographic orientation using x-ray diffraction with an area detector. *Langmuir*, 26(11):9146–9151, 2010. PMID: 20361783.